Microwave Field Applicator Design in Small-Scale Chemical Processing

Guido Sander Jan STURM

Microwave Field Applicator Design in Small-Scale Chemical Processing

Proefschrift

ter verkrijging van de graad van doctor

aan de Technische Universiteit Delft,

op gezag van de Rector Magnificus prof. ir. K.C.A.M. Luyben,

voorzitter van het College voor Promoties,

in het openbaar te verdedigen op maandag 11 november 2013 om 10.00 uur

door

Guido Sander Jan STURM

werktuigkundig ingenieur
geboren te Roosendaal en Nispen

Dit proefschrift is goedgekeurd door de promotor:
Prof. dr. ir. A.I. Stankiewicz

Copromotoren:
Dr. ir. M.D. Verweij
Dr. ir. G.D. Stefanidis

Samenstelling promotiecommissie:

Rector Magnificus,	voorzitter
Prof. dr. ir. A.I. Stankiewicz	Technische Universiteit Delft, promotor
Dr. ir. M.D. Verweij	Technische Universiteit Delft, copromotor
Dr. ir. G.D. Stefanidis	Technische Universiteit Delft, copromotor
Prof. dr. V. Hessel	Technische Universiteit Eindhoven
Prof. DSc. A. Yarovoy	Technische Universiteit Delft
Prof. dr. B. Ondruschka	Friedrich-Schiller-Universität Jena
Dr. M. Radoiu	Sairem SAS
Prof. dr. ir. B.J. Boersma	Technische Universiteit Delft, reservelid

Dit werk is financieel ondersteund door STW (Divisie toegepaste wetenschap NWO, Ministerie van Economische Zaken, Nederland)

ISBN: 978-94-6191-945-8

Cover layout, Legatron Electronic Publishing
Printed by Ipskamp Drukkers

voor Joke, Frans en Bram

Summary

Ever since the first experiments nearly three decades ago, microwave enhanced chemistry has received incessant scientific attention. Many studies report improved process performance in terms of speed and conversion under microwave exposure and therefore it is recognized as a promising alternative method of process activation. It has also raised skepticism though, since the mechanisms behind the process enhancement remain unclear. Nevertheless, in the context of process intensification, the combination of microwave fields and microreactor systems has a promising quality; the enhanced reaction rates of the former and the superior heat and mass transfer rates and tightly controlled processing conditions of the latter together may provide a well-controlled and highly intensified processing environment.

The objective of this thesis is to explore the possibilities to apply a microwave field in microstructured reactor systems. The familiar (domestic) multimode cavity systems are discounted as a viable means to apply a microwave field to a microreactor; the electromagnetic conditions in such systems simply are too poorly defined and controlled.

In order to give each molecule the same processing experience, the field applicator needs to apply a spatially uniform microwave field. Therefore it is investigated what the theoretical limitations are on the uniformity of the electromagnetic field and heating rate distribution under parametric variation in a hypothetical resonant system. Design charts are presented that illustrate how important operating, geometric and medium parameters relate with each other. It is demonstrated how these simple configurations can provide design guidelines and first approximations for more realistic process equipment geometries.

In a next step, the practical limitations encountered in commonly applied cavity systems are investigated. To this end, a simple exemplary process was analyzed both by experiment and simulation. The process under consideration is heating of water contained in a vial inside a popular, off-the-shelf, single-mode microwave cavity device. Both the heating rate distribution and the overall heating rate are investigated as well as the sensitivity of these measures to parametric variation. It is found that the resonant microwave field in generic, non-tailored systems is highly sensitive to parametric variation, that the heating process is hard to predict, and that that such systems do not lend themselves for control or optimization.

Currently, the types of microwave equipment that are used in microwave chemistry research are principally limited to the aforementioned generic microwave systems.

To widen this scope, the potential of standard sized, rectangular waveguides to form a basis for microwave applicator systems is explored. It is demonstrated that such systems support microwave fields that are relatively simple and predictable, which enables a higher degree of adaption and optimization to fit specific process requirements. The feasibility of long residence time continuous flow processing under microwave activation is experimentally demonstrated in a novel reactor type that the rectangular waveguide uniquely supports.

Up to this point only cavity systems that support resonant fields have been considered. Resonant conditions are associated with hard-to-predict electromagnetic field patterns, difficulty in controlling and optimizing heat generation, and intrinsic spatial non-uniformity. The novel Coaxial Traveling Microwave Reactor concept is proposed as a means to address these issues by avoiding resonance altogether. Thus the highly optimized processing conditions characteristic of microreactors may be retained. Two concept variants are presented, one for liquid phase processing and one for heterogeneous gas phase catalytic reactions, respectively. A method to optimize the applicator geometry is demonstrated.

The thesis is concluded by a discussion on the design principles that were identified in the course of the research and a on a framework for further development of equipment for electromagnetically enhanced chemical processing systems.

Samenvatting

Al vanaf de eerste experimenten, bijna drie decennia geleden, is er aanhoudende wetenschappelijke belangstelling geweest voor door microgolfvelden gedreven chemie. Veel studies rapporteren verbeterde procesresultaten, zowel in snelheid als conversie, bij blootstelling aan microgolfvelden. Microgolfvelden worden daarom gezien als een veelbelovende alternatieve vorm van activatie voor chemische processen. Er is echter ook scepsis ontstaan, want de mechanismen achter de procesversnelling blijven vooralsnog onduidelijk. Desondanks is combinatie van microgolfvelden met microreactoren in een procesintensificatiecontext veelbelovend; de verhoogde reactiesnelheid van de ene technologie gecombineerd met de superieure warmte- en stofoverdracht en nauwkeurig beheersbare procescondities van de andere zouden samen een goed gecontroleerde en sterk geïntensiveerde reactieomgeving kunnen vormen.

Het doel van dit proefschrift is om te verkennen wat de mogelijkheden zijn van toepassing van microgolfvelden in microreactoren. De algemeen bekende (huishoudelijke) meervoudig modale microgolfsystemen worden ongeschikt verklaard als middel om een microreactor van een microgolfveld te voorzien; de elektromagnetische omstandigheden in dergelijke systemen zijn simpelweg te slecht te bepalen en te beheersen.

Om ieder molecuul hetzelfde procesverloop te geven moet de microgolfveldapplicator een ruimtelijk uniform veld aanbrengen. Daarom is voor een hypothetisch resonerend systeem onderzocht wat de theoretische beperkingen zijn aan de elektromagnetische velduniformiteit en aan de verdeling van de warmtegeneratie onder variatie van parameters. Er worden ontwerpdiagrammen gepresenteerd die illustreren hoe belangrijke geometrische, medium- en bedrijfsparameters met elkaar samenhangen. Getoond wordt hoe deze eenvoudige configuraties kunnen voorzien in ontwerprichtlijnen en in eerste benaderingen voor realistischere geometrieën van procesapparatuur.

In een hierop volgende stap zijn de praktische beperkingen onderzocht die spelen bij veelgebruikte systemen met resonantieholte. Hiertoe is door middel van experiment en simulatie een eenvoudig voorbeeldproces geanalyseerd. Dit proces betreft het verhitten van water in een glazen buis met een populair, commercieel verkrijgbaar systeem met een enkelvoudig modale microgolfresonantieholte. Zowel de totale hoeveelheid als de verdeling van de warmtegeneratie zijn onderzocht, alsmede de gevoeligheid voor parametervariatie van deze kenmerken. Het blijkt dat het resonante microgolfveld in generieke, niet op maat

gemaakte systemen zeer gevoelig is voor parametervariatie, dat het verhittingsproces moeilijk te voorspellen is, en dat dergelijke systemen zich niet lenen voor procesbeheersing en -optimalisatie.

Momenteel zijn de typen microgolfapparaten die gebruikt worden in onderzoek naar microgolfchemie voornamelijk beperkt tot de voorgenoemde generieke systemen. Om dit overzicht te verruimen is het potentieel verkend van standaardmaat rechthoekige golfgeleiders om als basis te dienen voor applicatorsystemen van microgolfvelden. Aangetoond wordt dat zulke systemen velden ondersteunen die relatief eenvoudig en voorspelbaar zijn, wat de aanpasbaarheid en optimaliseerbaarheid van de microgolfvelden bevorderd. De haalbaarheid van continue processen met een lange verblijftijd is experimenteel gedemonstreerd in een nieuw reactortype dat enkel ondersteund wordt door rechthoekige golfgeleiders.

Tot aan dit punt zijn enkel systemen met resonante velden in ogenschouw genomen. Deze velden gaan samen met moeilijk te voorspellen elektromagnetische ruimtelijke patronen, met moeilijkheden bij het beheersen en optimaliseren van de warmtegeneratie, en met een intrinsiek niet-gelijkmatige ruimtelijke veldverdeling. Om dit te ondervangen wordt een nieuw concept voorgesteld, de coaxiale lopende-microgolfreactor, waarmee de kwesties die zich in resonante velden voordoen geheel worden vermeden. Op deze manier blijven de sterk geoptimaliseerde procescondities van microreactoren behouden. Twee conceptvarianten worden gepresenteerd, één voor vloeistoffase processen en één voor heterogene gasfase katalytische reacties. Een methode voor geometrische optimalisatie van deze systemen wordt gedemonstreerd.

Het proefschrift wordt afgesloten met een discussie over de ontwerpprincipes die zijn geïdentificeerd gedurende het onderzoek, en met het geven van een raamwerk voor verdere ontwikkeling van apparatuur voor elektromagnetisch gedreven chemische processystemen.

Table of Contents

Chapter 1

Introduction

1.1 Microwaves and microreactors – A promising concept

In a world with emerging economies, growing populations and ever scarcer and harder to explore natural resources, mankind will need to utilize these resources more efficiently in order to maintain the historic rise in living standards. The process industry takes center stage in this context, as it generates economic value by transforming these resources into raw materials, intermediate and final products, energy, and – inevitably – byproducts and energy losses. In fact, the process industry is notorious for its inefficient use of resources. In particular, waste stream sizes are reported [1,2] that are by mass 1 to 5 times the size of the desired product yield for bulk chemical production and 5 to 50 times in case of fine chemical production. As pointed out by Stankiewicz and Moulijn [3], conceptually, chemical process equipment has not changed much over the centuries; they present an example from a 16th century's scientific work, *De Re Metallica* by Georgius Agricola [4,5], in which the devices shown resemble present day stirred tank systems quite accurately, systems which – at least conceptually – seem to be inspired by the cooking pots that have been around since the dawn of time. Another somewhat less ancient example is distillation – separation technology's workhorse; the physical process was described already in antiquity in the context of water desalination [6], and the first monograph on the subject, *Liber de arte Distillandi de Compositis* by Hieronymus Brunschwig [7], appeared early in the scientific revolution.

Despite continual improvements to these traditional processes, as mentioned above, losses in terms of materials and energy are undesirably high. Stankiewicz and Moulijn [3] argue that the limited performance is inherent to these traditional processes and they urge for intensification of chemical processes, i.e. the development of new technologies that reach beyond these limitations. In that publication process intensification is described as reaching "breakthrough changes" by applying "novel [engineering] methods and equipment" to bring about "dramatic improvement" in process performance. The performance indicators mentioned are: relative equipment size (or hold-up), energy consumption and waste production; a target for performance improvement of a factor of two is proposed for a technology to qualify as process intensification. A number of examples are mentioned among which include: static mixers, packings or monolithic reactors with functionalized catalytic surfaces, microreactors, high gravity rotating devices, membrane reactors, hybrid separations, and alternative forms of energy such as microwave fields or ultrasound. What these intensified designs characteristically have in common is that 1) they are different from the traditional processes on a *conceptual level* and that 2) their performance is *inherently better* than the traditional processes.

The framework of process intensification is further formalized by Van Gerven and Stankiewicz [8], who propose four underlying generic principles to obtain the dramatic performance improvements and four technological approaches to follow these principles in spatial domains ranging from molecular events to plant scale operations. The principles herein are: 1) to "maximize the effectiveness of intra- and intermolecular events", 2) to "give each molecule the same processing experience", 3) to "optimize the driving forces at every scale and maximize the specific surface area to which these forces apply", and 4) to "maximize the synergistic effects from partial processes". The technological approaches distinguished in this framework are: 1) structural solutions, such as static mixers or microstructured systems, 2) alternative forms of energy, e.g. high gravity fields, light of various wavelengths, or – lower in the electromagnetic spectrum – microwave fields, 3) synergistic solutions, like multifunctional reactions or hybrid separations, and 4) technologies that manipulate the course of a process in time, for example by intensifying conditions to achieve millisecond processing or by applying periodicity to processes.

A promising concept in this framework is the combination of micro- or millistructured reactors with microwave fields. Small-structured reactors offer many advantages when compared to traditional systems [3,9-15]: they enable high heat and mass transfer rates and allow for a tight control on operating conditions and a high selectivity; furthermore, the smaller volumes are an inherently safer processing environment for toxic or explosive chemicals because they reduce inventory and thereby the risks; and, finally, smaller systems enable flexible, on-demand and decentralized processing.

The combination with microwave fields is particularly interesting [16]. On the chemistry side, chemical activation by microwave fields has been a widely researched topic for several decades [17-40], since there are a number of notable aspects to this unconventional form of energy. There are two undisputed inherent advantages to microwave fields. First, electromagnetic energy is transmitted at the speed of light, which is effectively instantaneous on the time scales of chemical processing. This facilitates control, since there is no thermal inertia, and allows for very high rates of energy and, thus, intensified conditions, due to the absence of (thermal) transfer surface limitations. Second, electromagnetic energy can be dissipated selectively, heating processes or activating reactions at locations only where this is desired, as opposed to thermal activation, which heats non-selectively; e.g. activation by microwave fields may permit a desired reaction on a hot electromagnetically dissipating catalytic site, while maintaining cooler bulk conditions to prevent unwanted side reactions.

Furthermore, there are some interesting but controversial additional aspects to microwave activation of chemical reactions. Ever since the first investigations on the subject [41,42] unexpectedly high reaction conversions are reported [43-48]; some studies even report acceleration factors in the order of several hundred times the conventionally activated case. Speculations have risen regarding the possibility of direct interactions of the microwave field with the reaction mechanism, i.e. not due to thermal activation caused by the generation of heat through electromagnetic dissipation, but alternative explanations have also been proposed. A number of studies point out that heat generation occurs non-uniformly in a microwave field [49-51]; it is argued that it is possible that temperature is monitored by a sensor that is placed in a relatively cold zone, so that the dominant temperature development, which drives the reaction, remains hidden from observation. Indeed, there are studies [52-54] that describe cases in which apparent microwave effects disappear under vigorous stirring. Another alternative explanation that is proposed implicates the heterogeneity of reactant mixtures and the interaction that a microwave field might have with an interface between aggregation states; studies by Dressen et al. [55,56] relate for a number of cases an apparent microwave effect to the heterogeneity of the reactant mixture. In particular, they report that the addition of a co-solvent coincides with the disappearance of microwave specific conversion rates.

Despite these efforts however, it has proven very hard to draw any definite conclusions on the interactions between microwaves and chemical reactions. The reason is that the exact processing conditions generally are unknown. As explained above, temperature may develop non-uniformly under microwave conditions, causing uncertainty with respect to this particular parameter. Although this can be alleviated by stirring in some cases, in other processes stirring is impossible, ineffective or undesired. Some examples in this respect are: packed beds [49,50], highly viscous polymerization systems [57], or (most relevant in the context of this thesis) continuous flow (milli)reactors. The set of relevant processing conditions is not limited to temperature though. Far more fundamental to the behavior of microwave enhanced processing systems are the actual electromagnetic interactions of the microwave field, since it is this field that supplies the energy to drive the process. More specifically, it is the electric field component of the microwave field that exerts forces on the electric charges in the molecules, thereby inducing movement of these molecules. For one thing, this movement is rapidly thermalized by Brownian interactions, which amounts to heat generation by electromagnetic dissipation. In addition to this though, it is the interaction of the microwave field with the molecules – whether through the exerted electric forces or through specific molecular movements – that is suspected of influencing chemical reaction rates via a yet unknown mechanism. It is therefore essential to know what the electromagnetic conditions are. As a matter of course, make and model of microwave equipment as well as the method of operation – either power or temperature control – are carefully and dutifully reported in relevant literature, but this does not translate into anything quantifiable on the field as it is acting on the process fluids. *Indeed the actual physical properties of the electromagnetic field in terms of field strength, field vector direction and polarization are never reported.* Additionally, frequencies outside the 2.45 GHz ISM [58] band are hardly ever considered for lack of available equipment.

This brings us to a final potentially important aspect of combining process activation by microwave fields with micro- and millistructured processing systems; the high degree of control over the process conditions in small scale processing systems would enable detailed investigation of the microwave-chemical interactions. In order to reach this objective, it is necessary to integrate the microwave field applicator – the structure that supports and contains the field – into the processing system. This poses an interesting challenge, as it requires to bride a fundamental knowledge gap between the fields of chemical engineering and electromagnetics engineering. Although many chemistry experiments have been conducted in microwave equipment, the theory of electromagnetics and electromagnetic wave propagation is largely absent from publications in the research field of microwave assisted chemistry. Since this thesis attempts to fill the aforementioned knowledge gap, the next three sections will introduce a number of key concepts regarding wave propagation and electromagnetic fields.

1.2 Characteristics of electromagnetic interactions

Because of their relative novelty to process engineering, this section will illustrate some relevant properties of microwave fields as they are applied in heating applications. In the first place, microwave fields are electromagnetic waves; as such, they obey Maxwell's electromagnetic field equations,

$$\begin{aligned} -\nabla\times\mathbf{H} + \partial_t\varepsilon\mathbf{E} + \sigma\mathbf{E} &= \mathbf{0} \\ \nabla\times\mathbf{E} + \partial_t\mu\mathbf{H} &= \mathbf{0} \end{aligned} \tag{1.1}$$

These equations describe the relation between the time-dependent electric field $\mathbf{E}$ and the time-dependent magnetic field $\mathbf{H}$. The term $\sigma\mathbf{E}$ denotes the electric current density – conductivity multiplied by the electric field –, which plays a role in conductive media such as metal walls, but is absent in vacuum or electrically insulating media. The properties of the medium that the electromagnetic wave propagates through are the electric permittivity ε and the magnetic permeability μ; in the context of this thesis, the former medium parameter is the most relevant one, because it depends on the media under consideration. In contrast, the parameter μ is fixed to the permeability of vacuum μ_0 because only nonmagnetic materials are considered in this thesis. The coupling between the electric and magnetic constituent fields results in a wave pattern interaction that transmits energy through space.

In many applications – including the context of this thesis – the electromagnetic field under consideration is time-harmonic, i.e. its constituent fields have sinusoidal time dependence. As such, the fields are conveniently expressed as a complex space-dependent parameter multiplied by $e^{i2\pi ft}$; by using the exponential function in this way with complex argument, it expresses a time harmonic function over time t with frequency f. The electric and magnetic fields thus become $\mathbf{E}(x,y,z,t) = \mathbf{E}(x,y,z)e^{i2\pi ft}$ and $\mathbf{H}(x,y,z,t) = \mathbf{H}(x,y,z)e^{i2\pi ft}$, respectively (note that $2\pi f$ is often expressed as ω, the angular frequency, and that i, the imaginary unit, is also often represented by the symbol j). Substitution in Eq. 1.1 yields,

$$\begin{aligned} -\nabla\times\mathbf{H} + i2\pi f\varepsilon\mathbf{E} &= \mathbf{0} \\ \nabla\times\mathbf{E} + i2\pi f\mu\mathbf{H} &= \mathbf{0} \end{aligned} \tag{1.2}$$

For this time-harmonic representation of Maxwell's electromagnetic field equations, the medium parameters ε and μ are complex valued parameters. In case the respective imaginary parts are non-zero, they relate to energy dissipation. In the context of this work, the latter does not hold for the magnetic permeability term, because – as was mentioned above – only nonmagnetic materials are considered. The dielectric permittivity can include a dissipation term though; the dielectric permittivity is then denoted as $\varepsilon = \varepsilon_0(\varepsilon' - i\varepsilon'')$. In literature, often the bracketed terms are reported as the dielectric medium properties. Since they express the dielectric permittivity of a medium relative to the vacuum permittivity, ε_0, the combined parameters, $\varepsilon' - i\varepsilon''$, are called *relative permittivity*.

Microwave fields are defined as electromagnetic fields with a frequency between 300 MHz and 300 GHz or, equivalently, with wavelengths in vacuum ranging from 1 m to 1 mm. Whether the wave-like nature of electromagnetic fields is relevant to specific applications depends largely on the geometrical characteristics of objects or equipment that are interacting with the field. More specifically, it depends on their size relative to the field's wavelength. It will be discussed briefly here how this affects the analysis. For a more detailed discussion on this subject, one is referred to the large volume of literature that addresses it, for example to the work by Van Bladel [59] that deals with the methodology electromagnetics analysis exhaustively.

Figure 1.1a illustrates the case in which the wavelength is (very) large with respect to a dielectric object that is exposed to the electromagnetic field. The arrows indicate the direction of the electric field and the grayscale of the object indicates the amplitude, or peak field strength, of the field in the object – darker zones have higher intensity. For a field with a frequency of zero and an infinitely long wavelength, the electric field would be static, i.e. unchanging in time. For non-zero frequencies, the field would exhibit a sinusoidal oscillation with two reversals of the field direction per oscillation period. There are some variations in the field intensity in the object. Inside and in the vicinity of the object the field is affected by the presence of the object, but at some distance there is no influence of its presence. Under the above conditions – electrically non-conductive, non-magnetic media –, the analysis of this case reduces to quasi-static analysis via potential theory, reducing the complexity of the problem considerably.

Figure 1.1b illustrates the case in which the wavelength is (very) small with respect to the object. Unlike in Figure 1.1a, the arrows in Figure 1.1b indicate the direction in which the field propagates, not the direction of the electric field vector. The rightward arrows represent the field originating from a source and incident onto the object. The field is partially transmitted into the object where it dissipates in an exponential profile along its trajectory, assuming dissipative – electromagnetically absorbing – medium properties. Hence the dark zone on the right side of the object that represents the time-average intensity of the field. The zone of highest intensity in the object is located to the right, facing the source. On the interface (or boundary) between the object and the surroundings the field is partially reflected away from the object. Like the previous case, the analysis of this case is relatively simple, as it can be conducted via optical analysis, for example by ray-tracing accounting for reflection, refraction and attenuation of optical beams.

On a side-note, in case the wavelength is relatively short and in the absence of medium property variations on the wavelength scale, then energy is locally traveling in straight lines through space. This is characteristic of radiation and, therefore, the electromagnetic interactions can be considered as such. For cases with longer wavelengths relative to the objects involved in which an object is present in the direct vicinity, medium property variations occur that will affect the electromagnetic field and energy cannot a-priory be expected to travel in straight lines. Hence the electromagnetic field cannot be considered radiation. More appropriate terminology in such case would be *field* or *wave field*; these terms will therefore be maintained throughout this thesis.

The case in which the size of the object is of the same order of magnitude as the wavelength is illustrated in Figure 1.1c. Note that the wavelength λ is approximately equal to the width of the object in this case. Like in Figure 1.1a and 1.1b, the grayscale represents the time average intensity of the electric field component, which is darker for higher intensities. Around the object, the instantaneous field strength (irrespective of field vector direction) of the wave pattern that travels rightward past the object is represented by the lighter gray coloring. It is evident that the intensity distribution inside the object is much more complicated than in the former two cases. Furthermore, outside of the object, the field is affected considerably; four bands of low wave intensity stretch far outward from the object. In all, the interactions are much more complicated than in the other two cases, which is due to the wave fields that are simultaneously scattered and redirected by the object, traveling through and around it, and constructively and destructively combining, thus forming spatially complex interference patterns of high and low intensities.

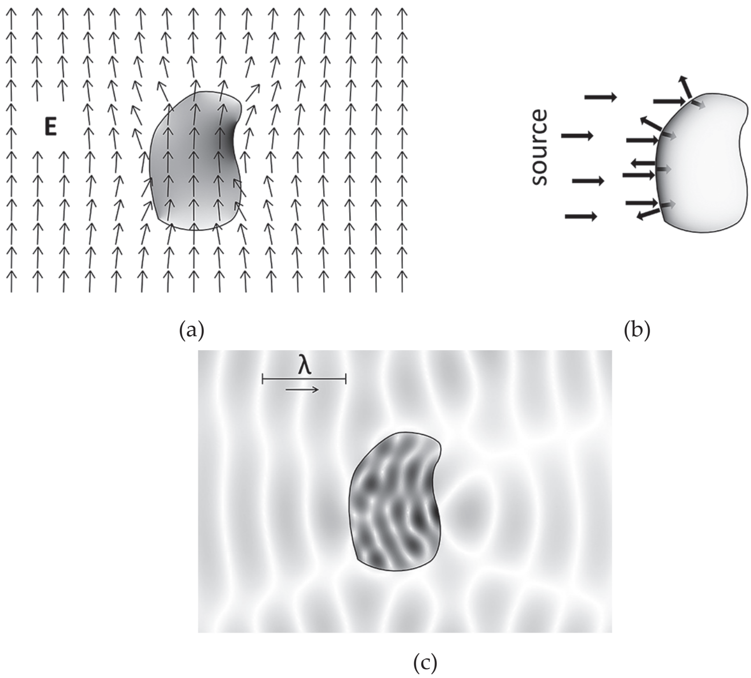

Figure 1.1. The variability of the interactions of an electromagnetic wave field with an object. Figure (a) represents the case in which the wavelength is (very) large relative to the object, (b) illustrates the case in which the wavelength is (very) short relative to the object, and (c) represents the case in which the wavelength is of the same order of magnitude as the object geometry.

The latter type of interaction – with object or equipment sized at the same order of magnitude as the wavelength – is the type relevant to microwave assisted chemistry applications; at 2.45 GHz for example, the wavelength is 122 mm in vacuum and 13 mm in water, which are length scales that are commonly encountered in processing systems. The next section therefore introduces wave interactions and a number of key concepts by means of a simple analogue system.

1.3 Waves on a string

An “excellent intuitive example” [60] of wave interactions is a vibrating tensioned string. Figure 1.2 presents this system; both ends are fixed, but on the right end a vertical displacement can be imposed. In this example, the length of the string (L) is one meter, it is tensioned (F) to 200 N and its weight per unit of length is 2.1 g/m; this would correspond to a polyamide string with a cross section of 2.75 by 2.2 millimeter that is tensioned to about a third of its breaking strength.

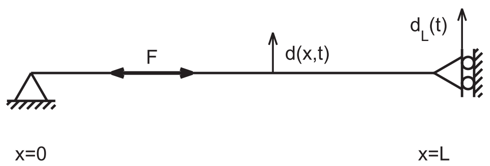

Figure 1.2. Vibrating string system. On one end of the string it is fixed in both the horizontal and vertical direction, while on the other end only the horizontal direction is fixed and the vertical displacement is an externally imposed variable. The string has a length L, it is tensioned to a force F, and its vertical deflection $d(x,t)$ varies both in time and along the position on the string.

When the string is subjected to an initial strike, this will cause the string to vibrate. The string enters an alternatingly upward and downward motion along its length. For an idealized system without damping, the vibrations endure infinitely if the system is left untouched. The vibrations that occur are a superposition of an integer number of resonance modes. These modes are patterns of oscillation that occur at specific frequencies and each of these patterns has a specific sinusoidal distribution along the length of the string. Figure 1.3 presents the deflection patterns of the string for the first four modal patterns.

This type of oscillation is termed *free resonance*, because the system is left free to oscillate after an initial excitation. Only a (possibly infinite) integer number of resonance modes can appears. This is explained as follows; the spatial oscillation pattern can be represented as a combination of forward and backward traveling waves. These waves interfere and combine constructively and destructively in a spatially alternating pattern. Only patterns that obey the boundary condition imposed on the string – no displacement on either end – can emerge. This constraints the wavelengths of the forward and backward traveling waves; an integer number of half wavelengths must fit exactly into the length of the string, otherwise the boundary condition cannot be satisfied. The patterns presented in Figure 1.3 represent modal patterns corresponding to wavelengths of $L/2$, L, $3L/2$ and $2L$. The corresponding frequencies are the speed of wave propagation along the string divided by the respective wavelengths.

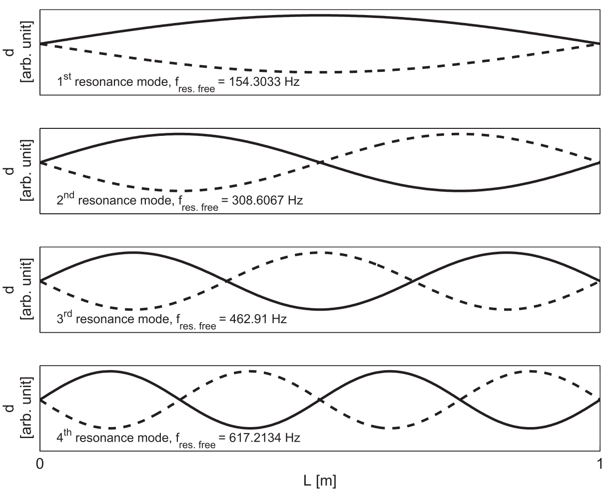

Figure 1.3. Modal patters at the first four free resonance frequencies of the string under consideration.

As opposed to free resonance, forced resonance can occur at any frequency. *Forced resonance* is the case in which a system is continuously excited by an external source of vibrations; any frequency can be applied as it is an externally imposed variable. In Figure 1.4a the deflection along the string is presented for three cases in which continuous sinusoidal excitation is imposed on the right end of the string. These excitations have frequencies of 278 Hz, 293 Hz and 306 Hz respectively and have the same maximum upward and downward deflection – or *peak amplitude* – of 1 mm imposed on the right end. As with free resonance, the deflection patterns can be represented as a superposition of interfering forward and backward traveling waves.

As is apparent from Figure 1.4a, the maximum deflection along the string varies considerably with frequency. The frequencies are chosen such that they are about 90%, 95% and 99% of the value of the second free resonance frequency; the respective maximum amplitudes are 1.7 mm, 3.2 mm and 19 mm. As the imposed frequency of excitation approaches the value of the second free resonance frequency, the deflection of the string becomes larger. This is further demonstrated by Figure 1.4b, which presents the average peak amplitude along the string versus the frequency of excitation; the nearer the excitation frequency is to a free resonance frequency, the more the vibrations are amplified. The large amplifications result from the fact that the boundary conditions have to be met; when the excitation frequency approaches a free resonance frequency, the deflection on the right end of the string must *relatively* become increasingly smaller, since at the free resonance frequency it approaches zero. Because the movement on the right end of the string is imposed, the displacement at that point cannot actually decrease; rather, the deflection only shrinks in relation to the vibrations along the string, which is expressed by increasingly amplified vibrations.

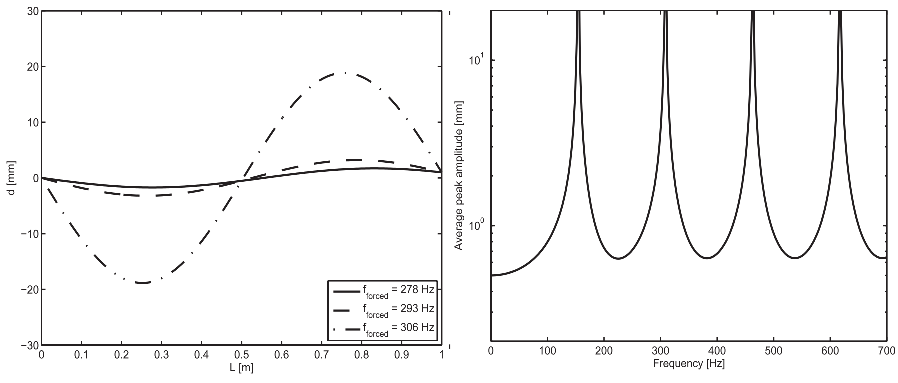

(a) (b)

Figure 1.4. Deflection of the string under forced resonance. Figure (a) presents the modal patterns of deflection under three excitation frequencies and (b) presents the average peak deflection along the length of the string.

1.4 Multimode cavities-familiar but obscure microwaves

The ubiquitous domestic microwave oven is the microwave heating system that we are most familiar with; in a culinary context, the convenience and speed it provides has – for better or worse – revolutionized preparation and consumption of our meals. At the outset it could have only seemed fitting to investigate these systems as an alternative means to provide energy to chemical processes. Nevertheless, upon closer inspection important limitations of these systems emerge.

Some of the practical limitations have already been addressed in similar laboratory systems [61-64]. These systems essentially are domestic microwave with a number of laboratory-specific features; for example, these devices come equipped with strengthened and lockable doors, finely controllable microwave sources, temperature control interfaces, access for inlet flows, outlet flows and sensors, and arrangements for continuous stirring. Aside from the different features, the construction of both the domestic and laboratory systems amounts to a rectangular metal box with a door on the front side and dimensions that range in the order of 20 cm to 50 cm. Typically a microwave field is generated by a magnetron tube and this field is led into the cavity by a short waveguide.

A more conceptual problem that both the domestic microwave ovens and these laboratory systems suffer from is implied in the generic name of these types of systems: they are *multimode* microwave system, which means that their cavity supports multiple resonance modes in the vicinity of the operating frequency [65-66]. Despite the geometrical simplicity, the electromagnetic analysis of these systems is very complicated.

Similar to the string in the previous section, the cavity supports a number of resonance modes, but in contrast to the string the number of resonance modes is much higher. This is a consequence of the three-dimensionality of the cavity and the variable directionality of the microwave field vectors; in brief, the microwave fields in these cavity systems have many more degrees of freedom than the vibrations on a string. In addition to this, the frequency spectrum of a magnetron is impure and relatively wide banded [65,67-68]. The combined consequence is that it is impossible to adequately determine the energy distribution over the free resonance modal patterns that are excited in this frequency band. Because the spatial field distributions of the respective modal patterns are very different, the final consequence is that the spatial distribution of the resulting microwave field becomes impossible to predict for practical purposes.

Further, as was demonstrated by the string example, small parametric variations can cause large effects on modal field patterns; they cause some modes to become stronger while other modes become weaker. Hence, the electromagnetic field is very sensitive to variations in geometries and in the medium properties of objects and fluids. As the modal patterns stretch over the entire spatial domain that is involved with the electromagnetic field, local variations cause global effects. Therefore, the introduction of objects in the field as well as variations in geometries and in medium properties change the field pattern globally. This adds to the complexity of the analysis, because, in the context of chemical processing, there are many phenomena that are likely to affect the spatial distribution of the electromagnetic medium properties. Examples in this respect are: progressing reaction coordinates, limited manufacturing tolerances of glassware, and hydrodynamic variations of fluids. Although mode stirrers have been suggested to improve microwave field uniformity [65], effectively these stirrers only add to the complexity of the problem, because they introduce yet another varying parameter that affects the field.

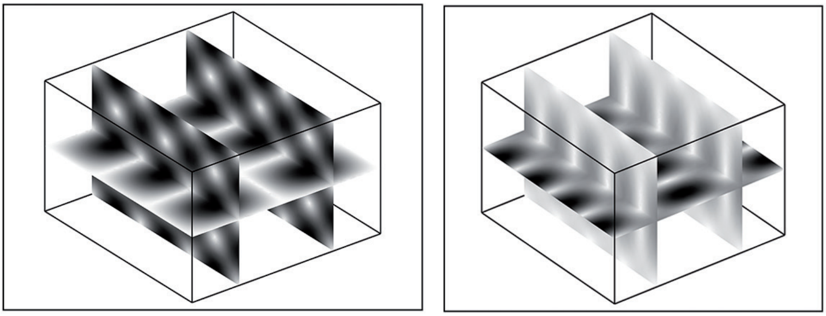

Figure 1.5. Modal patterns inside a 285 mm by 290 mm by 190 mm applicator cavity at a 2.449724 GHz resonance frequency (left) and at a 2.45032 GHz resonance frequency (right). The figures present slice plots of the electric field amplitude; darker zones concur with higher field intensity.

To demonstrate these issues a few experimental and modeling results are presented here for a typical domestic microwave oven (Sharp R-2S57). This oven has a 285 mm by 290 mm by 190 mm applicator cavity. For an empty rectangular cavity it is possible to analytically calculate the free resonance modes [69]; within a 30 MHz frequency band – typical for magnetron tubes – around a 2.45 GHz center frequency this cavity supports six free resonance modes. The system is therefore a multimode system. Inserting a load does not change this; while this may cause some resonance modes to shift out of the generated frequency band, it will also cause other resonance modes to shift into this spectral band. Via modal analysis in Comsol Multiphysics 3.5 with the RF-module [70], two spatial patterns of the distribution of the electric field strength were calculated for two free resonance modes that this cavity has around 2.45 GHz. Figure 1.5 presents these spatial field strength distributions; their spatial distributions differ considerably even though only a very small 0.6 MHz frequency variation would cause a shift from one to the other.

Thermal imaging was used to experimentally demonstrate the behavior of the microwave field in this microwave oven. Figure 1.6 presents thermal images (SP Thermoview 8300) of an expanded polystyrene plate supporting a thin water film heated in a multimode cavity; these images were made following a procedure from Karstädt et al. [71]. The images clearly show the non-uniformity of the resonant microwave field in the horizontal plane. Furthermore, these images demonstrate the dependence of the microwave field on the vertical direction; compare Figure 1.6a and Figure 1.6b, where the wet surface is at a height of 40 and 120 mm respectively above the cavity bottom. The resonance patterns between these images bear no similarity. Further, in Figure 1.6c, a water filled beaker is introduced in the cavity. The microwave field pattern that presents itself in the empty space of the cavity via thermal imaging is affected by the introduction of the beaker, which is most notable in the far left corner. *As mentioned before, a local variation – the introduction of the beaker – affects the microwave field globally, i.e. throughout the cavity.*

Although the above demonstrations reveal the sensitivity of the microwave field in the empty space of a multimode cavity, they do not show the effects on the heating rate distribution inside a load. In order to illustrate the heating rate distribution inside a typical load, the microwave field is simulated in the microwave oven with a 250 ml beaker containing 200 ml water placed centered on the floor of the cavity. Figure 1.7 presents slice plots at a height of 30 mm above the cavity bottom at a frequency of 2.45 GHz (Figure 1.7a) and at a slightly shifted frequency of 2.46 GHz (Figure 1.7b).

The simulations demonstrate the high degree of sensitivity to disturbances inside a load in a multimode microwave field; only a small frequency shift may double the total energy absorption. Note that these large effects are only due to small variations in the morphology of the microwave field caused by the frequency shift.

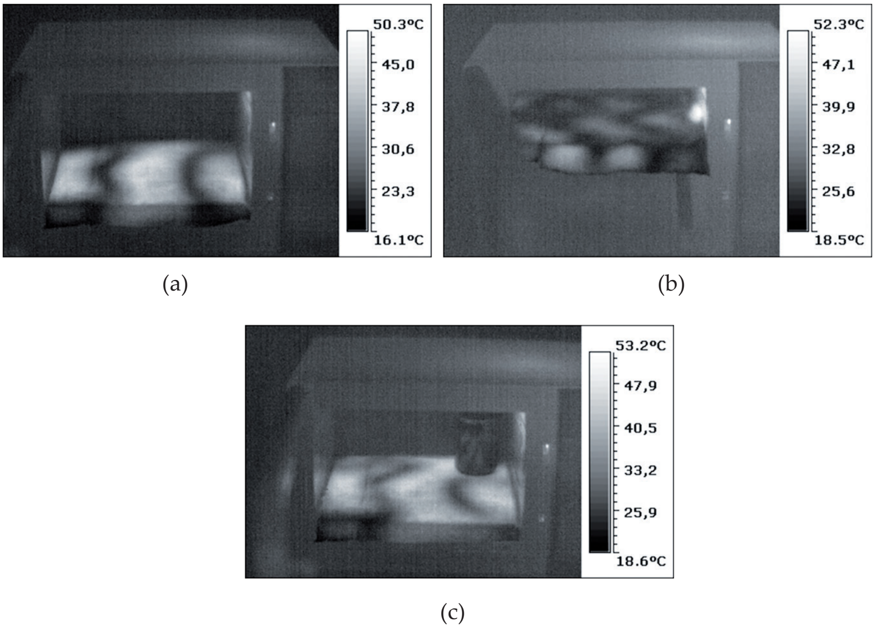

Figure 1.6. Thermal imaging of a water film in a multimode cavity, similar to Karstädt et al. [71], with the film 40 mm above on the cavity bottom (a); at a height of 120 mm above the bottom (b); and with the film at the 40 mm position with a water filled beaker placed into the cavity (c). The complex field patterns in the plane of the film change with the height and the introduction of the beaker. Note that, as opposed to the other images in this section, the colormap used in this image shows the highest intensity at the lightest color.

Further, the results show that there is an interference pattern of alternating high and low electromagnetic dissipation inside the water volume. This is supplemented by Figure 1.8, a multiple-slice plot in a different projection to show the three-dimensional distribution. This interference pattern does not even remotely follow an exponentially decaying trend as would be expected if in the analysis the microwave field would be performed using the ray (or optical) approximation. Upon occasion such modeling approximation has been proposed [72] but more regularly, studies mention the existence of penetration depth limitations. In both these discussions the microwave field is described using the ray (or optical) approximation. This simulation suggests that for this water filled beaker and for all systems similar to it – which essentially includes the whole field of microwave assisted chemistry – *wave field physics would be more appropriate on this geometrical scale relative to the wavelength.*

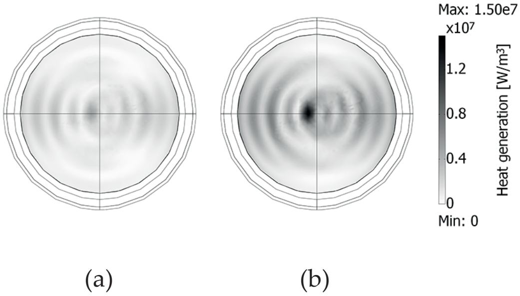

Figure 1.7. Slice plot, 30 mm above cavity bottom, of the heating rate in 250 ml beaker filled with 200 ml water ($\varepsilon_r = 77 - 13i$) placed in the middle of a 190 mm × 290 mm × 285 mm (h×d×w) cavity with a 1000 W field fed into the cavity. In the left figure (a) the field has the nominal frequency of 2.45 GHz, while in the right figure (b) the frequency has shifted slightly by 10 MHz. In both simulation results, the interference pattern is quite apparent; note that the shape has varied subtly. More obvious is the increase in heating rate for the shifted frequency; the overall heat generation in the water contained in the beaker has more than doubled. *At 2.45 GHz the absorbed power is 370 W, while at 2.46 GHz the absorbed power is 770 W.*

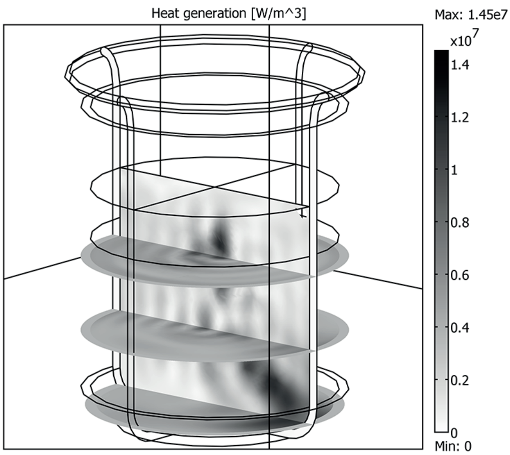

Figure 1.8. Three-dimensional slice plot of the heat generation in the water filled beaker heated in a multimode cavity described in Figure 1.7 at a frequency of 2.45 GHz. A complex three-dimensional interference pattern appears in the water volume. *The spatial distribution of heat generation does not at all resemble an exponentially decaying trend* that would be expected if one would predict the field intensity based on the penetration depth of a microwave field at this frequency in water (13 mm).

In all, what the analysis on multimode systems in this section shows, is that the microwave field in such systems is affected by insufficiently manageable parametric variations, which make this field impossible to predict for practical purposes. Further, the spatial distribution of the field forms complex and ill-defined patterns without any possibility for control nor for optimization. Recall that the discussion on the combination of micro- and millistructured processing systems with microwave activation explicitly highlights the high degree of control as a promising potential advantage. Combining these processing systems with the microwave ovens the world is familiar with will surely not yield such advantage; the exact microwave conditions in multimode cavities are very obscure, thus completely defeating the purpose of micro- or millistructured processing. The electromagnetic aspects of these microwave enhanced processing systems need to be addressed in a radically different manner to reach successful applications. This will be done in this thesis.

1.5 Research questions and outline of thesis

This study primarily aims to investigate the possibilities to apply a microwave field in microstructured reactor systems. As was pointed out in the previous section, the microwave systems we are most familiar with are not suitable at all for this purpose. A different kind of equipment design is required to introduce microwave fields in microreactors effectively. The aim of this thesis thus is directed toward the design of equipment in which chemical processing aspects are adequately integrated with electromagnetic aspects. In order to determine how these objectives can be achieved the following research questions are formulated:

1. In accordance with the process intensification principles as defined by Van Gerven and Stankiewicz [8], a uniform distribution of the microwave field strength would aid the objective of giving each molecule the same processing experience. What are the physical limitations for obtaining a favorable, spatially uniform distribution of the microwave field?
2. What are the limitations of resonant cavity microwave applicator systems? Aside from the possible emergence of multiple modal patterns, are their additional limitations to those microwave systems that are commonly utilized in microwave chemistry research?
3. What design requirements have to be met in the design of microwave processing systems in order to acquire a predictable, controlled and optimized microwave field? What physical properties have to be taken into account to satisfactorily predict the microwave field?

4. Can the resonant conditions that inherently entail a non-uniform distribution of the electromagnetic field be avoided? What would be the design of such a systems?
5. What design principles or guidelines can be derived from the answers to the above questions? In the broader context of electromagnetically enhanced chemical processing, can these be generalized to apply to systems other than microwave enhanced microreactors?

This dissertation is to the best of our knowledge the first attempt to systematically explore the possibilities of applying a controlled microwave or electromagnetic field in a microreactor system. The remaining five chapters of this thesis address the research questions stated above; these chapters are outlined as follows.

Chapter 2
In this chapter, two simple configurations with well-defined single-mode field patterns, namely a cylindrical and a rectangular cavity both containing a homogeneous cylindrical load were analyzed either analytically or numerically. The physical limitations on field homogeneity are investigated. It was found that load size, heating uniformity and desired frequency mutually constrain one another. Design charts are presented that illustrate how important operating, geometric and materials parameters relate to each other. It is demonstrated how these simple configurations can provide design guidelines and first approximations for more realistic process equipment geometries.

Chapter 3
Chapter 3 investigates the physics of a resonant microwave field by means of an extended case-study. This system herein is a highly celebrated off-the-shelf single-mode laboratory device (CEM Discover) that heats a simple water filled vial. Both the heating rate distribution and the overall heating rate are investigated as well as the sensitivity of these measures to parametric variation. The sensitivity and non-optimizability are demonstrated by means of experiment and simulation. Conclusions regarding resonant fields in cavity applicators in general are drawn.

Chapter 4
In the context of microwave enhanced chemistry, usually a narrow set of single- and multimode cavities is considered as microwave field applicator. This chapter aims to widen this current scope by exploring the potential of rectangular waveguides as a basis for microwave applicator systems. It is demonstrated that such systems offer microwave field patterns that are relatively simple and predictable, which makes processing amenable for adaption to specific requirements and for optimization. The feasibility of long residence time continuous flow chemistries

under microwave conditions is demonstrated in a novel reactor type that the rectangular waveguide uniquely supports.

Chapter 5

This chapter proposes a novel coaxial traveling microwave field applicator that avoids the resonant fields of currently used microwave heating equipment. The aim is to avoid problems associated with resonance, namely, hard-to-predict electromagnetic field patterns, difficulty in controlling and optimizing heat generation, and intrinsic spatial non-uniformity. The concept is presented as a means to retain the highly optimized processing conditions that are characteristic for microreactor systems both in the context of liquid phase processing and in the context of gas phase, solid catalyst processes. A method to optimize the applicator geometry is demonstrated.

Chapter 6

The last chapter summarizes the findings of the thesis and lists the design principles that were found. Additionally it proposes a framework for further development of equipment for electromagnetically enhanced chemical processing systems.

Chapter 2

Standing wave fields and limits on field uniformity

As pointed out in the previous chapter, resonant microwave fields in cavities inherently do not have evenly distributed field intensity. This poses limitations on the processing volume that effectively can be heated uniformly. To investigate the inherent limitations, two simple hypothetical electromagnetic field applicator configurations are analyzed and from this analysis two design charts are derived that illustrate how important operating, geometric and materials parameters relate to each other. It is demonstrated that in the popular 2.45 GHz band the spatial domain available for processing with a homogeneously distributed field is severely constraint. Furthermore, it is shown that the relations found for the operating, structural and material properties on the basis of these simple configurations can provide design guidelines and first approximations for more realistic process equipment geometries.

The contents of this chapter were adapted from the work published in:

G.S.J. Sturm, G.D. Stefanidis, M.D. Verweij, T. van Gerven, A.I. Stankiewicz
"Design principles of microwave applicators for small-scale process equipment"
Chem. Eng. Process. 49 912-922, 2010; doi:10.1016/j.cep.2010.07.017

2.1 Cavity applicator of reduced complexity

The observation of the previous chapter that microwave fields in cavities are inherently non-uniform leads to an important question with respect to the design of process systems with well-controlled activation by microwave fields: *how non-uniform is it?* The uniformity of the microwave field is a critical aspect, as one of the process intensification principles defined by Van Gerven and Stankiewicz [8] is to give each molecule the same processing experience. In this chapter it is investigated how uniformity in cavity systems is affected by geometrical and medium parameters, and what the limitations are on the uniformity of heating under microwave conditions. In this context a system of reduced complexity is considered in order to derive key relations between the parameters.

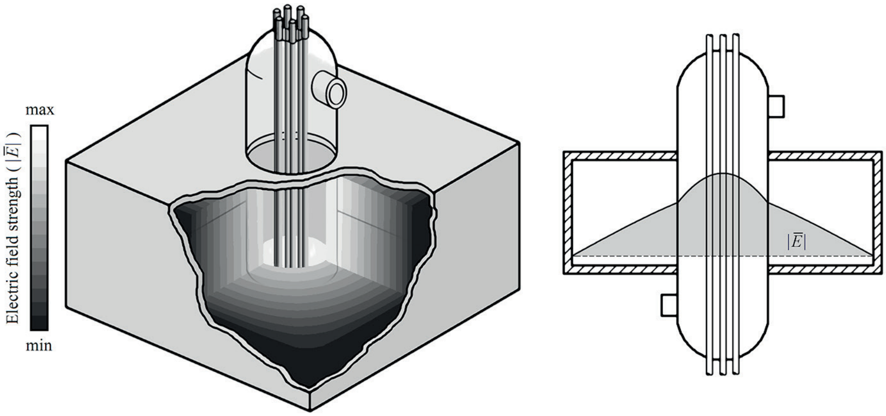

Figure 2.1. Representation of the electromagnetic heating systems envisioned in this chapter. Left: Shell and tube reactor partially enclosed in a single-mode heating cavity. Right: Transverse electric field intensity distribution.

The combination of process equipment and electromagnetic heating cavity that is considered in this chapter is represented by Figure 2.1. A cylindrical processing system – a shell and tube reactor in case of Figure 2.1 – is partially enclosed in an electromagnetic resonance cavity. In order to have a well-defined field the cavity is operated in a single resonance mode. Electromagnetic energy is externally generated and fed by some means into the cavity. There it induces a resonating electromagnetic field that extends throughout the entire cavity. As was explained in the previous chapter, this form of resonance would be forced resonance, but since we focus on the applicator parameters, we avoid the electromagnetic circuitry supplying the energy. Instead, in our analysis we consider the frequency and field distribution of the first free resonance mode. Considering the free resonance mode rather than forced resonance is acceptable in this case, because, in any case, in order to obtain good energy coupling, the forced resonance system would need to be operated near a free resonance mode. The rectangular cavity in Figure 2.1 depicts the distribution of the electric field component of this first resonance mode. In case of this rectangular cavity it is denoted as the TE_{101} mode, for which the spatial distribution is invariant with height and which has one field maximum centered in the cavity. By placing the load in and along the electromagnetic field maximum, gradients in the field distribution are minimized, thereby maximizing the heating uniformity.

In this frame, two simple configurations of a cavity with a cylindrical load are investigated, namely a cylindrical and a rectangular cavity. As opposed to Figure 2.1, cylindrical loads of homogeneous, temperature and frequency invariant properties are considered in the analysis. Heat generation – or, equivalently, electromagnetic dissipation – is examined, but not heat accumulation, heat transfer and temperature variations. Although these are unarguably big simplifications, they allow for the reduction of system descriptors to a small set of only three parameters. This enables insight into manipulation and interplay of critical system parameters in relation to heating uniformity. Given that the uniformity of heating is a key parameter in this chapter, the following definition is formulated for it: the uniformity of heating is the ratio of the minimum volumetric heat generation rate in the load to the maximum volumetric heat generation rate in the load, or,

$$HU = \frac{q_{load,\min}}{q_{load,\max}} \tag{2.1}$$

This chapter investigates how cavity size, load size and load permittivity affect the heating uniformity and resonance frequency. It is emphasized that due to the number of simplifications adopted, the quantitative analysis is meant to roughly quantify the interactions of system parameters rather than to provide accurate predictions. Nevertheless, the relations between the aforementioned parameters of the very simple configurations are shown to provide rough initial design guidelines for more realistic process equipment geometries that are relevant to chemical industry. These may include, but are not limited to, static mixers, shell and tube heat exchangers and micro and small-structured reactors.

2.2 Cylindrical cavity

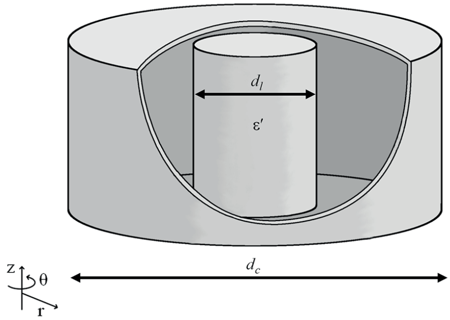

Figure 2.2. Simplified cylindrical cavity configuration.

A cylindrical single-mode resonant cavity with a homogeneous non-absorbing cylindrical load at the center, as depicted in Figure 2.2, is analyzed. The fundamental mode for this system is TM_{010} [69]. The number of descriptors of this system is just three, as opposed to configurations found in reality, which have many more. These variables are: the cavity diameter (d_c), the diameter of the cylindrical load (d_l) and the relative permittivity of the load (ε'). The above hold upon the following assumptions: 1) the cavity height is sufficiently low to prevent standing wave patterns from being formed in the axial direction; in other words, there is electromagnetic field invariance in this direction, thus eliminating the height dimension and reducing the components of the electric field vector to just E_z [69]. Furthermore, since the configuration is concentric, the system is also invariant in the tangential (θ) direction. What remains is a configuration that depends on one dimension of a cylindrical coordinate system. 2) Modal field patterns of resonance cavities are characteristic of the cavity and its load only, and they can be calculated by modal analysis of the cavity with its load. Although cavities are brought into resonance by adequate supply of electromagnetic energy, the manner energy is introduced does not affect modal patterns. It is therefore assumed that energy is supplied adequately without further regard for the specific way this is done. Finally, 3) the effect of the dielectric loss factor (ε'') of the load on the modal pattern is assumed to be negligible. The dielectric loss factor is the material property that determines the time-averaged rate of heat generation in a material subject to an oscillating electric field according to,

$$q = \pi f \varepsilon_0 \varepsilon'' \mathbf{E} \cdot \mathbf{E}^* \tag{2.2}$$

where $\mathbf{E}^*$ denotes the complex conjugate of the electric field vector **E**. In our case, with the linearly polarized electric field vector in the z-direction, Eq. 2.2 reduces to,

$$q = \pi f_r \varepsilon_0 \varepsilon'' \left| E_z \right|^2 \tag{2.3}$$

2

in which f_r is the resonance frequency of the cavity containing the load and in which $|E_z|$ is the peak amplitude of the electric field (maximum field intensity during oscillation).

In this chapter the dielectric loss factor (ε'') is assumed to lump together dielectric heating related with the imaginary part of the complex relative electric permittivity and conductive heating related with the electric conductivity σ. Lumping together these properties is acceptable, because in practice their respective contributions to heat generation cannot be determined separately [73]. The assumption that the dielectric loss factor has negligible effect on the electric field strength $|E_z|$ is acceptable, because commonly it is small with respect to the dielectric permittivity (e.g.: $\varepsilon_{r,water} = \varepsilon'_{water} - i\varepsilon''_{water} = 80.4 - 9.889i$ at room temperature and frequencies around 2.45 GHz [74]). Furthermore, since frequency is uniform throughout the system and the dielectric loss is uniform over the load, the heating uniformity according to Eq. 2.1 can be redefined via Eq. 2.3 as,

$$HU \approx \frac{\left| E_z \right|^2_{load,\min}}{\left| E_z \right|_{load,\max}} \tag{2.4}$$

From Eq. 4, it is concluded that the heating uniformity depends only on the on the modal pattern (note that the dielectric loss terms in the numerator and denominator are canceled out).

Because of its simple concentric one-dimensional configuration, the electric field distribution in the cylindrical cavity can be derived analytically. The modal field patterns turn out to consist of a set of Bessel functions, J_0 and Y_0, over the radial direction.

$$\begin{cases} E_z(r) = A_1 J_0\left(2\pi f_r r \dfrac{\sqrt{\varepsilon'}}{c_0}\right) & \text{for } 0 \le r \le \dfrac{d_1}{2} \\ E_z(r) = A_2 J_0\left(2\pi f_r r \dfrac{\sqrt{\varepsilon'}}{c_0}\right) + B_2 Y_0\left(2\pi f_r r \dfrac{\sqrt{\varepsilon'}}{c_0}\right) & \text{for } \dfrac{d_1}{2} \le r \le \dfrac{d_c}{2} \end{cases} \tag{2.5}$$

The coefficients A_1, A_2 and B_2 and the resonance frequency f_r can be calculated for any configuration with parameters d_c, d_l and ε'. More information on the derivation of these equations can be found in Appendix A. It is noted that the relation for the field pattern in the load is the same as for radio frequency heating of a cylindrical load between two circular electrodes [75].

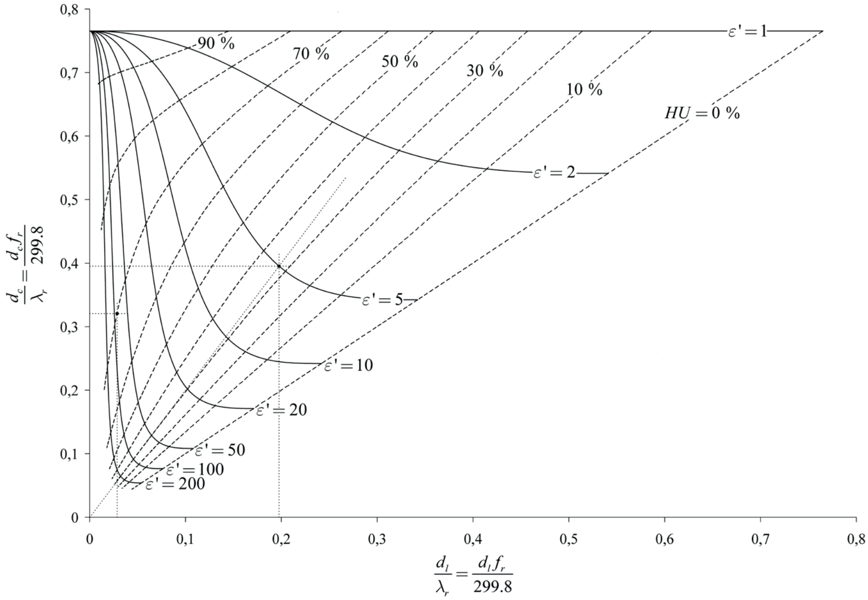

Figure 2.3. A chart relating the system parameters in the simplified cylindrical cavity configuration of Figure 2.2. The parameter set consists of: cavity diameter (d_c) [mm], load diameter (d_l) [mm], relative permittivity of the load (ε') [-], resonance frequency (f_r) [GHz], resonance vacuum wavelength (λ_r) [mm] and heating uniformity (*HU*) [-]. The dotted lines refer to the examples in the text.

The relations in Eq. 2.5 were implemented in MATLAB [76] to draw a chart that relates the system parameters d_l, d_c, ε', f_r (= c_0 / λ_r) with *HU* (Figure 2.3). This chart presents the characteristics of the system in terms of d_c / λ_r versus d_l / λ_r (ratio of the cavity diameter to resonance vacuum wavelength and ratio of the load diameter to resonance vacuum wavelength, respectively). This allows relating the ratio of cavity to load diameter and the relative permittivity to the heating uniformity independent of the resonance frequency. The solid lines are isolines for the relative permittivity and the dashed lines are isolines for the heating uniformity. In Figure 2.3, two examples are indicated by dotted lines. In the first one, a system with a ratio of $d_c / d_l = 2$ and a relative permittivity $\varepsilon' = 5$ is represented by the cross point (large black dot) with coordinates (0.198,0.395) and *HU* = 33%. If the load diameter in this system is 10 mm, it follows that λ_r = 10/0.19 = 51.3 mm and the resonance frequency f_r = 299.8/52.6 = 5.85 GHz. In the second example, a water load (ε' = 80.4 [74]) has a required heating uniformity of 70% at a frequency of 2.45 GHz (λ_r = 122.4 mm); this system is represented by the cross point (large black dot) with coordinates (0.029, 0.318) and requires a load diameter of 3.5 mm and a cavity diameter of 39 mm. Similar calculations can be performed in any direction.

The relative permittivity isolines correspond well to those found by Metaxas [77]. The upper line for ε' = 1 lies horizontal at a value of d_c / λ_r = 0.7655 and corresponds to the first root of the zeroth order Bessel function of the first kind, divided by π. This is expected on the basis of analytic calculations for an unloaded cavity [69]. The line for $d_c = d_l$ coincides with the line for *HU* = 0%; on this line, the load touches the cavity wall and since the electromagnetic boundary conditions enforce a zero parallel electric field at a conducting wall, *HU* is 0%. Based on the chart in Figure 2.3, a number of important remarks can be made on the relation between geometry, load permittivity, frequency and heating uniformity.

- An increase in load permittivity, while keeping d_c and d_l constant, results in lower resonance frequency and lower uniformity. An increase in load diameter, while keeping d_c and ε' constant, results in lower resonance frequency and lower uniformity. An increase in cavity diameter, while keeping d_l and ε' constant, results in a lower resonance frequency and a higher uniformity.
- The chart indicates that in order to achieve high heating uniformity, the cavity and the resonance wavelength need to be rather large compared to the load. For example, to achieve an *HU* of 90%, d_c needs to be at least 5.4 times larger than d_l in case the load has a permittivity close to one (e.g. a gas). For water at room temperature (ε' = 80.4), d_c / d_l should be 48. In other words, for a high permittivity load that requires a high heating uniformity, the cavity must be very bulky as compared to the load. The resonance wavelength increases accordingly. For *HU* = 90%, λ_r needs to be at least 6.9 times bigger than d_l if ε' is close to unity. On the other hand, if the load is water, λ_r needs to be 34 times larger than d_l.
- There is an upper constraint for the value of f_r so that the *HU* requirements are met. The value of this limit decreases with an increase in load permittivity and load diameter. For the last example (water load, d_l = 10 mm, *HU* = 90%), the resonance frequency can be at most 0.88 GHz. If the popular frequency of 2.45 GHz is to be used, the load diameter must be reduced to a value of 3.58 mm in order to meet the heating uniformity requirement. The heating uniformity reaches a very low value if a 10 mm load is used; a line drawn upwards from d_l / λ_r = 10/122.8 = 0.081 crosses the line: ε' = 80.4 very close to *HU* = 0%. It can be shown [69] that if the desired frequency is higher than 2.560 GHz, the point

representing this configuration is not even on the chart. Above this frequency, single-mode TM_{010} operation is not possible for a water load of 10 mm.

Three main conclusions can be drawn based on the observations above: 1) There are constraints to what can be achieved with cylindrical single-mode cavity applicators because the load size, the requirement on heating uniformity and the desired frequency mutually constrain one another. 2) Rather bulky cavities and resonance frequencies below an upper limit are required in order to attain high heating uniformity. A cavity becomes bulkier and the frequency becomes more tightly limited if the load diameter and permittivity increase. 3) Figure 2.3 can be used as a design tool to calculate the dimensions of a cavity applicator and its load and the operating frequency in the initial design steps of an electromagnetic heating system involving realistic process equipment. This is further elaborated upon in Section 2.4.

2.3 Rectangular cavity

Besides the cylindrical configuration, a rectangular one was analyzed as well (Figure 2.4). It is a single-mode cavity with a square base, analyzed for its fundamental mode, TE_{101}. Four parameters suffice to describe this configuration: the cavity wall length (a), the cavity height (h), the load diameter (d_l), and the load relative permittivity (ε'). First, its cross-section in the xz-plane was analyzed in 2D (field is invariant with height) and in a second step, the cavity height is taken into account to investigate the upper height limit, which ensures that the system is operated in a single TE_{101} mode.

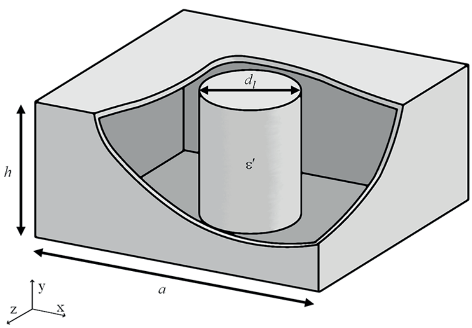

Figure 2.4. Simplified rectangular cavity configuration.

2.3.1 Cross-section analysis

The basic modeling assumptions described in the previous section were adopted for the cross section of the rectangular configuration as well. That is: 1) the cavity is assumed to be sufficiently low in order for the electromagnetic field to be invariant with height, 2) electromagnetic energy is assumed to be supplied adequately, so field patterns can be determined by modal analysis, and 3) neglect of the dielectric loss factor.

A numerical modal analysis was adopted to obtain the field patterns in the rectangular cross-section as an analytical solution for this geometry is difficult to derive. The numerical analysis was carried out with the RF-module of Comsol 3.5 [70] in a 2D model of the cross section in the xz-plane (Figure 2.4). Free mesh generation was employed for the finite element discretization with the default meshing parameters set to fine. A perfect electric conduction boundary condition was set for the edge of the geometry. Electromagnetic continuity was imposed at the interface between the load and the empty cavity space. We performed a parametric study over a wide range of the aforementioned system descriptors (a, d_l, ε') to calculate the resonance frequency (f_r) and the heating uniformity (HU) (Eq. 2.4) for a cavity resonating in the TE_{101} resonance mode. Afterwards, the simulation data was interpolated in Matlab to generate a chart that correlates the systems descriptors, the resonance frequency and the heating uniformity (Figure 2.5).

Similar to the chart for the cylindrical cavity, Figure 2.5 presents the characteristics of the system in terms of a / λ_r versus d_l / λ_r (ratio of the cavity wall length to resonance vacuum wavelength and ratio of the load diameter to resonance vacuum wavelength, respectively). The solid lines are isolines for the relative permittivity and the dashed lines are isolines for the heating uniformity. The lines connecting the open line markers are related with the height analysis and will be described later. This chart can be used to find relations among a, d_l, ε', f_r and HU for a rectangular cavity, in the same way as described for the cylindrical cavity. An example is indicated by the cross point (large black dot) of the dotted lines in Figure 2.5 for a load with a diameter of 15 mm and a permittivity ε' = 50. The load is required to be heated with a uniformity of at least 80% (the black filled circle is on the dashed isoline of HU = 80%). It is shown that under these conditions: d_l / $\lambda_r \leq 0.03$ and a / $\lambda_r \geq 0.52$. In this event, λ_r must be at least 500 mm ($f_r \leq 0.6$ GHz, that is, well below the popular heating frequency of 2.45 GHz) and a must be larger than 260 mm. All in all, the chart for the rectangular cavity is quite similar to the chart for the cylindrical one; more specifically, the general patterns are the same; $a = d_l$ coincides with HU = 0% and the top parallel line for ε' = 1 lies at a value of a / $\lambda_r = \sqrt{2}$, which is in accordance with the analytical solution for an unloaded rectangular cavity [69]. Finally, the same qualitative conclusions drawn for the cylindrical cavity in the previous section hold for the rectangular cavity as well.

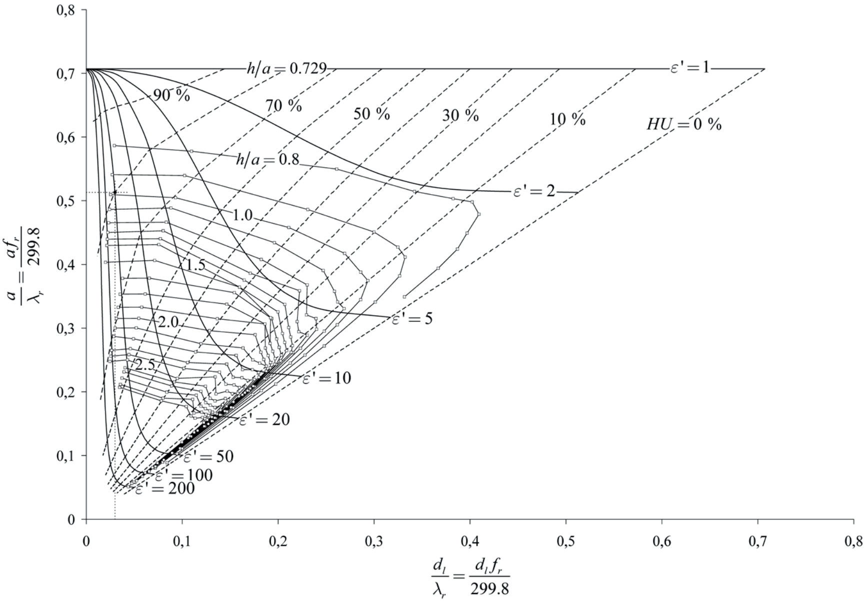

Figure 2.5. A chart relating the system parameters in the simplified rectangular cavity configuration of Figure 2.4. The parameter set consists of: cavity wall length (a) [mm], cavity height (h) [mm], load diameter (d_l) [mm], relative permittivity of the load (ε') [-], resonance frequency (f_r) [GHz], resonance vacuum wavelength (λ_r) [mm] and heating uniformity (HU) [-]. The dotted lines are added to illustrate the example discussed.

2.3.2 Maximum height analysis

In the analysis so far, it has been assumed that the cavity height is small enough so that the field is invariant with height and the electric field lines run in the vertical direction. In this section, we determine the upper limit of the cavity height to fulfill the condition above. More specifically, it was investigated at what height: 1) the fundamental resonance mode is TE_{101} and 2) the next lowest resonance frequency lies at a margin of 20% above the resonance frequency associated with the fundamental mode TE_{101}; the second lowest resonance frequency has thus 1.2 times the value of the fundamental resonance frequency. There needs to be a margin between the two resonance frequencies, because typically a resonance mode is not only being energized at one specific frequency, but over a range of frequencies. To ensure predominant single-mode operation in the fundamental resonance mode, it is therefore required that the operating frequency lies sufficiently below the resonance frequency of the mode nearest to the fundamental one. Based on practical experience, 20% is considered an adequate margin. The investigation was carried out by means of eigenvalue analysis of a three dimensional finite difference model that simulates Maxwell's electromagnetic field equations in a cavity configuration described by the 4 descriptors (a, h, d_l and ε'). The finite difference model was constructed according to Refs. [78,79] and was implemented in MATLAB for eigenvalue analysis. It yields the resonance frequencies of a cavity configuration with given descriptors. An optimization routine was employed to find the isolines defining the upper limit of the ratio of height to wall length (h / a) in Figure 2.5; they are represented by the solid lines connecting the square symbols. For any given point on the chart representing a configuration of a, d_l and f_r, these isolines indicate the maximum value for h / a for which the requirements on the resonance frequency hold. More information on the finite difference model can be found in Appendix B.

For the example indicated on the chart by the dotted lines (d_l = 15 mm, ε' = 50, HU = 80%, f_r = 0.6 GHz and a = 260 mm) the ratio h / a can be at most 1.0, which amounts to a maximum cavity height of 260 mm. In case the heating uniformity requirement is lowered to 75%, the cavity dimensions become: a = 214 mm and $h \leq$ 300 mm (λ_r = 480 mm and f_r = 0.62 GHz). For an unloaded cavity, it can be shown that the height constraint is h / a = 0.729. The results in the chart show that this constraint can be relaxed considerably by the presence of the load. Apart from verifying the proper dimensionalization of the load and the cavity as a function of heating uniformity, this chart was also used to estimate the maximum volume of a number of solvents at two ISM frequencies [58] of 0.915 GHz and 2.45 GHz for three different heating uniformity requirements (Table 2.1). The values for ε' were found in Hayes [74] for 2.45 GHz at room temperature. Based on a comparison with dielectric data from Patil [80], Kaatze et al. [81], Gabriel [82] and Meissner and Wentz [83], it appears that these values apply for 0.915 GHz quite well. They were, therefore, used for both frequencies. The ratio of cavity volume to solvent volume was calculated for the above cases too and the results are presented in Table 2.1.

The results in Table 2.1 show that at the popular frequency of 2.45 GHz the maximum volume that can be heated uniformly in this type of applicator is rather limited. Furthermore, the cavity volumes are very large compared to the load volumes. Same as in the previous section, it can be concluded that the cavity becomes very bulky as the heating uniformity requirement and load permittivity increase. In addition, it can be concluded again that load size, heating uniformity and desired frequency mutually constrain each other and that operating at a lower frequency allows for a larger volume to be heated uniformly. It is finally noted here that since the cavity dimensions scale proportionally with the resonance wavelength (for constant ε'), the required volumes scale to the third power of the wavelength.

Table 2.1. Estimate of the maximum volumes of a solvent that the cavity can heat with a given uniformity.

Solvent	ε'	f_r	**Solvent volume [ml]**			**Ratio of cavity volume to solvent volume**		
			$HU = 50\%$	$HU = 70\%$	$HU = 90\%$	$HU = 50\%$	$HU = 70\%$	$HU = 90\%$
Water	80.4	2.45 GHz	1.3	0.79	0.26	16	120	1300
		915 MHz	25	15	5.1	16	120	1300
Formic acid	58.5	2.45 GHz	2.0	1.4	0.27	13	87	1300
		915 MHz	39	28	5.2	13	87	1300
DMF	37.7	2.45 GHz	2.7	2.1	0.60	13	70	580
		915 MHz	51	41	12	13	70	580
Ethanol	24.3	2.45 GHz	3.9	3.1	1.1	14	65	330
		915 MHz	75	60	21	14	65	330
Isobutanol	15.8	2.45 GHz	6.5	5,2	1.7	12	44	220
		915 MHz	130	100	33	12	44	220
Acetic acid	6.2	2.45 GHz	17	6.6	3.4	9,1	33	110
		915 MHz	320	130	65	9,1	32	110
Toluene	2.4	2.45 GHz	30	20	5.7	7,3	14	70
		915 MHz	570	390	110	7,3	14	70

2.4 Simplified geometries as approximation of realistic process equipment geometries

In this section, we test the validity of the chart in Figure 2.5 for providing satisfactory approximations of the dimensions of the cavity and operating frequency for a targeted heating uniformity requirement in small or microstructured process equipment. The predictions of the chart (graphical method) are validated against the predictions of Comsol 3.5 (RF-module) for 18 model events. This is further analyzed as follows: two heating uniformity requirements (70% and 90%) are applied to three different solvents in three types of small-scale process equipment. These solvents are water, DMF and ethylene glycol with complex relative permittivities of $\varepsilon_r = 80.4 - 9.89i$, $37.7 - 6.07i$ and $37.0 - 50.0i$, respectively [74]. The equipment considered is a shell and tube heat exchanger at two different

2

sizes, and a static mixer. Figure 2.6 presents the cross-sections of the investigated process equipment. The larger shell and tube heat exchanger has an outer diameter of 40 mm and contains 7 borosilicate tubes (ε_r = 4.82 − 0.026*i* [69]) with an inner diameter of 5 mm. The smaller one has an outer diameter of 20 mm and contains 19 tubes with an inner diameter of 1.2 mm. In a heat exchanger, the type of coolant may vary; therefore, a relative permittivity value representative for low-absorbing liquids is applied (ε_r = 2.0 − 0.000*i*). Possible coolant options are hexane, toluene [74] or the less flammable silicone oil [84]. The static mixer has an outer diameter of 20 mm and although in reality the mesh structures are not invariant with height, this assumption is made in this work to allow for a two dimensional approximation of the geometry. The material of the mesh structure is PTFE (ε_r = 2.08 − 0.0008*i* [69]).

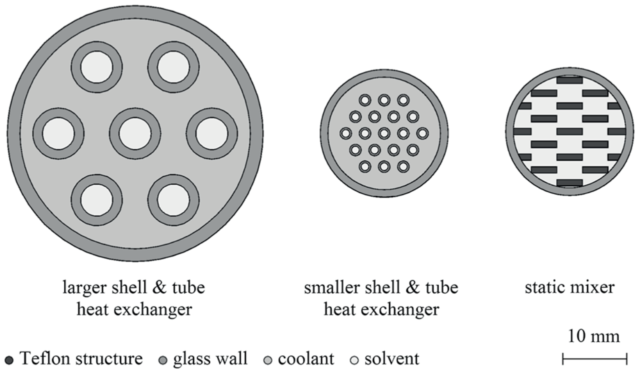

Figure 2.6. Three process equipment configurations.

Numerical method

The design procedure in Comsol 3.5 (same mesh details as in the previous section) to optimize the cavity dimensions for a required heating uniformity was as follows: First, each one of the design configurations of Figure 2.6 is placed in the center of a square domain that represents the cavity. Subsequently, modal analysis is performed to calculate the TE_{101} mode for the combination of process equipment and cavity. Note that in this numerical modal analysis, the effect of the dielectric loss factor ε'' on the modal pattern is accounted for. These steps are then repeated while adjusting the cavity wall length until the uniformity is within 1 percentile unit of the required value. The results of the Comsol simulations for the design cases are presented in Table 2.2 and indicated as "numerical method".

Table 2.2. Predicted cavity dimensions and resonance frequency for the 18 modeling cases based on the process equipment configurations in Figure 2.6.

Cross section type	Solvent	Average ε' of load [-]	*HU* required	Graphical method					Numerical Method	
				a [mm]	f_r [GHz]	*h* mm	Solvent volume [ml]	Ratio of cavity to solvent volume	*a* [mm]	f_r [GHz]
Larger shell and tube heat exchanger	Water	11.29	90%	590	0.33	430	60	2500	720	0.28
			70%	240	0.61	260	37	420	340	0.48
	DMF	6.62	90%	450	0.44	330	45	1500	580	0.35
			70%	200	0.78	180	25	290	250	0.67
	Glycol	6.55	90%	450	0.44	330	45	1500	600	0.34
			70%	200	0.78	180	25	290	310	0.57
Smaller shell and tube heat exchanger	Water	7.98	90%	210	0.73	150	3.2	2000	310	0.65
			70%	120	1.29	100	2.2	620	150	1.14
	DMF	5.06	90%	210	0.95	150	3.3	2100	250	0.81
			70%	95	1.68	76	1.6	420	115	1.51
	Glycol	5.02	90%	210	0.95	150	3.3	2100	250	0.81
			70%	95	1.68	77	1.6	420	130	1.37
Static mixer	Water	47	90%	550	0.34	400	72	1700	700	0.28
			70%	180	0.59	320	58	180	250	0.51
	DMF	22.7	90%	390	0.50	280	50	830	500	0.40
			70%	150	0.86	200	35	130	190	0.74
	Glycol	22.3	90%	390	0.50	280	50	830	550	0.37
			70%	150	0,85	200	34	130	250	0.57

Graphical method

To use the chart in Figure 2.5, a representative value of the real permittivity of the process equipment needs to be computed; this is simply assumed to be the volume weighted average of the real permittivities of the equipment materials and fluids. Then, based on this mean permittivity and the given diameter of the process equipment as well as the required heating uniformity, the resonance frequency and the wall length can be found on the chart as described earlier. The relevant results for the 18 cases described above are presented in Table 2.2 as well, under the head “graphical method”. Note that, as the results in Figure 2.5 are also based on Comsol simulations, the term “graphical method” is meant for distinction between these and the Comsol simulation results for the process equipment studied in this section. Finally, the chart-based estimates for the cavity height, the solvent volume and the ratio of cavity volume to solvent volume are also quoted in Table 2.2.

By comparing results in Table 2.2, it can be concluded, that the chart underpredicts the wall length by ~20 – 35% and overpredicts the resonant frequency by ~20 – 35%. This is primarily attributed to the assumptions of absence of dielectric loss and load uniformity. A smaller contribution originates from reading inaccuracies and interpolation errors. It is noted though, that both the direct Comsol simulations as well as the chart, which was generated for the simplified geometry (homogeneous load) exhibit the same trends, indicating that the chart gives a good first approximation of the required cavity size and resonance frequency. Besides, the resonant frequencies are all far lower than the commonly applied frequency of 2.45 GHz. This means that the required heating uniformities cannot be achieved at a frequency of 2.45 GHz. Inversely, in order to heat these types of load uniformly at 2.45 GHz, the load dimensions need to be restricted to a few millimeters. It is again observed that this type of applicator does not yield compact equipment; the volumes of the cavities are very large compared to the volume of the solvent.

2.5 Relevance with respect to practical systems

It needs to be remarked that the results presented herein are not sufficient for full understanding and design of a real heating system employing a single-mode microwave or high frequency radiowave heating cavity. In reality, a number of issues will complicate the design and analysis. The one most likely to be encountered is the fact that the permittivity of materials varies with temperature and thus in time and space in contrast to the assumption of a homogeneous permittivity adopted in this chapter. The variable permittivity may give rise to hot spot formation that would affect the electromagnetic field pattern such that the field intensity would become more concentrated on the hot spot. This could potentially lead to a thermal runaway. Furthermore, the presence of several uncertainties may result in experimental observations that deviate from the outcome of the modeling process. Such uncertainties are concerned with the limited accuracy of dielectric properties measurement and the unavailability of dielectric property data for many substances at the required frequency as well as manufacturing imperfections. These issues reconfirm that the results presented in this chapter are meant to give a good initial approximation for the design of heating cavity systems that require a well-defined and uniform heat generation field. Practical systems will always need to have adequate geometry modifications, and frequency and impedance matching features to compensate for perturbations [69,77]. Metaxas [77] presents a case that describes the design and manufacture of such a system.

Although this study indicates limitations on the performance of simple cavity applicators, other more advanced types of applicator systems may improve on the solvent volume and cavity bulkiness restrictions. One such option is the TE_{10n} cavity applicator that is investigated in Chapter 4 of this thesis. This versatile applicator type [65,85,86] features a resonance cavity that has a number of electric field maxima in a row. In Chapter 4 the feasibility of increasing the processing volume by applying controlled microwave conditions to multiple loads in a TE_{10n} cavity will be investigated.

Some final remarks are made here about how the applicator systems discussed in this chapter compare to applicators in commercially available microwave heating systems. The applicators discussed in this study are characterized by an electromagnetic field pattern that is invariant in one dimension and symmetrical in the others. These characteristics combined with single-mode operation offer well-defined electromagnetic field patterns. On the other hand, the lab scale single-mode applicator that is discussed in the next chapter, the CEM Discover™ Microwave Synthesis System, may at first glance appear to be symmetrical, but a closer inspection reveals that this is not the case [87]; in fact, its internal geometry is rather complex. In addition, there is no geometric and electromagnetic field invariance in any direction, so any analysis presents a full three-dimensional electromagnetic problem, which is, in general, significantly more difficult to tackle than a one- or two-dimensional problem. Most importantly, in that system heating is much less uniform, because the microwave field is not constant in one direction. The next chapter will discuss the matter in more detail.

2.6 Conclusions

In this chapter, two simplified single-mode (microwave or high frequency radiowave) cavity configurations are analyzed, namely a cylindrical and a rectangular cavity both containing a homogeneous cylindrical load. Investigation of these configurations resulted in design charts that enable the reader to understand how important operating, geometric and materials parameters relate with each other. A compilation of the most important conclusions of our analysis is given below.

- There are constraints to what can be achieved with single-mode cavity applicators. Load size, heating uniformity and desired frequency mutually constrain one another.
- At the popular frequency of 2.45 GHz there are rather limiting constraints on the volume of the load to achieve high heating uniformity. Opting for lower resonance frequencies allows for bigger load volumes to be heated uniformly.
- The cavity is rather bulky with respect to the load. The cavity volume increases, for a given heating uniformity requirement, as the load permittivity increases.
- There is an upper limit of the ratio of cavity height to wall length to ensure electromagnetic field invariance in the vertical direction. Field invariance cannot be assumed for any arbitrary cavity height.
- The design charts for the simplified geometries can be used in the first design stages of cavities hosting realistic micro- and millistructured process equipment. More specifically, they can provide initial approximations of the dimensions of the cavity and the operating frequency for targeted heating uniformities in the process equipment.

Chapter 3

Parametric sensitivity and distribution in space and time of heating by means of resonant microwave fields

The previous chapter investigated theoretical limitations to a resonant microwave field in a hypothetical single-mode cavity. This chapter presents an extensive case study into the limitations of a microwave field of a physical single-mode cavity system. Under consideration is a very simple exemplary system: a water filled vial that is heated in the CEM Discover Microwave Synthesis System. Two main aspects are studied: the distribution of the heating process in space and time, and the parametric sensitivity of the overall heat generation. The results evince highly non-uniform, transient and irregularly behaving heating processes that are very sensitive to – even minor – parametric variations. For practical purposes, it is not possible to achieve accurate prediction and control of the microwave heating process in this kind of flexible though non-optimizable heating device.

The contents of this chapter were adapted from the works published in:

G.S.J. Sturm, M.D. Verweij, T. van Gerven, A.I. Stankiewicz, G.D. Stefanidis
"On the effect of resonant microwave fields on temperature distribution in time and space"
Int. J. Heat Mass Tran. 55 3800–3811, 2012; doi:10.1016/j.ijheatmasstransfer.2012.02.065

G.S.J. Sturm, M.D. Verweij, T. van Gerven, A.I. Stankiewicz, G.D. Stefanidis
"On the Parametric Sensitivity of Heat Generation by Resonant Microwave Fields in Process Fluids"
Int. J. Heat Mass Tran. 57 375–388, 2013; doi:10.1016/j.ijheatmasstransfer.2012.09.037

3.1 An exemplary heating process

The previous chapter demonstrated theoretical limitations on the microwave field uniformity in the resonating field inside a microwave cavity. This was analyzed for a type of single-mode cavity that, by concept, would be tailored to fit particular applications. However in practice, researchers have preferred to use commercial off-the-shelf systems instead. Although it would seem appropriate to consider commercially available systems before opting for tailor-made devices, Chapter 1 already deems the entire class of familiar off-the-shelf multimode cavity systems unsuitable in the context of microreactor applications. In that chapter, it was argued that it is inherent to the concept of microreactors to have a high degree of control over the processing conditions, primarily in order to maintain an equal processing experience for all molecules. Multimode systems are incapable of delivering well-defined microwave fields and therefore they are unsuitable. As opposed to multimode cavities, single-mode off-the-shelf systems are worth exploring in more detail, however. Most prominent in this respect is the CEM Discover Microwave Synthesis System [88]. Although the processing volume this system accommodates is limited, it is a popular single-mode cavity device as it is capable of rapidly providing heat to reacting media without the need of a heat transfer surface or heat transport fluids, such as (open) flames, steam or heating oil. Importantly, the Discover employs a resonant microwave field to heat loads that are placed inside it, which means that it can serve as an exemplary system to the resonant fields of any cavity applicator.

To explore the generic off-the-shelf solutions for their applicability, this chapter presents an extended case study conducted with the CEM Discover into a simple exemplary heating process, being the heating of a water filled vial. Two main aspects are considered: first, the spatial and temporal distribution of the heat generation; and second, the parametric sensitivity of the overall heat generation in the vial.

An example of non-uniform heating in this particular device is presented by Durka et al. [49-50] for a catalytic bed in which temperature is found to vary roughly 50°C over an 8 mm distance. The present chapter attempts to probe the distribution of heat generation in more detail by combining two complementary experimental techniques. Most notable is the application of temperature sensitive dyes in the form of thermal fax paper. Fax paper has been used before to characterize patterns of microwave fields over the volume of resonant microwave cavities [66]. In this chapter it is used in combination with a set of fiber optic temperature sensors. Whereas the sensors yield temperature transients in a limited discrete number of points, the fax paper reveals the shape of the regions in which a certain temperature is exceeded over an entire cross section.

The other aspect of resonant fields that is investigated in this chapter is their sensitivity to parametric variation. Appendix C presents a very simple one-dimensional configuration that is both resonating and electromagnetically dissipating, which are both properties of resonant applicator cavities in microwave heating applications. It is demonstrated that this very simple configuration already exhibits strongly fluctuating interdependent relations between the overall electromagnetic dissipation – i.e. heat generation – and parametric variations. Via calorimetric measurements, it is investigated for the exemplary heating process considered in this chapter if and to what extent real world microwave heating is affected by parametric variations.

In addition to the experimental work, this chapter is further supplemented with numerical investigations of the process under consideration. Simulation studies of microwave processing systems have been performed in the past. Robinson et al. [89] present a numerical study of a load that is being heated in the Discover, revealing complex spatial field distributions. Another simulation study by Zhu et al. [90] of a microwave heated continuous flow system reveals complex interactions as well. The authors present a model of a tube with foodstuffs flowing through it that is exposed to a microwave field by means of a cylindrical applicator cavity at a frequency of 915 MHz. Their study shows that the distribution of heating rate “strongly depends on the dielectric properties of the fluid in the duct and the geometry of the microwave heating system.” In neither of these studies, though, was the forward and backward interaction between the microwave source and the load taken into account. In contrast, aside from the spatial distribution of the microwave field, this chapter presents numerical studies that do account for these interactions, which are achieved via microwave network analysis.

This chapter continues with a description of the microwave circuit of the Discover and the modeling methodology that is employed. Then the distribution of the field is discussed, followed by the parametric sensitivity of the heating process. The findings are finally extrapolated to the resonant fields of commercial non-tailored systems in general and to the consequences of these conditions to microwave enhanced chemistries.

3.2 Microwave circuit and flow of power

This section describes the layout of the microwave circuitry in the Discover and the flow of power in the system. Figure 3.1a presents a photograph of the microwave circuit and Figure 3.1b details its layout; it consists of two parts: the magnetron microwave source and the applicator section that directs the microwave field to the load to be heated.

The magnetron is supplied with electrical power that is controlled by electronics. An electron cloud emitted by the heated cathode filament of the magnetron interacts with the electric field caused by a high voltage between the cathode and an anode, and with the magnetic field from permanent magnets built into the magnetron. This interaction causes the generation of microwave fields [67] that are transmitted into the applicator section of the Discover.

At the heart of the applicator section is a cylindrical cavity in which the load is placed. The cavity is enclosed by a rectangular waveguide that is closed at one end and connected to the magnetron at the other end. The inner wall of the waveguide is slotted, forming a structure that efficiently couples electromagnetic energy generated by the magnetron into the cavity [65] to heat the load. A PTFE ring covers the inner wall of this cavity. The dimensions for the microwave circuit used in this study (Figure 3.1c) are based upon measurement of the outside of the microwave circuit and information from Jennings [87]. Though small relative to multimode cavities, the confined volume of the cavity results in a single-mode field that enables good coupling of microwave energy even in small loads.

Since this study deals with energy balances and efficiency, it is necessary to specify the relevant power flows in the device. Figure 3.2 gives a simplified scheme of these power flows; the symbols used to denote them are P for electrical power, S for microwave power, and Q for thermal power. Table 3.1 further specifies the power flows and the subscripts used to denote them. There is a complex pattern of forward and backward traveling microwave power in the microwave circuit and multiple definitions of the utilization efficiency of the microwave power can be specified. In this study we define it as the ratio of the thermal power usefully generated in the load to the microwave power generated by the magnetron,

$$\eta_U = Q_{load}/S_{generated} \tag{3.1}$$

Alternatively, if the small amount of conductive electromagnetic dissipation in the applicator walls is neglected it can be defined from the power balance at the connection between the magnetron and the applicator,

$$\eta_U = 1 - \frac{S_{a-m} - S_{m-a}}{S_{generated}} \tag{3.2}$$

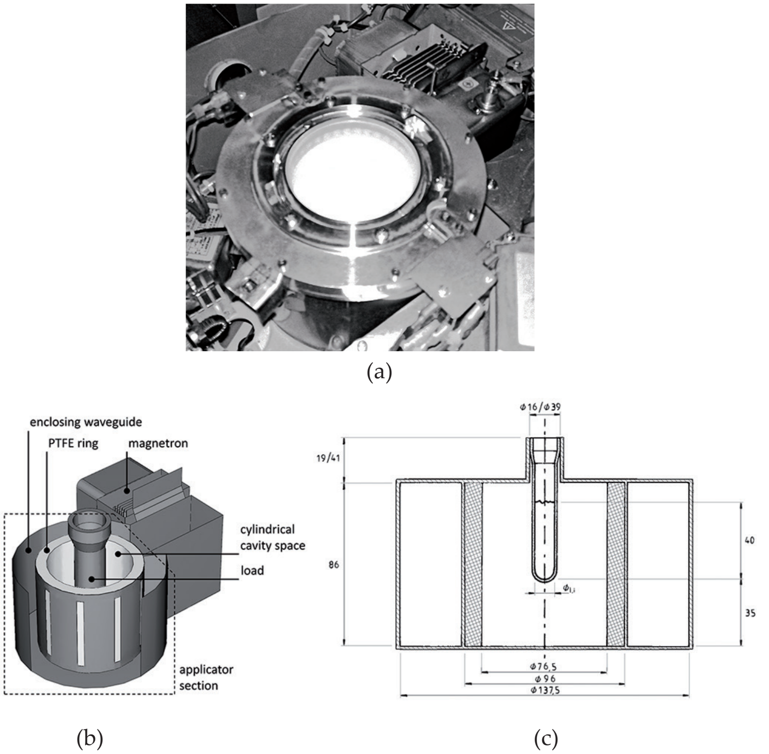

Figure 3.1. Microwave circuit of the CEM Discover: photograph (a); cut away view of the microwave circuit with main parts indicated (b); main dimensions of the microwave circuit and position of the load (c). The dimensions are in mm.

It follows that the microwave generation ($S_{generated}$) would be the upper limit for the heat generation in the load (Q_{load}). Experimentation, which will be discussed later in this chapter, has revealed that the heat generation in the load can be higher than the 300 W maximum microwave power output at which the device is rated by the manufacturer. To estimate what the upper limit for microwave power output would be in reality, the electrical power drawn from the socket is measured (Voltcraft Energy Logger 3500) first when the device is running at its maximum power and subsequently when it is running in idle mode. The idle mode power would account for the power supplied to the auxiliaries if the losses in the transformer are assumed to be negligible. The upper limit for $S_{generated}$ can be estimated by subtracting the idle mode power ($P_{aux.} \approx 25$ W) and the power used to heat the cathode ($P_{cathode} \approx 30$ W [91]) from the power drawn from the grid ($P_{grid} \approx 730$ W), which amounts to 675 W. In this calculation it is

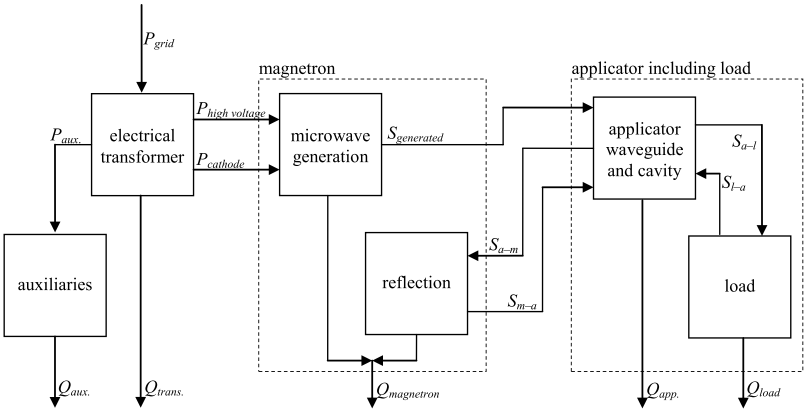

Figure 3.2. Specification of power flows in the Discover. *P* denotes electrical power, *S* denotes microwave power, and *Q* denotes thermal power. Refer to Table 1 for a description of the subscripts.

Table 3.1. Specification of the power flows (electrical, microwave and thermal) in the Discover.

P_{grid}	Electrical power drawn from grid.
P_{aux}	Electrical power supplied to auxiliary parts of the device such as fans and displays.
$P_{cathode}$	Electrical power supplied to the cathode filament in the magnetron to induce electron emission.
$P_{high\ voltage}$	Electrical power used to sustain a high voltage between cathode and electrode of the magnetron.
$S_{generated}$	Microwave power generated by the magnetron.
S_{a-m}	Microwave power reflected from the applicator section of the device to the magnetron.
S_{m-a}	Re-reflected microwave power transmitted from the magnetron to the applicator section.
S_{a-l}	Microwave power transmitted from the applicator section to the load.
S_{l-a}	Microwave power reflected from the load to the applicator section.
Q_{load}	Thermal power or heat, generated in the load by dissipation of microwave power. This is the usefully generated heat in the device.
Q_{app}	Microwave power dissipation into heat in the applicator section.
$Q_{magnetron}$	Electrical and microwave power dissipated in the magnetron.
Q_{aux}	Electrical power dissipated in the auxiliary parts of the device.
Q_{trans}	Electrical power dissipated in the electrical transformers of the device.

assumed that in the ideal case of maximally efficient microwave generation no additional dissipation of electrical or electromagnetic energy into heat occurs in the magnetron. In practice, the interactions involving the electron cloud do cause additional dissipation, so the actual microwave generation will be less than this estimated upper limit.

3.3 The loads: water filled vials

The loads considered in this study are 15 round bottomed insulated vials containing water (Figure 3.3). Table 3.2 lists the nominal and measured diameters of the vials; they are denoted by their nominal inner diameter, even though the actual diameters deviate somewhat from these values. It was decided to keep an even liquid level rather than a constant fluid volume, because the largest volume that would fit in the smallest vial would only fill a very small part of the larger vials. Expanded polystyrene blocks were fitted around the vials to insulate them. The assemblies of water filled vial and insulation were positioned in the cavity such that the vials were axially centered and the bottom of the vial was 35 mm above the bottom of the cavity (Figure 3.1c). Available with the Discover are several types of cavity lids that differ in the geometry of the access hole; the top end supports of the vials were matched either to a lid with a 16 mm diameter hole or to a lid with a 39 mm access hole, depending on the diameter of the vial (see the rightmost column of Table 3.2).

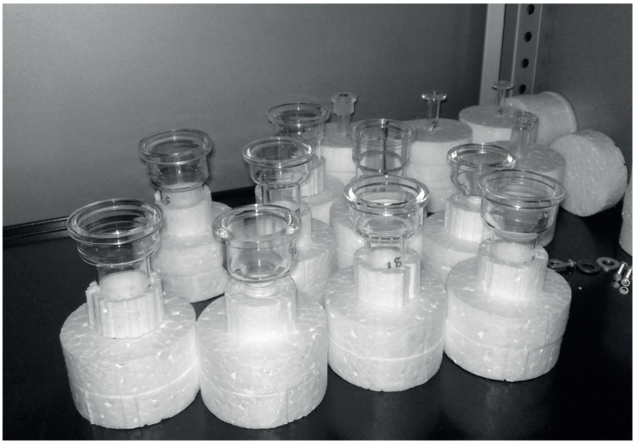

Figure 3.3. The set of vials used in this study. The inner diameters of this set range from 4 to 29 mm. Each vial has tightly fitting expanded polystyrene insulation. Note that there are two sizes of supports on top of the vials in this set; the smaller vials have a 16 mm diameter support while the larger vials have a 39 mm diameter support.

Table 3.2. Nominal and measured diameters of the vials. The vials are denoted by their nominal inner diameters, even though the actual measured diameters deviate somewhat from this value. Note that the wall thickness of the vials is either 1.5 mm or 2 mm approximately and that the vials have two sizes of supports on top: either a small one with a 16 mm outer diameter or a large one with a 39 mm outer diameter.

nominal inner diameter [mm]	inner diameter (measured) [mm]	outer diameter (measured) [mm]	top end support size
4	4	7	small
7	7	10	small
8	8	11	small
10	10	13	small
11	11	14	small
12	12	16	small
14	14.2	18.2	large
16	16	20	large
18	18.4	22.1	large
20	20.3	24	large
21	21.2	24	large
23	23.2	26	large
25	25.4	28.1	large
27	27.3	30	large
29	29	32	large

3.4 Modeling methodology

We have developed a model of the Discover that combines all relevant physics. The model was used both for the study into the spatial distribution of the heating process and for the study into the parametric sensitivity of the heating process. For the former study, the model includes electromagnetics, conductive and convective heat transfer, and fluid flow; for the latter study, only the electromagnetics is considered. This section describes the complete multiphysics model, in Section 3.6.3 the simplifications of the electromagnetics-only model are discussed. The modeling environment is Comsol Multiphysics 3.5 with the RF-module and the Heat Transfer module [70]. Regarding the electromagnetics, the model simulates both the forward and backward interaction between the applicator section of the circuit and the magnetron microwave source. This was done via microwave network analysis. The approach is motivated by the desire to predict energy flow in the system, which can only be done if all the mutual interactions between the elements in the microwave circuit are accounted for. Figure 3.4 presents the diagram of interconnected variables of the simulation. It comprises of: 1) a lumped model for the magnetron characteristics, 2) computational electromagnetics for the microwave field in the applicator section, 3) conductive and convective heat transfer in the water filled vial, and 4) computational fluid dynamics to account for the convective fluid motion in the vial. This section further details the modeling aspects of the simulation, the simulation results are discussed in Sections 3.5.3 and 3.6.3.

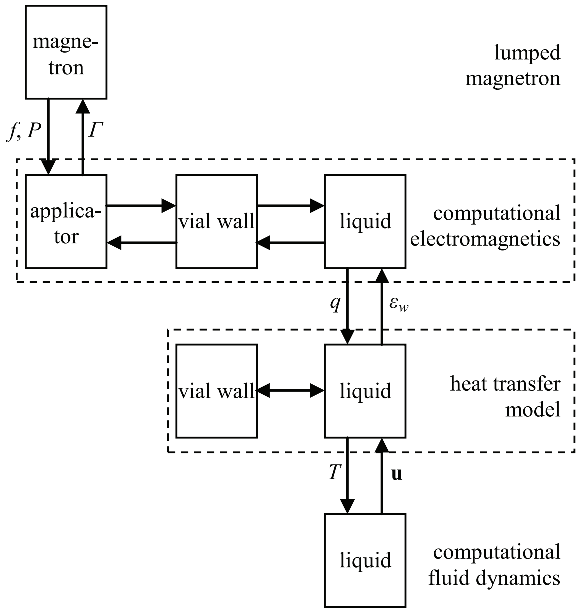

Figure 3.4. Diagram of the interconnecting model variables of the multiphysics simulation that combines electromagnetics, heat transfer and fluid mechanics.

3.4.1 Magnetron model

The rectangular block at the top of Figure 3.4 represents the lumped magnetron. There is a complex interaction between the applicator section of the microwave circuit and the magnetron microwave source. The magnetron generates microwave energy, which is coupled into the applicator section. There it is partially absorbed in the load that is placed in it, and partially reflected by the applicator back towards the magnetron. This reflected energy is then again partially absorbed by the magnetron and partially reflected back into the applicator. As such, a complex system of generated, reflected and absorbed microwave energy is formed. To determine the net power transfer into the applicator – power that is eventually absorbed in the load – a lumped magnetron model is used. This model is represented by a function that has the reflection coefficient of the applicator circuit (Γ) as its input and the net power transfer (S) and the operating frequency (f) as its output,

$$[S,f] = f_M(\Gamma) \tag{3.3}$$

A reflection coefficient [69] is a complex valued variable; it is the complex ratio of the electric field of the reflected electromagnetic wave to the electric field of the forward electromagnetic wave. The absolute value of the reflection coefficient is the ratio of the electric field amplitudes of the reflected and the forward waves respectively; and the argument of the reflection coefficient represents the phase delay, relative to the electric field component, that the field incurred over its path inside the electromagnetic system under consideration. The considered system only involves the reflection coefficient for the TE_{10} propagation mode. Propagation modes are ways in which microwaves can travel through waveguide structures and for each waveguide there exist an integer number of propagation modes. The system is operated below the cut-off frequencies of the higher order propagation modes of the waveguide, so only TE_{10} matters [69].

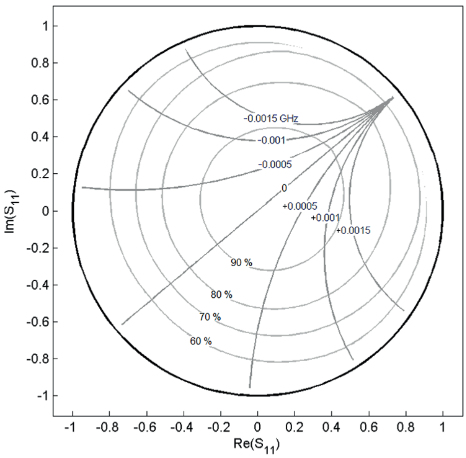

Figure 3.5. Rieke diagram of the idealized magnetron model fitted to experimental data from the specifications of the 2M218 magnetron [91].

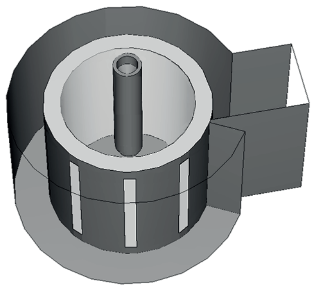

Figure 3.6. Cutaway view of the geometry of the applicator section that was simulated.

If the isolines of the function in Equation 3.3 are plotted on the unit disk of reflection coefficients, a Rieke diagram is formed. Figure 3.5 presents the Rieke diagram of the function in Equation 3.3 as it was used in the model. It is a fit of an idealized magnetron model that was based on a simplified equivalent circuit [65]. The magnetron model was fitted to an experimentally obtained Rieke diagram [91] that was found in literature on the 2M218 magnetron tube that is used in the Discover. A 220° clockwise rotation was added to the magnetron model to account for a shift in reference plane in the applicator model. Based upon the measurements of the electric power drawn from the socket, as was mentioned earlier, the maximum power of the magnetron model is scaled back to 675 W.

3.4.2 Computational electromagnetics of the applicator section

Figure 3.6 displays the geometry of the applicator section that was simulated. The electromagnetic model of the applicator section – second row in Figure 3.4 – solves for the microwave field in the applicator waveguide, in the vial, and in the liquid contained in the vial. The Radio Frequency module of Comsol Multiphysics 3.5 [70] is used to calculate the microwave field. It solves the Helmholtz representation of Maxwell's electromagnetic field equations to determine the time harmonic microwave field,

$$\nabla^2\mathbf{E} + \varepsilon_r\left(\frac{2\pi f}{c_0}\right)^2\mathbf{E} = \mathbf{0} \tag{3.4}$$

where **E** is the complex electric field vector of the time-harmonic oscillating microwave field, f is the frequency of oscillation, ε_r the relative permittivity of the dielectric media consisting of a real part ε' and an imaginary part ε'' ($\varepsilon_r = \varepsilon' - i\varepsilon''$), and c_0 the speed of light in vacuum. The imaginary part of the relative permittivity, ε'', is the dielectric loss factor, which determines the electromagnetic dissipation in a material.

The medium parameters relevant in the electromagnetics model are the relative permittivities of the materials present in the microwave circuit. PTFE and borosilicate glass are assumed not to absorb microwave energy; so, for PFTE, $\varepsilon_r = 2.06 - 0i$ [65] and for the borosilicate glass of the vials, $\varepsilon_r = 4.6 - 0i$ at 1 MHz [92]. Because ε_r of borosilicate glass does not vary much over the frequency range at the relevant temperatures [65] this value was assumed to be appropriate at 2.45 GHz as well. In contrast, the permittivity of water does vary significantly over the relevant temperature range. Table 3.3 presents the ε_r values of water [74] used in the model over the temperature range 20 – 100°C.

Table 3.3. Complex relative permittivity of water for a range of temperatures at 2.45 GHz [74].

Temperature [°C]	Complex relative permittivity [-]
20	78.0 – 10.5i
30	75.0 – 8.6i
40	72.0 – 6.7i
50	69.0 – 5.1i
60	66.2 – 3.85i
70	63.9 – 3.3i
80	62.7 – 3.1i
90	62.3 – 3.0i
100	62.0 – 2.9i

The heat generated in the water is determined via,

$$q = \pi f \varepsilon_0 \varepsilon'' \mathbf{E} \cdot \mathbf{E}^* \tag{3.5}$$

in which $\varepsilon_0 \approx 8.8542 \cdot 10^{-12}$ F/m is the electric permittivity of vacuum and $\mathbf{E}^*$ is the complex conjugate of the electric field vector.

As shown in Figure 3.4, the electromagnetic model has got the net power transfer (S), the operating frequency (f) and the temperature dependent permittivity of water (ε_w) as inputs and the generated heat (q) and the reflection coefficient of the applicator (Γ) as outputs. The reflection coefficient of the microwave circuit at a given distribution of the temperature dependent relative permittivity of the water volume is a function of the operating frequency,

$$\Gamma = f_A(f) \tag{3.6}$$

This equation in combination with Equation 3.3 determines the interaction between the magnetron and the applicator sections of the microwave circuit. The procedure is further described in Section 3.4.5.

3.4.3 Heat transfer model

Heat transfer is modeled in the water contained in the vial (conductive and convective) and in the vial wall along the wetted length plus an additional non-wetted length (conductive). Over the relevant temperature range, water has little thermal expansion, so the total water volume is assumed constant. No heat transfer to the surroundings is included, since the vial is thermally insulated and does not release much heat to the surroundings over the simulated time scale. Figure 3.7 presents an axisymmetric cross section of the simulated domain of the vial with the imposed boundary conditions indicated.

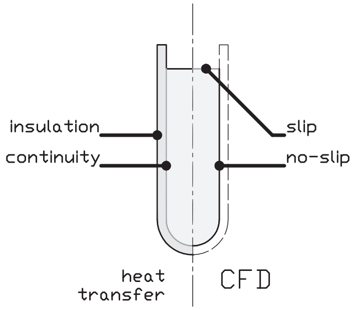

Figure 3.7. Axisymmetric cross section of the simulated domain of the vial with the imposed boundary conditions indicated for heat transfer and fluid dynamics.

3

The heat transfer model – third row in Figure 3.4 – solves for convection and conduction in the load using Comsol's Heat Transfer module [70] according to,

$$\rho C_p \partial_t T + \nabla\cdot(-k\nabla T) = q - \rho C_p \mathbf{u}\cdot\nabla T \tag{3.7}$$

The first term on the left hand side is the accumulation rate of heat and the second term is the conductive contribution to heat transfer. On the right hand side, the first term is the heat generation and the second term is the convective contribution to heat transfer. The symbol ρ denotes the medium density; C_p is the specific heat capacity; T is the temperature; k is the thermal conductivity; q is the dielectric heat generation; and $\mathbf{u}$ is the flow velocity vector, which is relevant only to the domain of the liquid contained in the vial. Table 3.4 lists the medium properties used herein. The heat transfer model has the electromagnetic energy loss (q) and the fluid velocity field ($\mathbf{u}$) as its input variables, and the water permittivity (ε_w) and temperature (T) as its output variables (see Figure 3.4).

Table 3.4. Material properties used in the simulation [65,74,92-95].

Air				
	ε_r	complex relative permittivity	$1.0 - 0i$	-
PTFE ring				
	ε_r	complex relative permittivity	$2.06 - 0i$	-
Vial, borosilicate glass				
	ε_r	complex relative permittivity	4.6	-
	ρ	density	2230	kg/m^3
	k	thermal conductivity	1.2	W/m·K
	C_p	specific heat capacity	840	J/kg·K
Water				
	ε_r	complex relative permittivity,	see Table 3.3	
	ρ	density	1000	kg/m^3
	$\rho_w(T)$	temperature dependent density,	see Table 3.5	
	k	thermal conductivity	0.58	W/m·K
	C_p	specific heat capacity	4180	J/kg·K
	η	dynamic viscosity,	see Table 3.6	

3.4.4 Fluid dynamics model

The computational fluid dynamics model – fourth row in Figure 3.4 – employs the incompressible Navier-Stokes feature of Comsol Multiphysics 3.5 [70] to solve for the momentum balance equation,

$$\rho[\partial_t \mathbf{u} + \mathbf{u} \cdot \nabla \mathbf{u}] - \eta \nabla \cdot [\nabla \mathbf{u} + (\nabla \mathbf{u})^T] + \nabla p = [0 \;\; 0 \;\; F_z]^T \tag{3.8}$$

and for the continuity equation for incompressible fluids,

$$\nabla \cdot \mathbf{u} = \mathbf{0} \tag{3.9}$$

In Equations 3.8 and 3.9, **u** is the flow velocity vector, η is the dynamic viscosity, and ρ is the fluid density. The first term in the momentum balance equation is due to inertia, the second term are the viscous forces and the third term is the pressure gradient ∇p. On the right hand side is the gravity field F_z acting on the liquid. In order to drive free convection in the fluid dynamics model, there must be a variation on gravitational pull on the liquid. Therefore the density of water was introduced a second time into the model, now as $\rho_w(T)$, but this time only to account for the gravitational volume force field (F_z) over the volume,

$$F_z = -9.81\rho_w(T) \tag{3.10}$$

Table 3.5 lists ρ_w for water at different temperatures. Table 3.6 lists the dynamic viscosity of water over the temperature range. A no-slip boundary condition is imposed on the contact surface with the vial wall and a slip boundary condition is imposed on the liquid surface level (Figure 3.7). The temperature (T) and the fluid velocity field (**u**) are the input and output variables to and from the fluid dynamics model, respectively (Figure 3.4).

Table 3.5. Temperature dependent density of water [93].

Temperature [°C]	Density [kg/m³]
0	999.8
4	1000
20	998.3
40	992.3
60	983
80	972
100	958

Table 3.6. Temperature dependent viscosity of water [94].

Temperature [°C]	Viscosity [Pa·s]
0	$1.787 \cdot 10^{-3}$
10	$1.307 \cdot 10^{-3}$
20	$1.002 \cdot 10^{-3}$
40	$0.653 \cdot 10^{-3}$
60	$0.467 \cdot 10^{-3}$
80	$0.355 \cdot 10^{-3}$
100	$0.282 \cdot 10^{-3}$

3.4.5 Solver specifications, operating point and discretization

This problem has very stiff dynamics; the electromagnetics work on time scales of 10^{-9} seconds, which is considerably faster than the 0.1 to 10 seconds time scale of convection and conduction. The microwave field is therefore modeled as a stationary field that is periodically updated, while heat transfer and fluid dynamics are solved as a dynamically coupled model. A procedure was scripted in MATLAB [76] to determine the operating point of the interaction between applicator and magnetron. Figure 3.8 presents a flow chart of this procedure. For a set of frequencies spanning 30 MHz, the applicator model (Eq. 3.6) calculates the corresponding set of reflection coefficients,

$$\{\Gamma_1,\ldots,\Gamma_N\} = f_A(\{f_{1.1},\ldots,f_{1.N}\}) \tag{3.11}$$

Subsequently, a corresponding set of net microwave power transfers and a secondary set of frequencies is calculated with the magnetron model (Eq. 3.3),

$$[\{f_{2.1},\ldots,f_{2.N}\},(\{S_1,\ldots,S_N\}] = f_M(\{\Gamma_1,\ldots,\Gamma_N\}) \tag{3.12}$$

The operating frequency is found by interpolating the condition where frequencies of the applicator model and magnetron model match ($f_1 = f_2$). Based on this frequency, the net microwave power transfer in the operating point is calculated using the relations above. Since it is assumed that in the applicator section there is no electromagnetic dissipation apart from the dielectric loss in the water volume, the total heat generation in the vial equates corresponds to the net power transfer between magnetron and applicator. The heating rate distribution, q, in the water volume is first calculated for a preliminary power input and is subsequently scaled to match the total heat generation that Is obtained by the procedure in Figure 3.8.

The relevant discretization parameters in this model are: the spectral resolution of the aforementioned set of frequencies, the mesh refinement of the electromagnetics model, the refresh rate of the microwave field in the dynamic simulation, the maximum step size of the dynamic simulation, and the mesh refinement of the combined heat transfer and fluid dynamics model. The mesh refinement with $1.33 \cdot 10^6$ elements is chosen such that the converged solution fits into the 24 GB RAM available. Further refinement is not possible due to memory limitations with the computer used. Nevertheless, in order to have a rough estimate of how further mesh refinement may affect the solution presented herein, simulations were run with a simpler model and progressive mesh refinement up to the point that the solution is no longer affected by the mesh size (mesh independent solution). This simplified model differs from the model presented in this work in that the electromagnetics component is excluded and a representative heating rate distribution is imposed. It was found that the solution with the number of elements used in the full model is within 10% of the mesh independent solution.

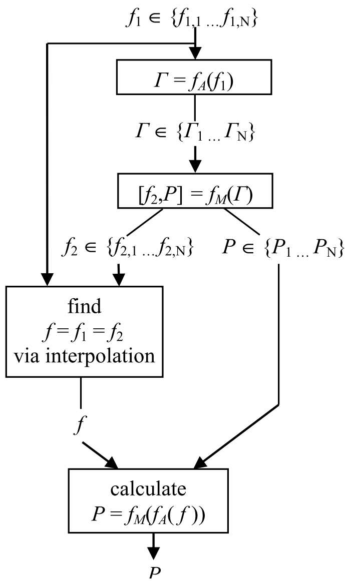

Figure 3.8. Calculation of operating point in terms of reflection coefficient, frequency and transmitted power. The function $f_A(f_1)$ indicates the applicator model and the function $f_M(\Gamma)$ indicates the magnetron model.

3.5 Distribution in space and time of the resonant microwave field

This section investigates the heating rate distribution induced by the resonant microwave field in the Discover. It discusses experimental methodology, the experimental results and the simulation data obtained with the model described in the previous section. Out of the set of fifteen vials, three vials were selected for the investigations in this section, being the vials with the 10 mm, 12 mm and 20 mm inner diameter.

3.5.1 Experimental methodology

Ideally one would place as many sensors as possible inside a load to assess its temperature field when it is exposed to microwave fields. As this is not a practical solution, an alternative approach is to combine measurement techniques. The two techniques that are used in this study are multiple fiber optic temperature sensors and thermally sensitive dyes.

The temperature sensors employed are Neoptix T1 sensors [96] connected to a Neoptix Reflex signal conditioner [97]. The sensors tips are not fitted with their standard PTFE jacket, which leaves a minimally sized sensor tip with an approximately 0.6 mm diameter. Because the size of the measurement volume is small, a good spatial resolution is obtained and, additionally, internal dynamic lag and electromagnetic scattering by the sensor are minimized. The response time of the sensors is 35 ms, but the dynamic limitation on measurement that remains is the maximum sample rate of one sample per second.

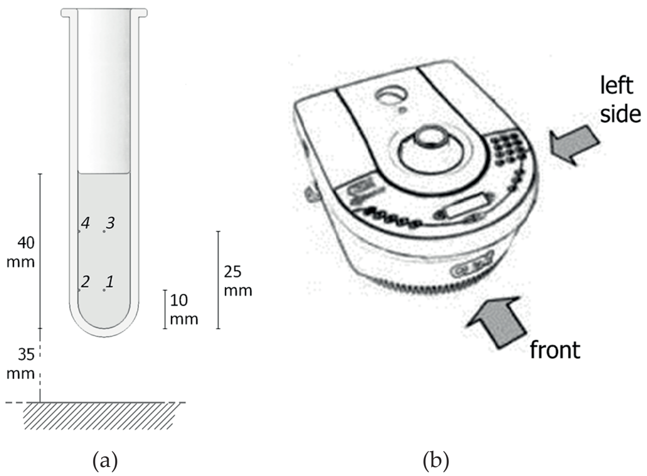

Figure 3.9. Description of measurement positions and perspectival orientations. The figure on the left (a) defines the positions of the numbered sensor tips in the vials in a front view orientation as defined by the figure on the right (b). Four sensors are placed in the following positions: 10 mm above the vial bottom on the centerline of the vial; 25 mm above the vial bottom on the centerline of the vial; 10 mm above the vial bottom against the right wall of the vial (from the perspective of the device); and 25 mm above the vial bottom against the right wall of the vial. Figure 3.9b defines the front view and left side view considered in this study, relative to the device. The arrows indicate the faces the observer is looking at.

Four sensors were used, numbered 1 to 4, and they were positioned according to Figure 3.9. The sensors were placed with a minimum of supporting structure. Although the accuracy of positioning is approximately one millimeter due to their minimal support, it reduces the effect the support has on the microwave field. The vials were positioned in the cylindrical cavity according to Figure 3.1c and exposed to the maximum microwave power the Discover can produce. Starting at an ambient temperature of around 20°C, the vials were heated for a duration that would cause them to remain just below boiling. It was found that the rate of temperature increase is highly dependent on the dimensions of the vials. For the 10 mm inner diameter vial a duration of exposure of 8 seconds was set; in the 12 mm vial the rate of temperature increase was much higher and it could be exposed for only 2 seconds before it would boil; the duration of exposure set for the 20 mm vial is 17 seconds. No stirring is applied; free convection governs fluid motion.

The thermally sensitive dyes used in this study are strips of thermal fax paper. It consists of thermally sensitive ink on a paper substrate (56 μm thickness). In preparatory experiments it was found that this ink darkens irreversibly if the temperature exceeds a threshold of roughly 67°C. This method has limitations; it can only indicate the region where a temperature of 67°C has been exceeded at some point in time. Nevertheless, it does allow evaluation of the continuous shape of the temperature field in the entire plane in which the thermal paper is placed; this is impossible when there is only a limited discrete set of measurement points available, as is the case with fiber optic sensors.

Paper strips were cut such that they fit tightly in the vials. The ink dissolves quickly when exposed to moisture, so the strips were covered by a combination of transparent adhesive tape and transparent plastic film. The total thickness of the packaged strips was 0.2 mm. One strip was used in each experiment. A strip was placed in the middle of the vial in either the front view orientation or the left side view orientation, with the ink facing the respective arrows in Figure 3.9. All experiments were conducted at the maximum microwave power the device can supply. To determine the development of temperature in time, the experiments were conducted in series with varying duration of microwave exposure. The exposure times were varied by one or two seconds; the shortest variation available in the time settings of the device is one second. The strips were extracted from the vial as soon as the exposure ended. Subsequently, the temperature was homogenized by manual stirring and measured with a fiber optic temperature sensor.

3.5.2 Experimental results

From the results obtained both with the fiber optic sensors (Figure 3.10) and with the thermal paper (Figure 3.11) it is clear that the samples are heated non-uniformly. Measurements from the lower placed sensors consistently show lower readings than those placed higher. Moreover, the thermal paper results show a pattern of several dark spots that grow with increasing duration of exposure. These dark spots coincide with regions of high temperature measured by the sensors. Importantly, both measurement methods indicate that for the cases presented here, the zones in the bottom of the vials remain relatively cold for the duration of the experiments. Note that the temperature rise would not have been registered by a probe dropped onto the bottom of the vial nor by the built-in pyrometer of the Discover; this demonstrates the risk of missing the dominant temperature trends in microwave heated systems by unfortunate sensor placement.

From the transients measured with the probes it is found that the heating rate not only varies in space, but also in time. Figure 3.10a shows a decelerating temperature rise (concave trend) for the 10 mm vial. On the contrary, Figure 3.10c shows a slightly convex trend for the 20 mm diameter vial. Thus, depending on the size of the load, the system responds differently to the changes in material properties that were induced by rising temperatures.

Power transmission towards the load varies between cases as well: for the 10 mm vial (Figure 3.10a) multiplication of the temperature difference with an estimated heat capacity yields a transmission of around 100 W; for the 12 mm vial (Figure 3.10b), it results in a transmission of around 450 W; and for the 20 mm vial (Figure 3.10c), it is around 200 W. As was remarked earlier, the system is rated at a maximum microwave power output of 300 W by the manufacturer.

Aside from non-uniform transient heating, indications are present in the experimental results of a high sensitivity to perturbation. Figure 3.11b presents results of repeated experiments for the front and side view orientations of the fax paper strip placed in the 12 mm vial with durations of exposure of 1 and 2 seconds. For each pair of experimental conditions in terms of strip orientation and duration of exposure, the experiment was repeated four times. Even though the respective series of experiments had the same initial conditions, there is a striking variation in darkening of the strips and in the homogenized end temperatures. This apparently stochastic behavior is likely caused by subtle imperceptible variations in, for example, water volume and temperature, positioning of vial and paper strip, and magnetron temperature. As was reported above, the microwave energy transfer is high for this particular vial, which is a sign that in these specific conditions the system is operating at a resonance peak in the microwave energy transfer. Peaks in the relations between variables of resonant systems are characteristically narrow; a slight variation can thus have a relatively large effect. The strong amplification of imperceptible variations that occurs when this specific vial is heated would be an expectable outcome of this mechanism.

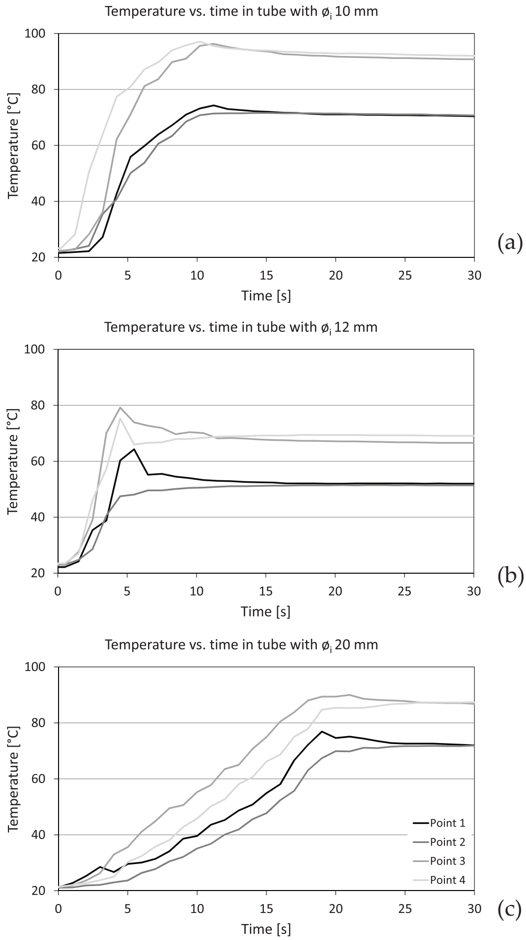

Figure 3.10. Temperature transients measured by fiber optic sensors in the vials: (a) the 10 mm inner diameter vial; (b) the 12 mm inner diameter vial; and (c) the 20 mm inner diameter vial. The sensors were placed as shown in Figure 3.9. Microwave exposure lasted 8 s for the 10 mm vial, 2 s for the 12 mm vial, and 17 s for the 20 mm vial. These are the maximum durations of exposure for the respective vials for which the water contained in them does not boil. The trends vary significantly between the vials. The temperature transients in the 10 mm vial have a concave trend; in the 12 mm vial there is a very high rate of temperature increase and three out of for transients have a significant overshoot before they reach a quasi-steady state; finally, the temperature transients of the 20 mm vial have a slightly convex trend. During and shortly after microwave exposure, temperature changes quickly, but only seconds after exposure ends, the temperature distribution reaches a quasi-steady state in which heat transfer is governed by slow heat loss to the surroundings. After the 30 s interval in these graphs, temperatures fall in 20 – 50 minutes to the temperature of the surroundings.

The results for the 20 mm inner diameter vial indicate a high degree of sensitivity to perturbations of the heating process as well. Most obvious is the fact that the thermal paper strips placed in the side view orientation are considerably darker that the respective strips in the front view orientation (Figure 3.11c). This is reflected by the homogenized temperatures as well, which are initially higher for the experiments with the strips oriented in the side view. Aside from this, the shape of the heating patterns on the strip differs strongly between the two orientations. Furthermore, the times at which the sensors reach 67°C (Figure 3.10c) are different from the times at which the onset of darkening of the thermal paper is observed in the corresponding positions. In position 1, for example, the thermal paper in side view orientation has clearly exceeded the discoloration temperature of 67°C after 6 seconds of exposure, whereas the sensor in position 1 reaches this temperature only after 17 seconds at the same power setting. The time scale on which this difference occurs is much larger than what could be expected on the basis of a difference in the response times of the respective sensing agents. In addition to this, would the response times play a role in the dynamics of the system, then one would expect slower dynamics of the thermal paper compared to the sensor, as the former is packaged in several layers of plastic film and adhesive tape. It can be concluded therefore that, although the thermal paper strip is thin, it acts as a substantial electromagnetic scatterer and strongly affects heat generation in this specific vial, again a sign of a high sensitivity to perturbation.

Summarizing, the heating process in the resonant microwave field provided by the Discover was found to behave in a highly case specific manner. The heating patterns presented in Figure 3.11 differ considerably with the diameters of the vials, which is also reflected in the transients presented in Figure 3.10. Additionally, the sensitivity to perturbation also differs between the vials. More specifically, while for the 20 mm vial the presence and orientation of the fax paper strip notably affects heating, for the 12 mm vial this does not occur. Rather, the effect of other imperceptible variations is strongly amplified. Finally, for the 10 mm vial, neither type of sensitivity was observed. Collectively, heating a load as simple as a water-filled vial in a resonant microwave field proves to be quite a complex process for which it is difficult to make detailed predictions.

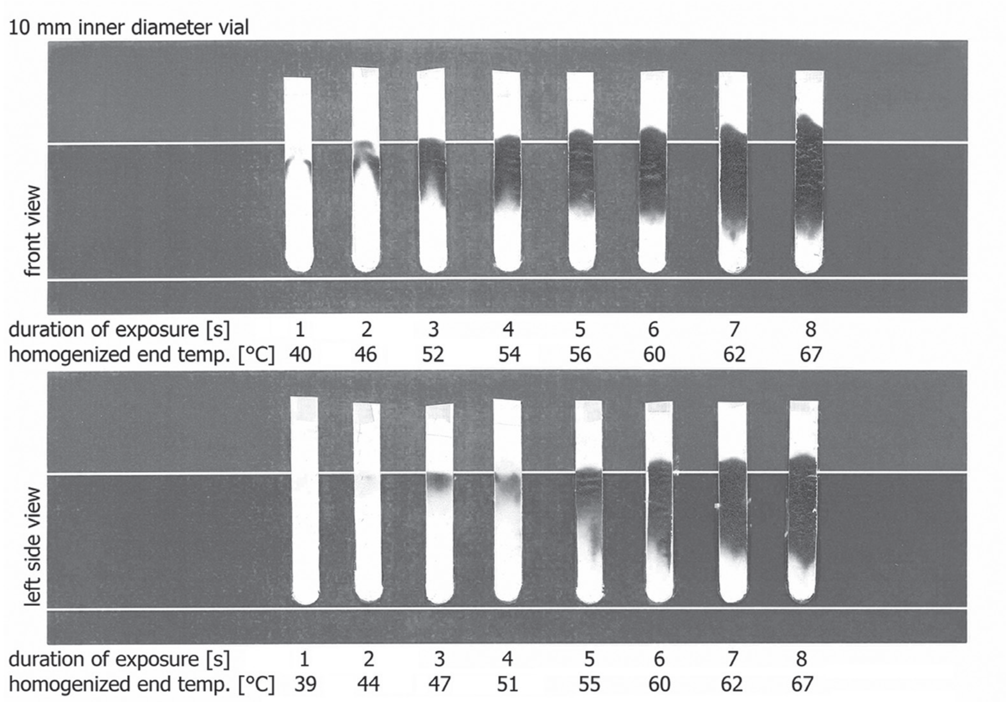

(a)

Figure 3.11. Discoloration of strips of thermal fax paper placed in a vial containing water to a level of 40 mm. These are results for (a) the 10 mm inner diameter vial, (b) the 12 mm inner diameter vial, and (c) the 20 mm inner diameter vial. During the experiments, the vials ▷

3

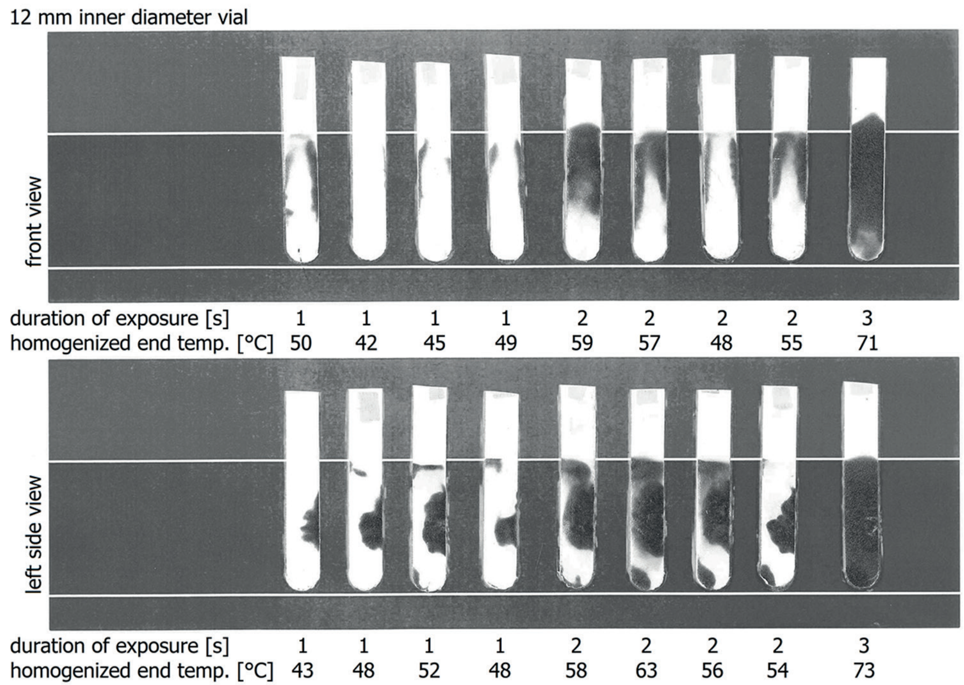

(b)

Figure 3.11. *(continued)* were exposed to the maximum microwave power the Discover can supply. The strips are oriented in front and side view (top and bottom rows, respectively) with the inked side of the strip facing the respective arrows in Figure 3.9. The ▷

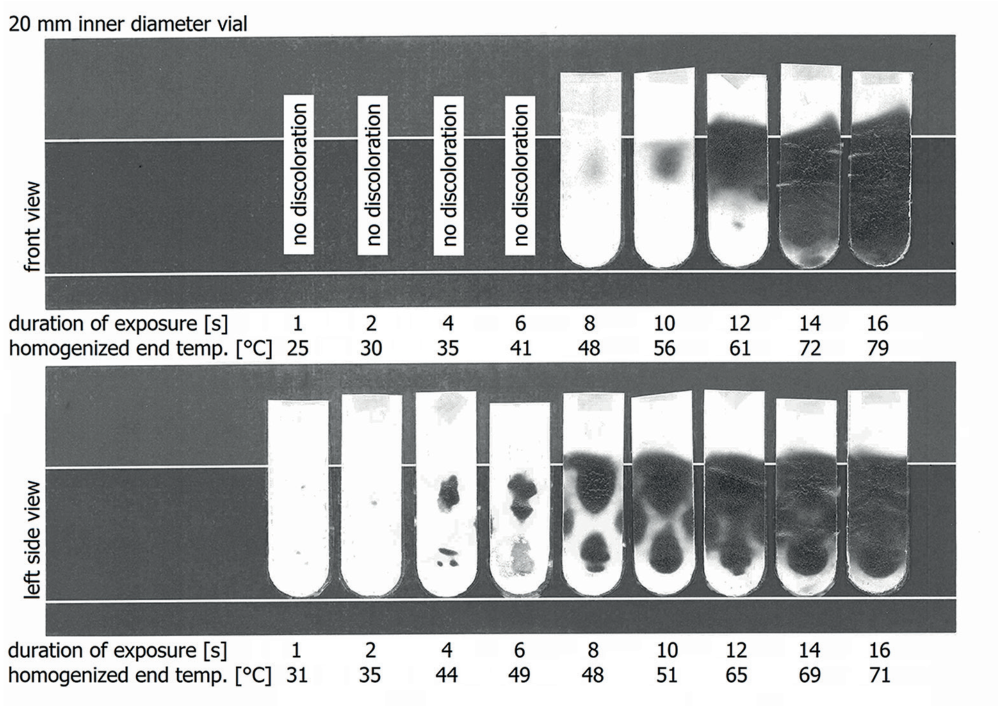

(c)

Figure 3.11. *(continued)* upper white lines separating the gray planes indicate the height of water level. Note that each strip results from a separate experiment. Underneath each figure, the duration of microwave exposure and the homogenized final temperature of the water after exposure are indicated.

3.5.3 Simulation results

Since it has the shortest operating time of the cases described in the previous section, only the case of the 12 mm vial was chosen for simulation to limit the time required for simulation. The simulation lasted a little more than 5 days, which would roughly extrapolate to 20 days in case of the 10 mm vial and six weeks in case of the 20 mm vial. Two seconds of microwave exposure (at full power) of the 12 mm inner diameter vial was simulated, at a starting temperature of 20°C, followed by 8 seconds of conductive and convective heat transfer. The slice plots for volumetric heat generation and temperature after one and two seconds of exposure are presented in Figure 3.12.

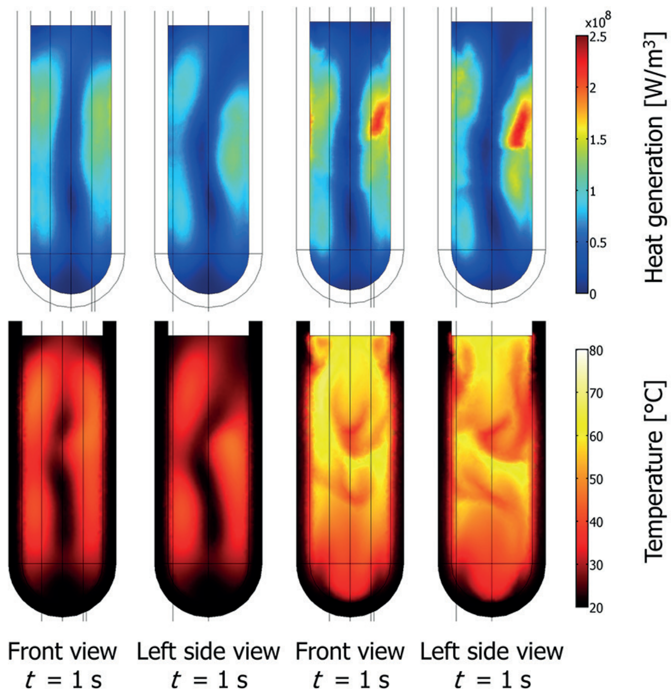

Figure 3.12. Simulation results for heat generation (top) and temperature (bottom), in front and left side view, after one and two seconds of exposure of the 12 mm inner diameter vial to the microwave field. These slice plots are centered in the vial and oriented according to the views specified in Figure 3.9.

The pattern found experimentally with the thermal paper qualitatively corresponds to the simulation results. In the front view, there are two hot zones against the vial wall that are more pronounced in the top half of the vial than in the bottom half. The side view has a dominant hot zone against the back wall of the vial, while there are two relatively smaller hot zones in the top and bottom of the vial against the front wall. This pattern is present in all results for heating rate distribution and in the results for the temperature distribution after one second of exposure. The temperature distribution after two seconds of exposure does not exhibit the experimentally found pattern. This difference is likely caused by the presence of the strip of thermal paper in the experiments, which obstructs the convective flow patterns that redistribute temperature in the simulation.

While the heating rate and temperature distribution patterns found by the thermal paper qualitatively coincide with the simulation results, the quantitative temperature rise is underestimated by the model. The 67°C temperature threshold is not reached in the simulation at time and location where it has in the experiment; the temperature rise is underestimated by about a third by the model. Moreover, the microwave power transfer is underestimated in the model. Figure 3.13 presents the simulated transient of microwave power transfer. It averages around 320 W, which is about 70% of the average power found experimentally.

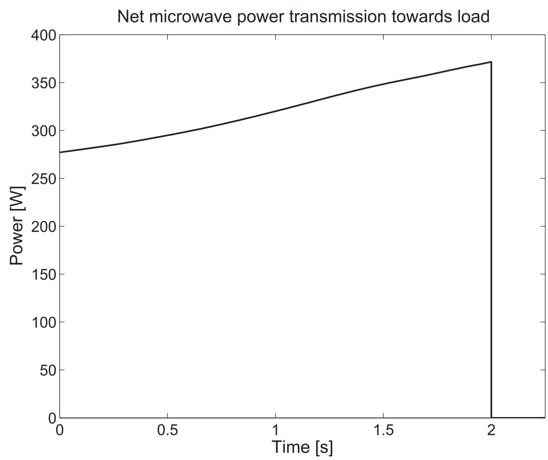

Figure 3.13. Net microwave power transfer to the load during the 2 second microwave exposure time.

The discrepancies likely originate mostly from the magnetron model, although the geometrical inaccuracies probably have affected the results as well. The magnetron model we use is an idealized fit to data [91] measured during operating conditions of the magnetron tube that are similar, but not the same as those that occur in the Discover. In addition, despite the fact that this literature data spans a large portion of the unit disk of reflection coefficients, measurement data near the edge of the unit disk is absent. In this region the model is an interpolation that makes the transferred power go to zero at the edge of the unit disk. Although it is possible to improve the magnetron model by tuning it to fit our experimental results, the multiphysics simulation was intended to be based upon first principles. Alternatively, one could start out with better data for magnetron behavior. This, unfortunately, was unavailable to us. The purpose of the simulation was to gain qualitative understanding on heating induced by resonant microwave fields and to demonstrate a methodology to simulate the interaction the microwave circuit has with its microwave source. The model therefore suffices for this purpose.

Note that, as found experimentally, the net power transfer is not a stationary variable. It varies in time as do the simulation results for heat generation. The changes in medium properties caused by temperature rise are coupled back via the microwave field towards the magnetron and influence its operation. Further transients are shown by Figure 3.14, which displays temperature profiles versus time for the four points defined in Figure 3.9. As mentioned above, the temperature rise is ~2/3 of what was found experimentally, which is a reduction by the same ratio as the simulated power transfer compared to the experimental one. In accordance with the experiments, temperatures in the two lower positions are below those in the higher positions; also, the temperatures settle to a quasi-steady state as they do in the experiments. The simulated transients are shaped differently from those found in the experiments, which can have multiple causes. In the simulation, the convective flows are not impeded by the sensors themselves, nor are the measurements affected by internal dynamics or the non-zero volume of the sensors. Furthermore, the experimental measurements suffer from a limited sample rate, which is not relevant to the simulation. Indeed the simulations show fast convective fluctuations of temperature, which would be unobserved in the experimental sample interval.

Temperature inhomogeneity that occurs during microwave exposure and shortly afterwards is demonstrated again by Figure 3.15, which shows a temperature histogram at t = 2.0 seconds, the moment at which microwave exposure ends. The histogram displays a wide spread in temperature. Even though there is convective fluid circulation during and just after microwave exposure, at t = 10 seconds – which is 8 seconds after microwave exposure ends – there still is a considerable quasi-stable temperature gradient in the axial direction. At t = 10 seconds the bottom has only reached 23°C, while the upper fluid level is quasi-steady at 57°C. In accordance with the experimental results, the temperature increase due to microwave heating would be largely unobserved over this time span by either a probe dropped in on the bottom of the vial or by the built-in pyrometer.

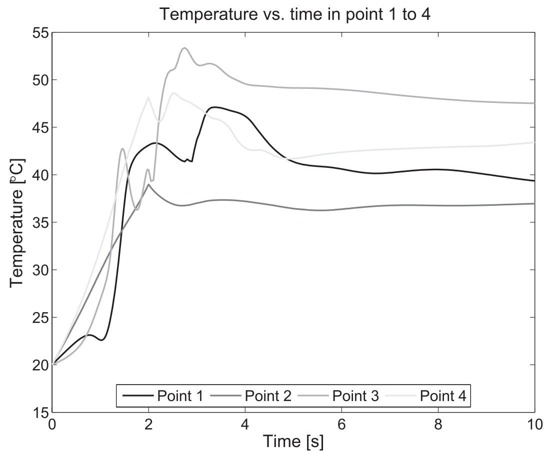

Figure 3.14. Temperature transients for point 1 to 4 (refer to Figure 3.9).

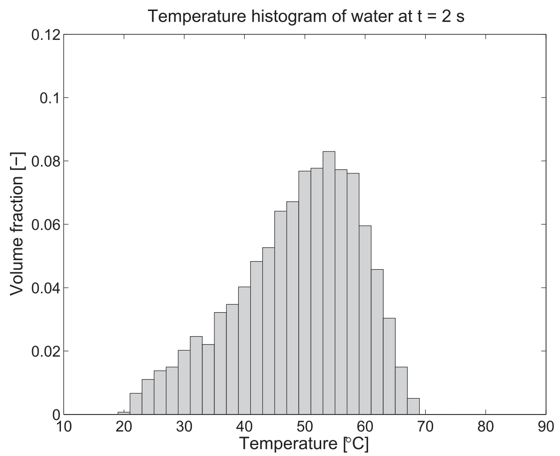

Figure 3.15. Temperature histogram for the fluid at t = 2.0 s.

When the simulation ends, at t = 10.0 s, the convective flows have stopped and they will no longer be induced because the downwards gravitational pull decreases with height. The system thus reaches a quasi-steady state that is governed by slow conductive temperature homogenization. Heat transfer to the surroundings was not modeled, because it has no relevance for the time scales considered here. Would it be included though, temperature would drop slowly until it eventually reaches equilibrium with the surroundings.

3

3.6 Parametric sensitivity of the overall heating rate

In this section the parametric sensitivity of the overall heating process by means of the resonant field in the CEM Discover is investigated. The following aspects are discussed: the experimental methodology, the experimental results and the simulation results. The complete set of fifteen vials is considered in this section.

3.6.1 Experimental methodology

The investigation of the overall heating process in the vial is complicated by the fact that heat generation and temperature under microwave heating typically are not homogeneously distributed in space, stirring is therefore required. Although the Discover facilitates magnetic stirrer bars, the bars do not fit into the smallest vials. Additionally, bars affect the microwave field, which complicates the analysis. An alternative approach towards temperature homogenization and measurement is employed. Figure 3.16 presents this procedure. It consists of applying consecutive cycles of 1) temperature homogenization by stirring, 2) temperature measurement, and 3) microwave heating. First, the temperature is homogenized by manual stirring with a small polystyrene rod for at least 5 seconds to bring the vial wall in thermal equilibrium with the water. Simulation in Comsol Multiphysics 3.5 [70] revealed that the heat accumulated in the wall approaches this equilibrium with a margin of 10% in 5 seconds after a step-wise temperature increase of the water. The heat accumulating in the insulation material is negligible (< 5%). In the next step, the temperature is measured with a small uncladded fiberoptic temperature probe (Neoptix T1 [96]), which is followed by a short pulse of microwave heating at the maximum power of the device (specified to be 300 W). This procedure of stirring, measuring and heating is repeated in consecutive cycles until boiling occurs. In most cases, the pulse is applied over the shortest time interval that is available in the settings, which is one second. For some vials the boiling point is reached more rapidly than for others. If needed, the procedure was repeated several times to generate sufficient data.

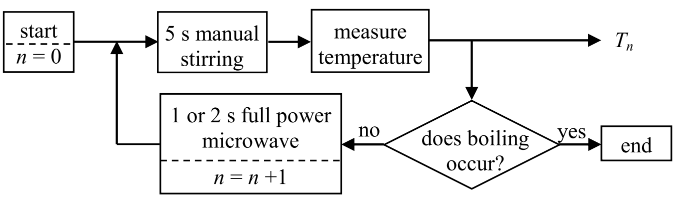

Figure 3.16. Experimental procedure for temperature measurement.

3.6.2 Experimental results

Figure 3.17 illustrates the progression of heat generation by microwave fields in the water contained in the vials. More specifically, the figure presents the results of two different experiments that are represented by black and gray colored curves, respectively. These experiments are conducted with the 21 mm inner diameter vial and the same initial temperature of a little over 20°C.

Figure 3.17a shows the homogenized temperature versus the number of past heating cycles. It shows that for both the black and the gray experiment temperature increases monotonically with the number of heating cycles. It was found that the black and the gray curves initially follow a similar path, but after ten heating cycles they split. Eventually, the gray curve reaches the boiling point sooner even though the conditions of both experiments are the same in practical terms. Additionally, upon closer inspection, the seemingly similar initial trajectories of the curves in Figure 3.17a are not exactly the same.

This is more evident in Figure 3.17b, which presents the temperature gains during the consecutive heating cycles of both experiments. Both the black and the gray experiment show an irregular and fluctuating trend in the temperature gains. Moreover, the black and the gray trend in Figure 3.17b follow two completely different paths.

Similar to the results from Section 3.5, Figure 3.17 shows that this heating process has complex and unpredictable characteristics. The data obtained with the complete set of fifteen vials is processed to further understand these characteristics. First, the heat generation during the heating pulses is determined calorimetrically by multiplying the estimated heat capacity of the vial and the water ($C_{vial} + C_{water}$) with the temperature gain ($T_n - T_{n-1}$) followed by division with the duration of microwave exposure ($t_{microwave}$),

$$H_n = \frac{(C_{vial}+C_{water})(T_n-T_{n-1})}{T_{microwave}} \tag{3.13}$$

Then the average temperature during the heating pulses is calculated,

$$T_{av,n} = \frac{(T_n+T_{n-1})}{2} \tag{3.14}$$

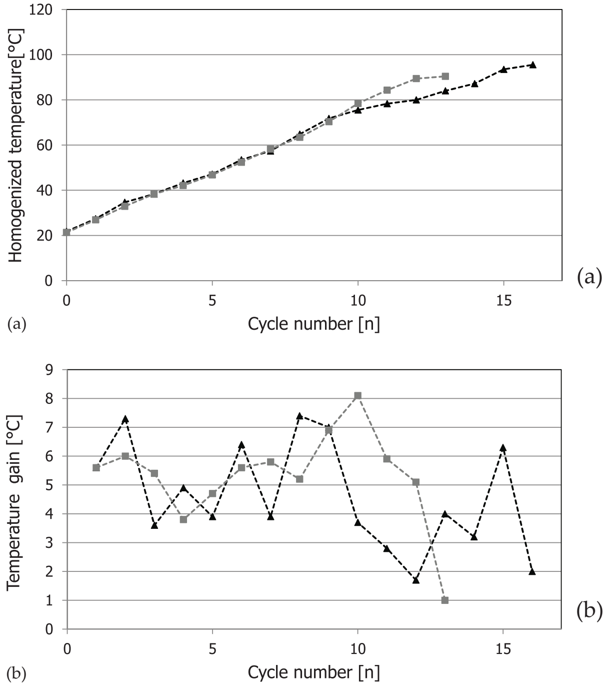

Figure 3.17. Temperature development during two separate experiments with the 21 mm inner diameter vial. The top graph (a) presents the results in terms of the temperature (T_n) versus the number (n) of experimental heating cycles. In the cycles, the duration of microwave exposure was one second. The bottom graph (b) presents the temperature gains between consecutive heating cycles ($T_n - T_{n-1}$); two irregularly fluctuating trends are found for the respective experiments. Note that the magnitude of the fluctuations is larger than the precision of the sensors (0.8°C [96]). Also note the different temperature scales of the figures.

For each vial, the set of calculated heat generation values during heating cycles is plotted as data points against the corresponding average temperature of each cycle. Figure 3.18 presents the resulting graphs for four vials with progressively larger vial diameter (8 mm, 12 mm, 21 mm and 25 mm inner diameter); the graphs for the complete set of fifteen vials are presented in Appendix D. To facilitate analysis, a continuous piecewise linear curve of three parts is fitted to the experimental data points of the graphs of Figure 3,18 and Appendix D. This regression minimizes the standard deviation between the data points and the fitted curve. In the figure captions the standard deviation (σ) and the averaged overall heat generation of the experimental data points in the graphs (A) are reported.

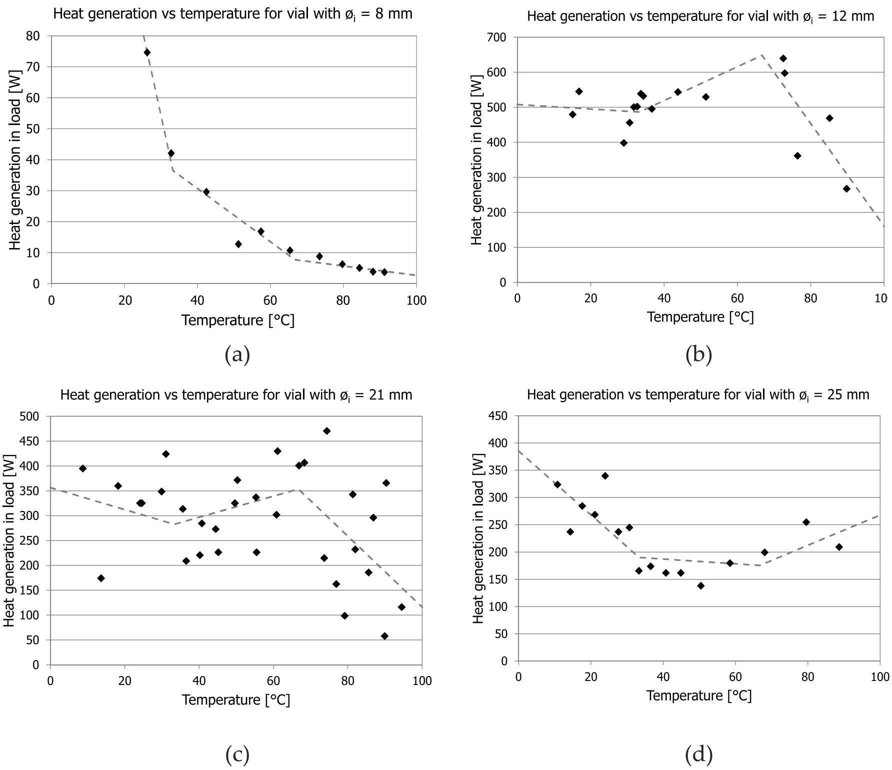

Figure 3.18. Heat generation versus temperature graphs for four vials: (a) 8 mm vial, (b) 12 mm vial, (c) 21 mm vial, and (d) 25 mm vial; both experimental data points and regression curves are included in the graphs. Note also that the scale of the heat generation differs among these graphs. Standard deviation (σ) and average heat generation (A) for the respective curves are σ = 2.8 W, A = 19 W (a); σ = 60 W, A = 491 W; σ = 88 W, A = 288 W; σ = 37 W, A = 224 W.

These graphs and representative values for σ and A characterize the heating process in each vial, which is used for mutual comparison of the vials and their heating processes. It is found that 1) the shapes of the clouds of experimental data points and the curves fitted to the clouds differ; 2) the averaged overall heat generation in each graph differs; and 3) the spread in the data points differs, as characterized by the standard deviation both in absolute (σ) and relative (σ/A) terms. These differences are apparent from the subset of vials corresponding to Figure 3.18, which is a representative selection of the full set in Appendix D.

Discussing Figure 3.18 in more detail, *Figure 3.18a* presents the heat generation power versus the average temperature during these steps for the experiments with the 8 mm inner diameter tube. Of the set of vials represented by Figure 3.18, this vial absorbs the least amount of microwave energy, which averages at 19.5 W or only 3% microwave utilization efficiency assuming 675 W of microwave power generation. Additionally, σ = 2.82 W and σ / A = 0.14.

Compared to other vials presented in Figure 3.18, the 12 mm vial (*Figure 3.18b*) absorbs the most microwave energy. This averages at 491 W or 73% of the assumed microwave power generation. The value for σ is accordingly large (59.7 W), although on relative terms (σ /A = 0.12) it compares to the 8 mm vial.

Figure 3.18c presents the heat generation versus temperature for the 21 mm vial. As was already apparent from the spread in temperature gain during the heating cycles (Figure 3.17b), there is a large variation in the step-wise heat generation values in this vial. This results in the largest absolute and relative values for the standard deviation (σ = 88.2 W resp. σ /A = 0.31) of the graphs in Figure 3.18. The averaged heat generation of 288 W is intermediate though, and of the set of four vials it corresponds best to the set microwave power of 300 W.

Finally, *Figure 3.18d* presents the results for the 25 mm vial. The heating process in this vial is intermediate both in terms of heat generation, A = 224 W, and spread in the data point, σ = 37.0 W and σ /A = 0.17, respectively.

As observed in Section 3.5 and as is calculated for the one-dimensional resonant system in Appendix C, the heating process behaves in a highly case specific manner. More specifically, the total electromagnetic dissipation in objects is strongly affected by geometrical variations as well as variations in the dielectric material properties that are involved with the electromagnetic field; the latter variations can be induced by many phenomena, for example by temperature and composition variations and by a phase change.

The geometric properties variations are shown to affect both the averaged heat generation and the seemingly stochastic spread in the heat generation. It is unclear what the exact source of the stochastic behavior is. Measurement of the cathode current (Chauvin Arnoux MINI 05 current clamp) revealed that there is a non-constant switch-on time before each heating cycle when the magnetron is started, but it was also found that the distribution of the switch-on time bears no resemblance to the spread in the heat generation. Furthermore, inaccuracies in the temperature measurement cannot be ruled out. However aside from this, as was mentioned before, we suspect that the variations in heat generation can partially be attributed to a strong amplification of small imperceptible variations in, for example, liquid volume, vial position or magnetron temperature. Additionally, small gas or vapor bubbles that enhance microwave reflection could have formed in the vial. A last important contributor to the stochastic behavior could be the unstable operating regimes of the magnetron [65,67,68] that result from the forward and backward interaction between the applicator and the non-linear magnetron characteristics.

From the fitted curves of the complete set of fifteen vials (Appendix D), heat generation versus diameter graphs were determined at five temperatures, 20°C, 40°C, 60°C, 80°C and 100°C. These graphs, presented in Figure 3.19, are strongly and irregularly fluctuating with large gradients (high peaks and low dips) over the range of diameters. Additionally, these results reveal the parametric interdependence in resonant fields; the heat generation versus diameter curves change for each temperature. In particular, the general shape of the lines change and peaks shift to different diameters.

Aside from this, an apparent steady drop in heat generation emerges with increasing temperature. This is caused by heat loss due to evaporation and boiling; since the latent heat of evaporation of water is high compared to the specific heat, evaporation of only a small amount of water withdraws a relatively large amount of heat from the system. No additional compensation for this effect is incorporated in our calculation though, because the conclusions we draw below are not affected by it.

Both Figure 3.19 and the one-dimensional resonant system described in Appendix C exhibit a fluctuating trend of alternatingly high and low heat generation under geometric variation. Underlying these observations are the interfering wave fields; the alternating pattern of constructive and destructive interference manifests itself not only in a non-uniform spatial distribution (Section 3.5) of the field intensity or amplitude, but also in an alternating relation between geometry and, collectively, energy transfer, electromagnetic dissipation, and heat generation. The complex fluctuating and parametrically interdependent behavior is *inherent to resonant fields*.

As is apparent in Figure 3.19, the actual heat generation in the vials deviates considerably from the set 300 W of microwave power, both upward and downward depending on the conditions. Assuming the aforementioned 675 W of microwave power generation, a secondary axis is included in Figure 3.19 for the utilization efficiency of microwave power. The efficiency fluctuates between very high (~90%) and very low values. Due to the strong and irregular fluctuations, it would be difficult to optimize this type of system for a high efficiency when it is subjected to variations in dielectric materials properties, as is the case in chemical processing in general. More specifically, dynamically progressing reaction coordinates, temperature variations, phase changes, and hydrodynamic variations (fluid surface variations and flow) would dramatically complicate optimization of the microwave utilization efficiency.

3.6.3 Simulation results and extended parametric study

The investigation on the parametric sensitivity is continued by means of simulations. The fact that the overall heat generation is considered, rather than the detailed distribution over the volume of the load, permits a number of simplifications that reduce the computational demand. More specifically, the study considers the effects of variation of the uniform load temperature. Heat generation and transfer are no longer simulated. Instead, the homogeneous and time-invariant dielectric permittivity of water corresponding to the load temperature under investigation is imposed over the water volume. Electromagnetic dissipation remains accounted for with respect to the electromagnetic analysis, but is no longer processed further as heat generation. In this approach only the electromagnetic interactions remain to be simulated, which avoids time-consuming dynamic heat transfer and fluid dynamic simulations. Additionally, by omitting the mesh size sensitive fluid dynamics, the mesh can be applied considerably courser without adverse effects on the results, which further reduces the computational demand. The mesh sizes that were used range from 54.000 to 111.000 elements depending on the diameter of the vial simulated. Since no electromagnetic dissipation other than dielectric heating of the water in the vial is assumed to occur in the applicator section, the net power transfer towards the applicator, as calculated following the procedure in Figure 3.8, equals the heat generation in the load.

Figure 3.20 presents the simulation of the parameter variations in Figure 3.19; it shows heat generation versus inner diameter graphs for five different temperatures: 20°C, 40°C, 60°C, 80°C and 100°C. The simulated graphs differ quantitatively from the experimental results, because we simulate a highly sensitive system with a simplified model based upon limited information. As mentioned in Section 3.5, We consider the magnetron to be the most significant source of modeling error for two reasons: first, it is a component with non-linear characteristics and it has a complex interaction with the applicator section of the system; second, the magnetron model is fitted to data that was obtained experimentally with the same type of magnetron [91], but under conditions that match our experiments and simulations neither in the scattering properties that the magnetron “sees” nor in the power applied to the magnetron. On a general note, avoiding the forward and backward interactions over the microwave circuit may improve the predictability of systems, for example by including an isolator in the microwave circuit to absorb all backward traveling fields. This approach is not applicable to the Discover and many other systems, though.

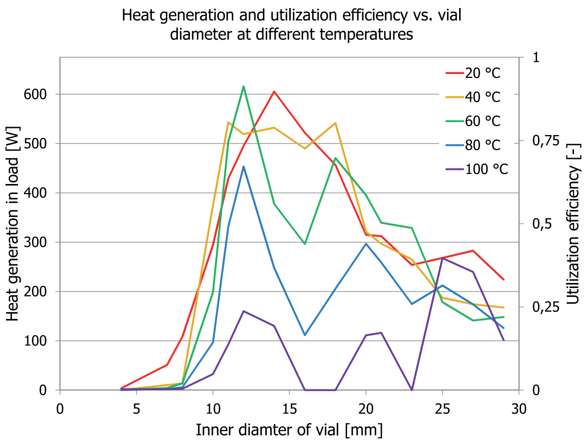

Figure 3.19. Heat generation versus inner diameter of the vials at 20°C, 40°C, 60°C, 80°C and 100°C. A fluctuating pattern of peaks and dips emerges in these graphs. The secondary vertical axis indicates the utilization efficiency for 675 W of generated microwave power as defined in equations 1 and 2.

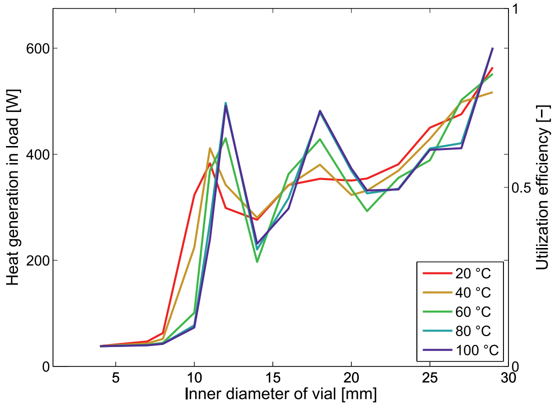

Figure 3.20. Simulated energy transfer – equal to heat generation – versus the inner diameter of the vials at 20°C, 40°C, 60°C, 80°C and 100°C. As with the experiments, a fluctuating pattern of peaks and dips emerges. The secondary vertical axis on the right indicates the utilization efficiency of the microwave field according to the definition of Equations 3.1 and 3.2.

3

Despite the quantitative mismatch, similar fluctuating behavior is observed in the simulations (Figure 3.20) as was found experimentally (Figure 3.19). Furthermore, temperature, which affects dielectric properties, has again a strong effect on the relation between heat generation and diameter. We will proceed by using this model to further qualitatively demonstrate the parametric interdependence in this kind of system. Variation of the following additional parameters is simulated: water level in the vial, wall thickness of the vial, and vertical position of the vial.

Figure 3.21 shows simulated heat generation versus diameter graphs for the base case water level (40 mm) and for water levels of 20 mm and 30 mm. Variation of the water level in the vial has an effect similar to variation of the water temperature: the positions of the peaks and dips shift somewhat and their heights change.

A different effect can be observed in Figure 3.22 for the variation of the vial wall thickness. Figure 3.22 presents simulated heat generation versus diameter graphs for 1) the base case situation with thicknesses of 1.5 mm or 2.0 mm (see Table 3.2), 2) the situation with walls of zero thickness (no walls), and 3) for the situation where all walls are 3.0 mm thick. Figure 3.22 shows that for all cases a thicker glass wall enhances heat generation in the vials. This behavior resembles that of other electromagnetic systems such as, for example, an anti-reflective coating on a lens or a quarter wave matching circuit. What these systems have in common is the presence of two domains of different media between which there is a section of intermediate electromagnetic properties; in these cases, the presence of this section enhances the electromagnetic energy transfer between the domains due to the smoother impedance variation over the length of the section. Appendix C further illustrates this phenomenon by discussing an anti-reflective layer in a one-dimensional configuration.

Variation of the vertical position of the vial has little effect on the total amount of heat generation. Figure 3.23a presents heat generation versus diameter graphs for the base case that has the vial bottom 35 mm above the cavity bottom and for the case in which this distance is reduced to 15 mm. It can be seen that the change in the vertical position of the vial has little effect on the total amount of heat generation. Nevertheless, this does not necessarily imply that nothing has changed. Figure 3.23b shows the axial distribution of heat generation in the vial over 10 layers of equal volume in the 10 mm inner diameter vial. It shows that if the position of this vial is lowered by 20 mm, the focal point of heat generation shifts from the top half of the vial to the bottom half.

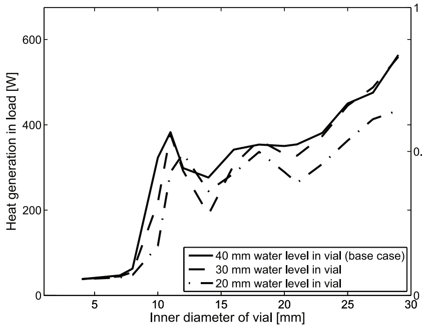

Figure 3.21. Heat generation versus vial inner diameter for different water levels at a water temperature of 20°C.

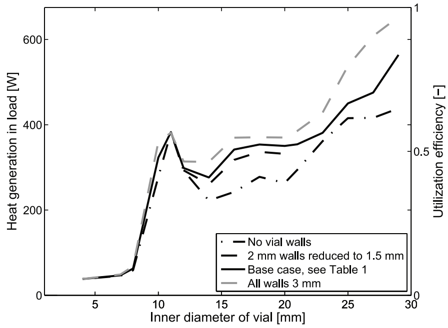

Figure 3.22. Heat generation versus vial inner diameter for different vial wall thicknesses at a water temperature of 20°C.

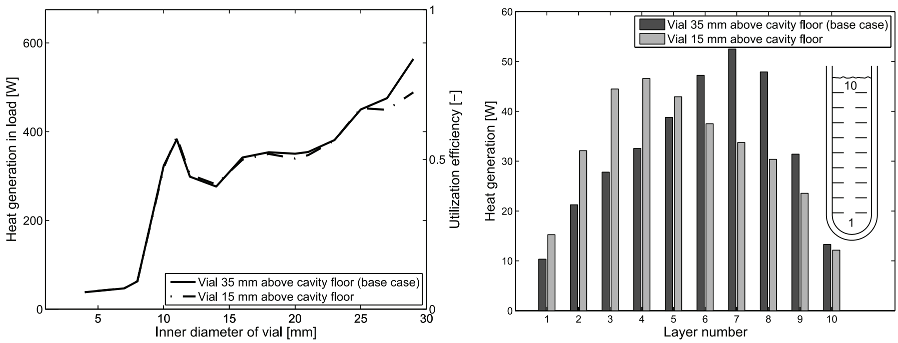

(a) (b)

Figure 3.23. Effect of the vertical position of the vial on the relation between heat generation and diameter (a) and on the axial distribution of heat generation in the 10 mm inner diameter vial (b). The vertical position of the vial has little effect on the total heat generation, whereas the distribution of heat generation in the vial is affected considerably.

The system under consideration does not lend itself well for beforehand prediction, due to the fact that any arbitrary parametric variation may have a variety of effects. Consequently, as pointed out previously in this section, the lack of information makes it difficult to achieve accurate simulation, because the parametric interdependence and sensitivity call for a highly detailed description of the system in order to achieve accurate predictions.

This demand, however, contrasts with common practice in this field of research for two reasons: 1) precise control over geometric parameters is hard to obtain due to inherent practical limitations with respect, for example, to glassware manufacturing tolerances and hydrodynamic variations; 2) detailed dielectric information is often missing. More specifically, the dielectric properties of pure components are reported, but not the properties of mixtures of solvents, reactants, catalysts and reaction products under various temperatures and reaction coordinates. Incidentally, the focus is often limited to the electromagnetically dissipative properties of fluid or solid matter.

Clearly, in view of our findings, better definable non-resonant systems are needed for either quantified prediction or reproducible experimental investigation of the microwave-chemical interactions. It may be argued that temperature control could partially alleviate the indeterminacies by regulating temperature at a predetermined set point, but this is an unsatisfactory arrangement for several reasons. *First*, for fast chemistries it may not yield sufficient control over the conditions, as the time in which this set point is reached could matter in the overall performance of the process. *Second*, if it cannot be quantified how much microwave energy is dissipated in a sample, how much is scattered and what the field intensity is, then any direct interaction of the microwave field with the chemistry (i.e. not due to temperature effects) that might possibly occur cannot be confidently related to the microwave field even though temperature is known. *Third*, as pointed out in Section 3.6.2, the utilization efficiency of the microwave energy cannot be monitored nor optimized if the electromagnetic interactions are not quantified.

3.7 Conclusions

This chapter explores the practical limitations of heating with a resonant microwave field in a non-tailored off-the-shelf system. This is done via an extended case study of a simple exemplary process. The process under consideration is the heating of a water filled vial in a single-mode cavity (CEM Discover) that is a popular device in the context of microwave enhanced chemistries. Both experimental methods and simulations were applied to this end, in which the modeling approach that was taken accounts for the forward and backward interactions in the microwave circuit via network analysis. We investigate the spatial and temporal distribution of heat generation as well as the sensitivity of the overall heat generation to parametric variations.

Heating is distributed non-uniformly in space and is highly sensitive to (even minor) variations of geometric and operating variations. The experimental approach in this context uses two complementary measurement techniques, being fiber optic probes and thermally sensitive dyes. In combination with simulations, it is shown that the standing wave patterns associated with resonance are strongly dependent on the geometry and the properties of the medium in which the microwave field is present.

Regarding the parametric sensitivity of the overall heat generation, both experimental and simulation results exhibit irregular and strongly fluctuating relations and complex interdependent interactions between total heat generation in the resonant microwave field and several parametric variations. The fact that such behavior is observed in all cases demonstrates that it is inherent to resonant fields in general.

All in all, the capricious nature of resonant fields of this generic non-tailored system reveals the challenge to quantifiably predict and manipulate the chemo-physical interactions in microwave enhanced chemistries. Sole consideration of the dissipative dielectric properties of fluid or solid matter, which is often done in the relevant literature, is not sufficient. Rather, *all* geometrical and medium parameters involved with the microwave field should be taken into account, including their dependency on secondary phenomena, such as, for example, temperature or hydrodynamic variations. All these parameters need to be considered in order to obtain predictable and controlled process performance. This could turn out to be unfeasibly complicated for non-tailored, of-the-shelf systems that present a fully three-dimensional electromagnetics problem, like the Discover, which in addition do not allow any spatial optimization of the microwave field.

Contrasting to these findings, from the previous chapter it may have appeared that the analysis and design of resonant microwave fields in process systems do not need to be as complicated as this present chapter suggests. Of course, Chapter 2 considered systems that are highly simplified and idealized in many aspects, most notable in this respect would be the reduced spatial dimensionality. Likewise, the next chapter considers custom built systems that can be approximated as two-dimensional, rather than three-dimensional, but in contrast to the systems in Chapter 2, the parts that make up the custom built systems are available commercially. Chapter 4 hence continues the exploration of the options for predictable and optimized application of resonant microwave fields in microstructured reactor systems.

Chapter 4

Rectangular Waveguides as a basis for microwave enhanced continuous flow chemistries

Chapter 1 and 3 describe the narrow set of microwave cavity systems that is usually considered in the context of microwave enhanced chemistry. The present chapter aims to widen the current scope by exploring the potential of rectangular waveguides as a basis for resonant microwave applicator systems. It is demonstrated that such systems offer microwave field patterns that are relatively simple and predictable, which makes processing amenable for adaption to specific requirements and for optimization. The feasibility of long residence time continuous flow chemistries under microwave conditions is demonstrated in a novel reactor type that the rectangular waveguide uniquely supports.

The contents of this chapter were adapted from the work published in:

G.S.J. Sturm, A.Q. van Braam Houckgeest, M.D. Verweij, T. van Gerven, A.I. Stankiewicz, G.D. Stefanidis
"Exploration of Rectangular Waveguides as a Basis for Microwave Enhanced Continuous Flow Chemistries"
Chem. Eng. Sci. 89 196–205, 2013; doi: 10.1016/j.ces.2012.11.039

4.1 Off-the-shelf technology

This chapter explores the limits and possibilities of microwave heating systems whose design is based on standard sized rectangular waveguide sections. Although these systems cannot be bought off-the-shelf as whole units, as is the case for some of the systems described in the previous chapters, their parts are standardized and commercially available. This type of system has already been used for research in chemical processing context [98-101], but this research did not primarily focus on the microwave field interactions. In principle, the rectangular waveguide addresses some of the issues identified for the cavity systems considered in the previous chapters. In particular, 1) the field is relatively simple and two-dimensional by approximation, which makes it easier to predict and permits optimization of the field itself and/or the reactor configuration; further 2) the system can be scaled by increasing the total length of the waveguide sections. We investigate the interactions of the microwave field with continuous flow millireactor (2.0 – 3.5 mm inner diameter) systems for a number of aspects that include field perturbation and manipulation, reactor orientation, and the interaction between multiple reactors. In the last section, the chapter presents a new adaptable, predictable and efficient continuous flow reactor configuration that is uniquely supported by the rectangular waveguide. Its operation is demonstrated for a model esterification reaction between propanol and propionic acid for propyl propionate synthesis.

4.2 Experimental setup and modeling details

In this study we consider the standard WR-340 waveguide as a basis for microwave enhanced processing systems. This waveguide size is compatible with the 2.45 GHz ISM band that is commonly used in microwave processing research [58]. The cross-sectional dimensions of the WR-340 guide are 86 by 43 mm [102]. Figure 4.1a presents a photograph of the setup we use. The orientation is such that the narrow 43 mm side of the waveguide is in the vertical plane.

The setup consists of the common parts for this type of system. The essential parts are the microwave generator and the applicator cavity. The generator section holds the variable power magnetron microwave source (10 – 1200 W) and has a waveguide section as output. The cavity is a custom made waveguide section, which has a removable lid and in both the lid and the cavity bottom there is an array of holes (5.5 mm diameter, hexagonal pattern, 8.0 mm centerline spacing). The arrangement of the lid and both arrays of holes provide flexibility and versatility in terms of access to the cavity and connectivity for sensors and flow tubes.

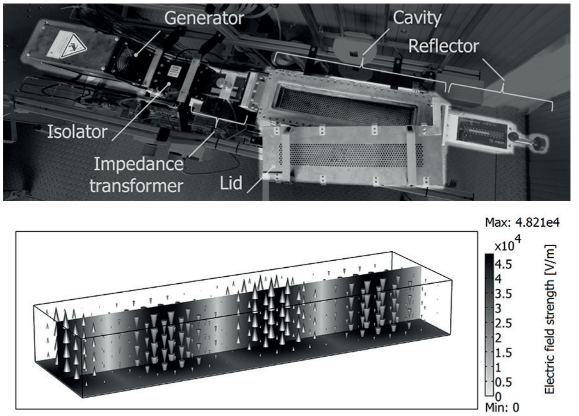

Figure 4.1. TE_{10n} cavity. Top (a): photograph of the TE_{10n} cavity setup. Bottom (b): simulation of field pattern in the cavity.

The system further includes an isolator, an impedance transformer and a variable reflector. The isolator protects the generator from reflected microwave fields; it lets a microwave field pass in the forward direction – from the generator to the cavity –, but it absorbs it in the reverse direction. This protects the magnetron from damage [73], but it also prevents the complex and hard-to-predict electromagnetic interactions between the magnetron and the heating process in the applicator cavity that were described in the previous chapter. The impedance transformer is a tunable system that can redirect a microwave field exiting the cavity back into it. Proper tuning of the impedance transformer facilitates operation with high microwave utilization efficiency. As such, a microwave utilization efficiency of around 90% or more can be obtained [65,69,73]; this would bring the overall efficiency of converting electric energy into useful heat via microwaves to ~60% for applications using a frequency of 2.45 GHz [103]. Finally, the variable reflector allows for variation of the position where the microwave field reflects at the far end of the system. Changing the reflector settings enables positioning of the standing microwave field pattern in the cavity. All parts of the microwave circuit, except the applicator cavity, were purchased from Sairem SAS [104-105].

When empty, the system supports a microwave field pattern that has one field maximum over the width of the cavity; it has no field maxima in the height direction, thus rendering it invariant in this direction; and it has an integer number of field maxima along the waveguide. Additionally, the field pattern the empty system supports has the electric field vector direction vertically oriented, perpendicular to the length direction of the cavity. These characteristics explain the "TE_{10n}" naming: *transverse electric*, *one* maximum along the broad side, *no* maximum along the narrow side, and an integer number *n* along the length [69]. This is illustrated by Figure 4.1b that presents a simulation of the electric field component in an empty cavity.

Note that the terms "waveguide" and "cavity" are interchangeable to some extent. The microwave field in our system travels forth and back in the waveguide that comprises the applicator section. It thus forms a resonant standing wave pattern. The term "cavity" is commonly used to denote an enclosed space that holds a resonant field.

Finally, the simulation environment that is used in this study is Comsol Multiphysics 3.5 with the Radio Frequency module [70] in combination with Matlab and Simulink [76]. The microwave field interactions are calculated by solving the Helmholtz representation of Maxwell's electromagnetic field interactions,

$$\nabla^2\mathbf{E} + \varepsilon_r\left(\frac{2\pi f}{c_0}\right)^2\mathbf{E} = \mathbf{0} \tag{4.1}$$

Here **E** is the complex electric field vector, *f* is the frequency of the electromagnetic field, c_0 is the speed of light and ε_r is the complex relative permittivity of the medium in which the electromagnetic field is present. The imaginary part of the relative permittivity accounts for electromagnetic dissipation, which causes heat generation. Dielectric properties of materials are obtained from Meredith [65] and Hayes [74]. The time-average electromagnetic dissipation is calculated via,

$$q = \pi f \varepsilon_0 \varepsilon'' \mathbf{E}\cdot\mathbf{E}^* \tag{4.2}$$

The electromagnetic field is solved by this software package via finite element analysis in the frequency domain imposing the appropriate boundary conditions. In all cases discussed herein, sufficiently refined meshing was applied in order to obtain grid independent results. For brevity, electromagnetic analysis is not further detailed here; for additional information one is referred to the extensive volume of literature on the subject; for example, the textbook by Pozar [69], which is an excellent starting point for further study.

4.3 Physical interactions

The relatively simple microwave field in the cavity enables consideration of the interactions of the microwave field with continuous flow systems. The effects of scattering and field vector orientation will be demonstrated here.

Since microwave heating consists mainly of dielectric heating, which is due to interaction of materials with the electric field component, heating is enhanced by placing loads in the electric field maxima. It may appear tempting to distribute loads in the field maxima that occur along the length of the empty cavity (Figure 4.1b), but it will be demonstrated here that this approach does not yield satisfactory results. Figure 4.2a is a drawing of such a configuration, which has three bundles of four water containing tubes (polyurethane, 2.5 mm inner diameter and 4.0 mm outer diameter) placed in the electric field maxima. The drawing suggests that microwave heating will occur uniformly distributed over the twelve tubes. On the contrary, the simulation of this configuration (Figure 4.2b) shows that the tube bundles distort the microwave field considerably; they reflect the microwave field, which causes the electric field maxima to appear between the bundles, rather than on the bundles. This result is verified by an experiment with an incident microwave field of 1.0 kW and a flow rate of 100 ml/min in each tube. The temperature gains in tubes are low and non-uniformly distributed (Table 4.1), which is a consequence of the unfavorable distribution of the microwave field strength over the tubes.

Table 4.1. Temperature gains in the tubes of the configuration described in Figure 4.2. The water flow rate in each tube is 100 ml/min and the incident microwave power is 1.0 kW.

Tube 1	4.3°C	Tube 5	0.4°C	Tube 9	0.3°C
Tube 2	0.8°C	Tube 6	0.5°C	Tube 10	2.0°C
Tube 3	0.8°C	Tube 7	0.4°C	Tube 11	1.0°C
Tube 4	2.6°C	Tube 8	2.8°C	Tube 12	2.2°C

The directionality of the constituent electric and magnetic vector fields plays an important role in the interactions that the microwave field has with objects. This is illustrated by a flow tube (LDPE, 2.0 mm inner diameter, 2.5 mm outer diameter) presented in Figure 4.3a that is positioned in the cavity such that it enters though the bottom of the cavity, bends to run horizontally for approximately 0.3 m along the centerline of the cavity, and bends down to exit the cavity. It thus has two sections that run vertically at the entrance and exit, and one longer horizontal section. Water flows though the tube at a rate of 15 ml/min towards the generator end of the cavity.

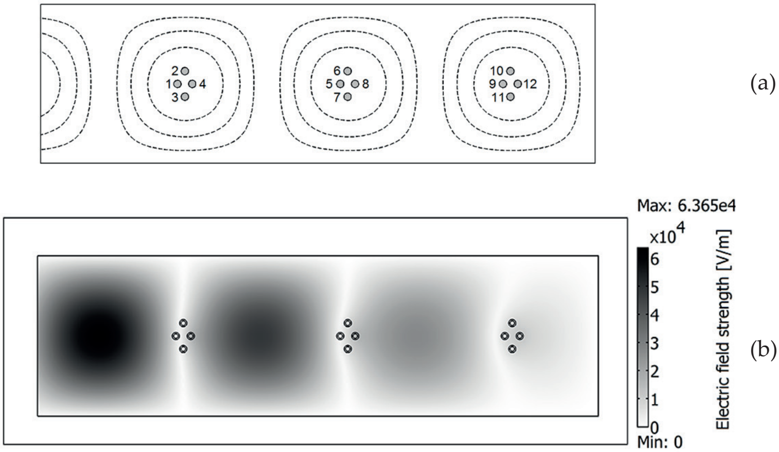

Figure 4.2. Interaction of multiple tube bundles with microwave field. Top (a): drawing of three bundles of four tubes (polyurethane containing water, inner diameter 2.5 mm, outer diameter) position in empty TE_{10n} cavity field with the empty cavity electric field distribution indicated by the dashed lines. Bottom (b): simulated electric field strength in the cavity containing these tube bundles, with an incident microwave power of 1.0 kW from the left. The simulation shows that the presence of the bundles strongly distorts the microwave field. The field reflects on the bundles causing the electric field maxima to occur between the bundles, rather than on them.

The distribution of heating in the tube was evaluated both via simulation and experiment. Figure 4.3b presents a simulation of the heating rate distribution; heat generation turns out to be concentrated in the vertical sections of the tube. This result agrees with temperature measurements inside the tube with a fiber optic temperature sensor (uncladded Neoptix T1 [96]) (Figure 4.3c); the temperature rise in the tube occurs primarily in the vertical sections.

These observations can be explained by the orientation of the electric field vector with respect to the interface between the tube and the surrounding cavity space. For the horizontal section of the tube, the electric field vector has a significant perpendicular (or normal) component over most of the circumference of the tube, whereas in the vertical sections, the electric field vector is practically tangentially oriented over the entire tube circumference. This difference affects the electric field strength inside the tube. The boundary conditions for the electric field (Figure

4.4a) are such that for a field in the normal orientation, the field strength inside the tube is reduced by the ratio of the dielectric permittivity outside of the tube to the permittivity inside the tube. In contrast to this, for a tangentially oriented field there is no reduction in the field strength. Consequently, in the vertical sections of the tube, the field strength is as high as it is in the surrounding cavity space and the heating rate is high. On the contrary, in the horizontal section, the field strength in the tube is diluted because of the significant perpendicular component in the orientation of the electric field vector with respect to the interface between the tube and the surrounding cavity space. This is further illustrated by Figure 4.4b, which presents a static electric field analysis of a dielectric cylinder oriented perpendicularly to the electric field vector.

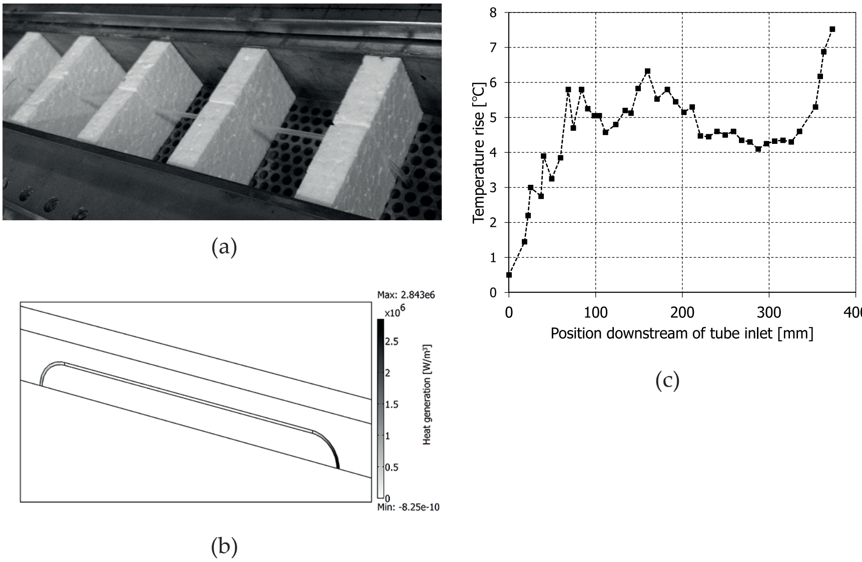

Figure 4.3. Effect of orientation with respect to microwave field. Figure (a): photograph of tube in centered flow path; notice the vertical inlet section on the right. Figure (b): simulation of heating rate in tube. Figure (c): measured temperature profile inside tube. Microwave heating concentrates in the vertical sections of the tube.

The findings presented in this section demonstrate that the phenomena occurring during microwave heating processes are not limited to only the absorption of microwave energy in dissipating objects, but that these objects also scatter the microwave field and change its distribution. In general, microwave fields are affected by the presence, geometry, orientation and medium properties of any object they come into contact with. This must be taken into account in order to achieve predictable and controlled performance in microwave enhanced processes. On a more practical note, since the flow tubes (reactors) are shown to couple poorly with the microwave field unless it is oriented vertically, multiple of these short vertical passes are needed to obtain sufficient processing time if this were to be required. The next sections will explore two strategies to approach this requirement.

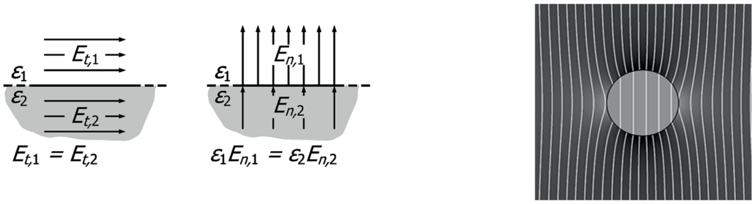

(a) (b)

Figure 4.4. Figure (a): Boundary conditions for the electrical field over interfaces between different dielectric media for a flat boundary [69]. Figure (b): static electric field analysis for a cylindrical dielectric object oriented perpendicularly to the field (b). In Figure (b) the grayscale indicates the field strength (darker zones indicate higher intensity) while the white lines represent the field lines.

4.4 Symmetrical microwave field application

The first approach for increasing the processing volume in the cavity is based upon utilizing symmetry with the aim of obtaining highly controlled and equal conditions over multiple tubes. As opposed to the cases discussed earlier, microwave scattering is taken into account in this approach. Figure 4.5 presents a photograph of a four-tube configuration. These are identical glass tubes with water flowing through them. In theory, for equal inlet conditions in terms of flow rate and inlet temperature, symmetry would ensure equal conditions over the width of the cavity. Furthermore, tuning of the reflector position may enable equal conditions in the tubes along the length of the cavity too. Additionally, the tubes have a small 3.5 mm diameter, which limits the variation in the electric field strength over their cross section (see Chapter 2). Therefore, theoretically, careful adjustment of flow rate, inlet temperature and reflector position may enable a fourfold increase of the processing volume while maintaining controlled and uniform processing conditions.

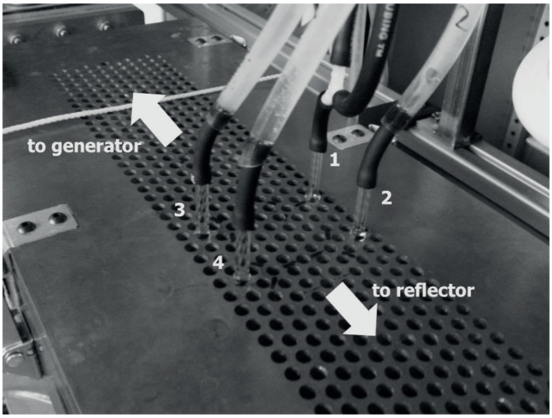

Figure 4.5. Photograph of four glass tubes (inner diameter 3.5 mm, outer diameter 5.0 mm) running through the cavity. Tube numbers and orientation with respect to generator and reflector are indicated.

A fully coupled multiphysics simulation is used to determine an operating point for which a temperature gain of 40°C occurs in all tubes for inlet flow conditions of 10°C and 100 ml/min in each tube. The primary aim of this model is to account for the electromagnetic interactions to arrive at an evenly distributed heating rate distribution over the four tubes. In order to limit the computational requirements, a number of simplifications are incorporated in the model. First, the microwave field is simulated in two dimensions, because it is height invariant by approximation. The spatial domain of the two-dimensional electromagnetics model comprises the empty cavity volume, the tube walls and the fluid volume. Second, since the tubes are narrow, the conditions in terms of temperature and electric field distribution are evaluated along their axial dimension only; a series capacitor equivalent circuit (one-dimensional electrostatics) is used to calculate the electric field distribution and heat generation in the water volume of the tubes along the axial direction while taking into account the temperature dependent dielectric properties of water. Third, a simple heat transfer model is used in which one-dimensional axial discretization is applied to both the water volumes and the tube walls. Heat transfer between the discretization cells of the water volumes and the tube walls, and heat loss to the surroundings are calculated by means of lumped heat transfer coefficients. These heat transfer coefficients were obtained from an additional model of the axisymmetric tube geometry that comprises laminar flow, uniformly distributed heat generation in the water volume, conductive and convective heat transfer and heat loss to the surroundings. Figure 4.6 presents a diagram of interconnected variables of the model and auxiliary information. An ODE solver in Simulink was used to calculate the steady state behavior of the system by running the dynamic heat transfer model while updating the electromagnetic field at every time step until it reached stable equilibrium. This was simulated over 5 seconds of operating time, which required 52 minutes of simulation time owing to the frequent microwave field updates. The memory requirement for the simulation was 70 MB. An optimization routine in MATLAB was used to determine the manipulated parameters for which the operating point is reached with the aforementioned outlet conditions. Figure 4.7 presents the relevant parameter values for the targeted operating point and Figure 4.8 presents the amplitude distribution of the electric field under these conditions. These conditions are used as base case for further parametric study.

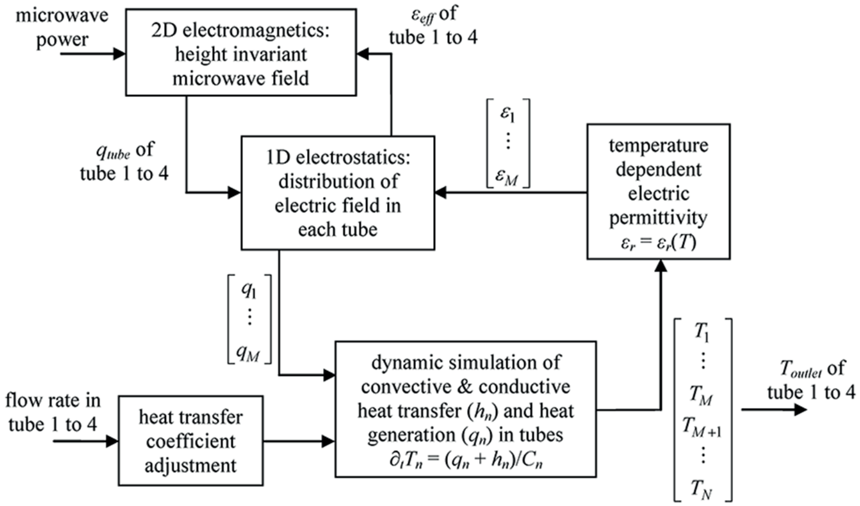

Figure 4.6. Diagram of interconnecting model variables. The model couples electromagnetics with heat transfer and fluid dynamics. The electromagnetics model is split into the – by approximation – height invariant, two-dimensional microwave field in the cavity; and into the – also by approximation – one-dimensional electrostatic distribution of the electric field in the water contained in the tubes. The water volume and the glass wall of the tubes are discretized along the length; in the diagram, domain 1 to M represent the water and domain M+1 to N (= 2M) represent the glass wall. The electrostatics model calculates the effective electric permittivity of the water in the tubes, which serves as input to the 2D electromagnetics model. The electromagnetics model calculates the overall heating rate in each tube, which is split in the electrostatics model over the discretized water volume. Heat generation and transfer are combined in a dynamic simulation from which the outlet temperatures of the tubes are derived.

The base case settings that result from the simulation were applied to a continuous flow experiment with 20 s of microwave exposure. The outlet temperatures of the four tubes during this experiment are presented in Figure 4.9. It can be seen that the outlet streams reach their end temperatures very fast (in less than one second), but these temperatures are unstable and fluctuate. Moreover, a strong correlation between the respective outlet temperature transients exists. This behavior is indicative of a strong interaction between the tubes. Furthermore, although a very high rate of temperature increase occurs in the tubes (~120°C/s), the outlet temperatures do not reach the exact target values of 50°C, nor are they exactly equal. This small mismatch between simulation and experiment may be attributed to idealizations and inaccuracies in the model, but in view of the capricious characteristics of the resonant system the predictive quality of the model is very good.

Four parameter variations have been evaluated in a parametric study of this system. These are the inlet temperature of tube 1, the flow rate of tube 1, the magnetron power output, and the reflector position. These investigations are conducted both by simulation and – within practical constraints – experiment. The experimental data has been averaged over at least 20 seconds to filter out the dynamic fluctuations.

Figure 4.10a and 4.10b clearly demonstrate the interaction between the tubes that was mentioned earlier (Figure 4.9). A variation in inlet temperature (Figure 4.10a) or flow rate (Figure 4.10b) in tube 1 affects the heat generation and outlet temperatures of all tubes. This behavior results from the temperature dependent electric permittivity that affects the resonant microwave field pattern in the cavity. The microwave field forms a coupled system throughout the cavity: a variation in one point affects the field *over the entire volume*.

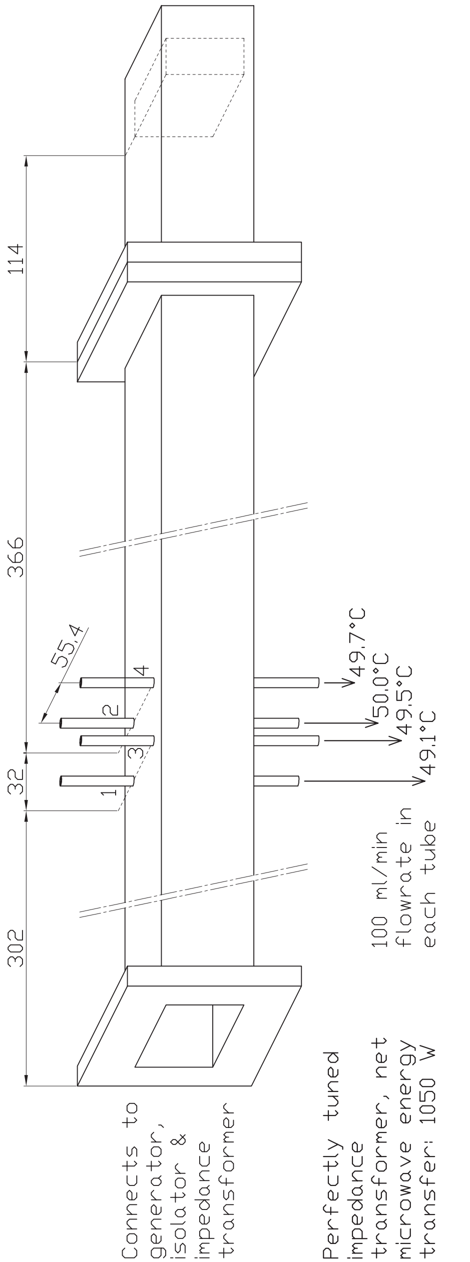

Figure 4.7. Parameter values for targeted operating point in Figure 4.8.

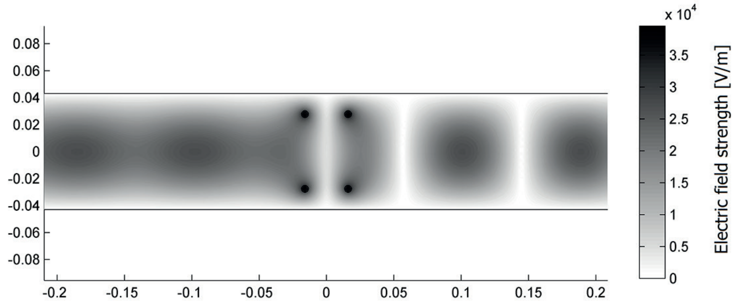

Figure 4.8. Simulation of electric field component's amplitude in TE_{10n} cavity with four continuous flow tubes that have equal flow rate, inlet and outlet temperatures, and heat generation. The scale is in meters.

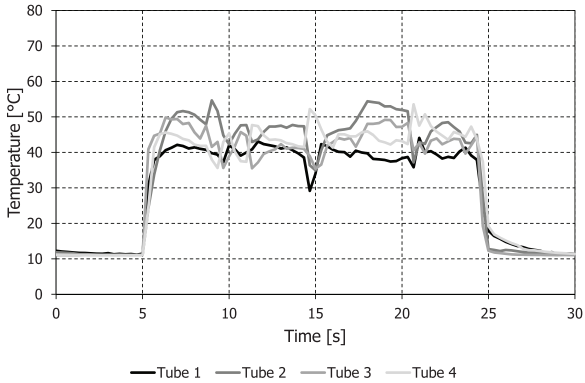

Figure 4.9. Transient behavior of outlet temperatures during 20 s of microwave exposure. The outlet temperatures respond fast to the microwave field and a high temperature increase is attained in a short residence time. The outlet temperatures do not stabilize though and there appears to be interaction between the tubes.

The results for the variation of microwave power (Figure 4.10c) show a dramatic effect of the interaction on the temperature distribution; at high microwave power, the symmetry is lost even though the inlet conditions are symmetrical. The lines of the symmetrical tube pairs (1 and 3 with 2 and 4, respectively) split if the power is increased beyond a certain threshold. The simulations show this very clearly, with the outlet temperature of tube 1 even dropping strongly with increasing microwave power. The experimental results are less extreme, but the outlet temperatures of symmetrically positioned tubes still separate and the outlet

4

temperature of tube 1 drops at higher microwave powers. This can be explained by the scattering characteristics of the tubes. If in one tube temperature rises, this leads to a drop in the electric permittivity of the medium contained in it. In turn, this will cause the interface between the tube and the surrounding space to scatter less, so that a larger portion of the microwave field will transmit into the tube causing more electromagnetic dissipation and further temperature rise. This mechanism thus creates a self-enhancing disturbance, which explains the loss of symmetry under symmetrical inlet conditions.

The relation between outlet temperature and reflector position is presented in Figure 4.10d. It can be seen that the temperatures change periodically with the reflector position, which is due to variations in the position of the minima and maxima of the standing wave field relative to the tubes. In particular, the outlet temperatures of the pairs of symmetrical tubes rise and fall asynchronously with the reflector position, because the pairs are in different locations along the length of the cavity and, hence, along the standing wave field itself. Consequently, the numerical results in Figure 4.10d predict two positions in which the outlet temperatures of the pairs cross: in the 114 mm position, for which the model has predicted the desired equal temperature rise of 40°C in each tube, and in the 84 mm position. Likewise, the experimental data shows that the outlet temperatures are indeed converging around the 114 mm position.

Collectively, it can be deduced from Figure 4.10 that field interactions and complex behavior are inherent to cavities and resonant microwave fields. Consequently, predictability and control will always be compromised to some extend if the volume in which the field is controlled is large enough to contain a substantial portion of a standing wave. This translates itself into a strong coupling between multiple loads, which makes it difficult to operate them as separate entities.

Nevertheless, Figure 4.10 clearly shows good qualitative and quantitative agreement between experimental data and model predictions. This implies that controlled and predictable application of microwave fields according to custom requirements can be obtained provided that the two following conditions are met. First, *microwave scattering must be taken into account*. In contrast to the unfavorable behavior of the case presented in the previous section, the results of this section demonstrate that careful adjustment of process settings for microwave field scattering on solid and liquid matter enables prediction and control of the field. This is an aspect that is frequently overlooked in the context of microwave-chemical interactions where commonly emphasis is placed only on the dissipative dielectric properties of media. Second, *a morphologically simple microwave field pattern in a geometrically plain and well-known applicator is required*, as for example the two-dimensional (by approximation) microwave field in the rectangular waveguide proposed in this chapter.

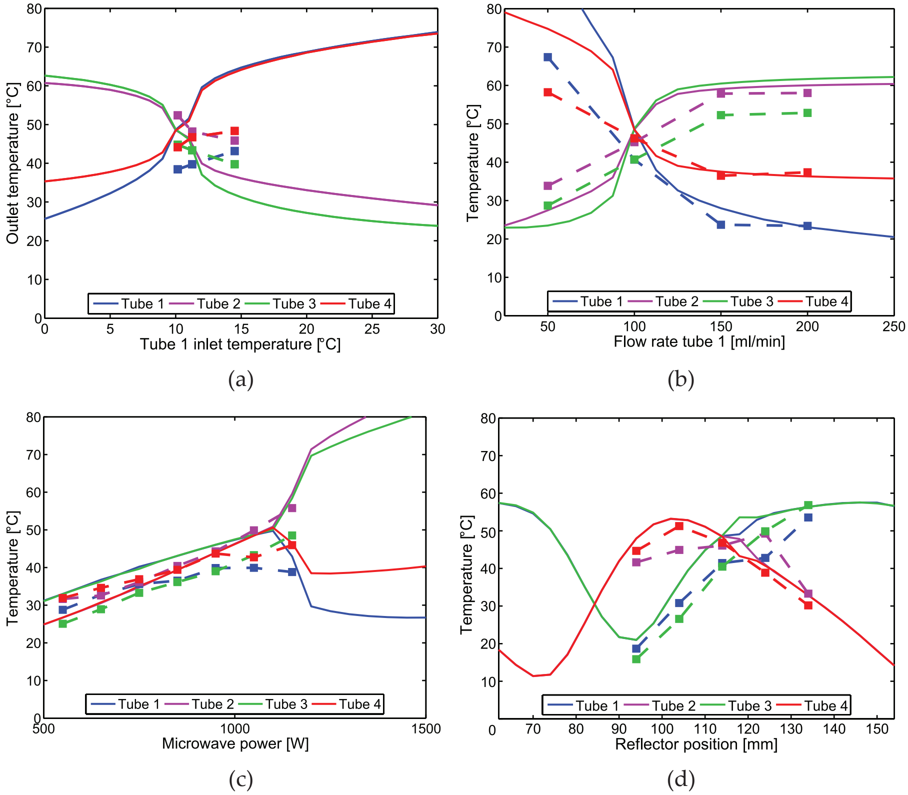

Figure 4.10. Parametric study for variation of: the inlet temperature of tube 1 (a), the flow rate in tube 1 (b), the microwave power (c), and the position of the reflector (d). This study was conducted both by simulation (solid lines) and experimentally (dashed lines with markers).

4.5 Adaptable continuous flow microwave coil reactor

For reactions that do not occur very fast, a single pass or a limited number of passes through vertically oriented tubes would require an impractically low flow rate in order to attain sufficient residence time under continuous flow operation. In this section we present a coiled reactor configuration that permits much longer flow paths. Figure 4.11 presents this configuration as it is placed in the cavity. It consists of a flexible tube (LDPE, 2.0 mm inner diameter, 2.5 mm outer diameter)

4

that forms a regular series of loops around an expanded polystyrene support. The loops are shaped to have a relatively large vertically oriented path to provide good coupling with the microwave field. There are 47 loops in total with a 10 mm mutual centerline separation; the total length of the flow path in the cavity is 4.5 m.

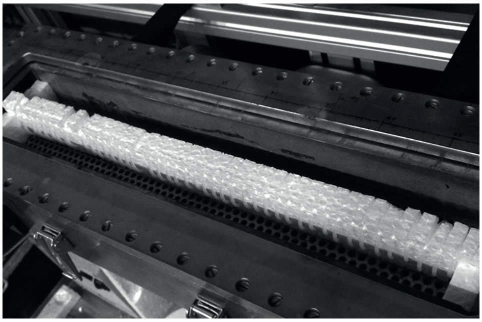

Figure 4.11. Photograph of coil reactor configuration.

The operation of this reactor is investigated with the zinc-triflate (98%) catalyzed esterification of 1-propanol (ProOH) with propionic acid (ProAc) to synthesize n-propyl propionate (ProPro) (all chemicals were purchased from Sigma-Aldrich). The stoichiometry of the reaction is,

$$C_3H_7OH + C_2H_5COOH \rightleftharpoons C_2H_5COOC_3H_7 + H_2O \tag{4.3}$$

This case system has previously been studied under microwave conditions; Altman et al. have shown that this reaction performs well under microwave conditions [106] and that the dissipating properties of the alcohol fraction enable effective heat generation [107]. The base case inlet composition of our study is an equimolar feed ratio with 2 wt% of dissolved catalyst. It was shown by Altman and co-workers [106] that at the nominal temperature of 100°C, the system reaches chemical equilibrium (~66% conversion) after several hours under conventional heating.

Due to the narrow inner diameter of the tube and the large number of bends, temperature measurement by fiber optic temperature inside the tube along its length in the microwave field proved impossible. Instead, temperature is determined by thermal imaging and outlet temperature measurement. Figure 4.12 presents two thermal images (SP Thermoview 8300) that demonstrate the performance of the coil reactor in terms of heat generation and temperature levels. The images are made by removing the lid of the cavity, only seconds after switching off the microwave source. The results show that the temperatures are high enough to drive the reaction. The temperature distribution indicates that heating decreases with the distance to the generator. Additionally, the standing wave pattern of the microwave field appears along the length of the cavity in the thermal images of Figure 4.12 as a regular pattern of brighter zones that correspond to local maxima in the temperature distribution.

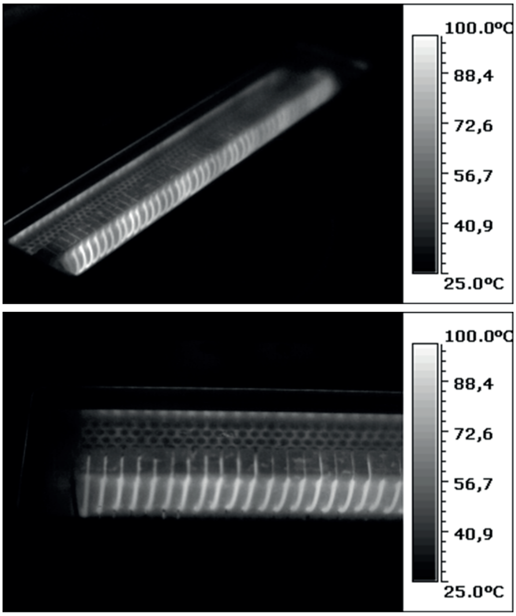

Figure 4.12. Thermal images of the coil reactor that demonstrate the heating performance. Microwave power of 100 – 200 W was applied. Top: overall view; the temperature peaks along the cavity length corresponding to the brighter color zones indicate the standing wave pattern along the length; bottom: close-up thermal image. Sufficiently high temperatures are reached to drive the reaction.

In addition to thermal imaging, the outlet temperature is measured with a thin (0.5 mm diameter) thermocouple inside the tube, but outside of the microwave field. Figure 4.13 presents the outlet temperatures for the aforementioned inlet conditions at microwave powers of 60 W and 120 W (Figures 4.13a and 4.13b, respectively). For the lower power setting, the measured outlet temperature is constant and the outlet flow is smooth (Figure 4.13a), but for the higher power setting the temperature fluctuates wildly and the outlet flow is unsteady (Figure

4.13b). This is due to cycled boiling occurring inside the reactor stream at higher microwave power, which causes discontinuous liquid flow at the outlet of the reactor.

To understand operation of this reactor, the effects of temperature and residence time are investigated. Both, however, are difficult to quantify. As far as temperature is concerned, the overall process temperature can be determined via thermography, but not continuously during operation. On the other hand, outlet temperature can be continuously measured, but it is only a poor representation of the process temperature due to the unsteady outlet flow. Therefore, microwave power is parametrically varied to indirectly investigate the role of process temperature. As far as residence time is concerned, the unsteady outlet flow hinders its accurate determination. Therefore, the ratio of reactor volume to volumetric flow rate is used as representative parametric variable for the residence time. Besides, the base case conditions for these experiments are the aforementioned equimolar inlet composition with 2 wt% of dissolved catalyst, fed into the reactor at a rate of 0.5 ml/min (30 minutes residence time), and 80 W of microwave power.

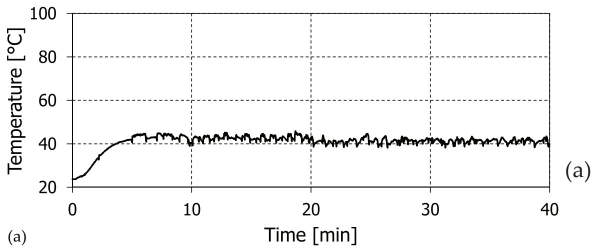

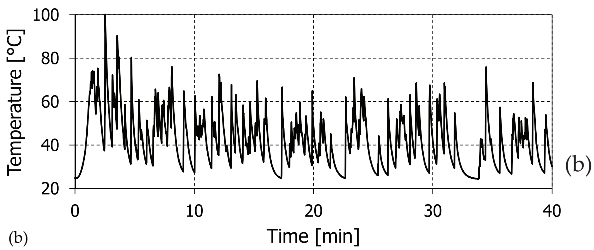

Figure 4.13. Two outlet temperature transients during continuous flow operation (0.5 ml/min). Top (a): transient at 60 W. Bottom (b): transient at 120 W. The fluctuations that occur at 120 W are due to boiling.

In the *first series of experiments*, microwave power is varied from 60 W to 200 W. In the experimental procedure, the process is run for at least 40 minutes to let it reach stationary operation. The outlet conversion is subsequently repeatedly sampled until at least three similar conversions are measured. Karl-Fischer titration is used to determine conversion via the water content. Figure 4.14 shows the results of conversion versus microwave power. The behavior is non-monotonic. Initially, conversion increases with increasing microwave power, reaches a maximum value at a power of ~125 W and then decreases with further power increase. This behavior is due to the fluctuating outlet flow at high microwave powers, which may hamper reactor performance. More specifically, at high microwave power, vapor generated by boiling pushes the fluids out of the reactor thereby cutting the processing time short. This issue can be addressed by adjusting the shape of the coil reactor, for example by widening the reactor loops on the generator side (i.e., at the front end of the waveguide). This would position the well-absorbing vertical sections of the loops nearer to the side walls of the cavity in a zone of lower electric field intensity (see Figure 4.1b). On the contrary, down the waveguide, the loops should be closer to the central zone of high field intensity to compensate for the amount of microwave power dissipated along the length. Such adjustment may result in a more uniform temperature distribution along the length of the reactor and in the prevention of boiling at an upstream location.

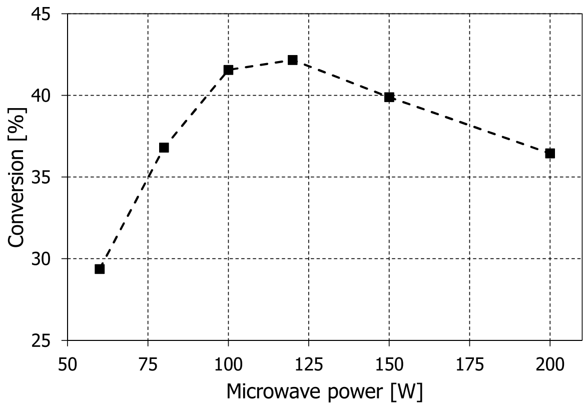

Figure 4.14. Conversion versus microwave power. The system is operated at a 0.5 ml/min equimolar feed ratio of ProOH and ProAc with 2 wt% dissolved zinc-triflate catalyst. At higher microwave power levels boiling occurs, which causes vapor to push the reactant mixture out of the reactor, thereby reducing residence time and reactor performance.

Figure 4.15 shows the results of the *second series of experiments* in terms of conversion versus the ratio of reactor volume to inlet flow rate. This ratio represents the residence time, which is varied between 12 minutes (1.25 ml/min) and 60 minutes (0.25 ml/min). The same procedures as described above are used to determine outlet conversion and to reach and verify stationary operation. As expected, conversion increases with increasing residence time. Most importantly, Figure 4.15 shows that that the employed microwave reactor configuration achieves satisfactory conversions for the given processing times. For example, 37% conversion is attained for 30 min residence time when the maximum temperature recorded via thermal imaging along the length is 76°C. Assuming a static fluid, simulation of radial heat transfer during a ten second interval between stopping the microwave generation and acquisition of the thermal image shows that 1) this wall temperature (76°C) corresponds to a maximum temperature of 89°C during the process and 2) a temperature difference of 6°C exists in the cross section of fluid. The conversion attained (37%) is approximately the same as that in Altman et al. [106] in conventionally heated batch experiments performed at significantly higher constant temperature (100°C) using the same catalyst. Moreover, they have observed similar rate enhancements under batch processing of the chemical system in a cylindrical microwave cavity.

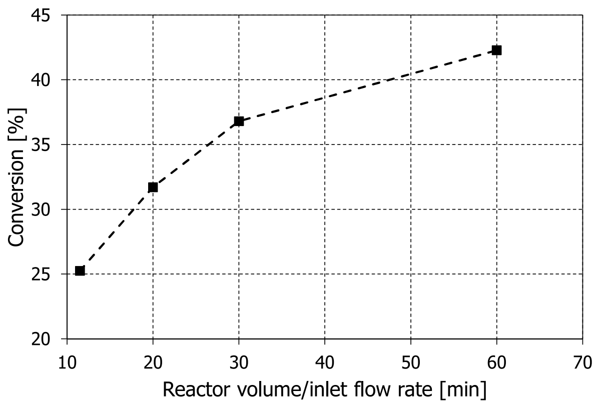

Figure 4.15. Conversion versus residence time. The reactants are fed in equimolar ratio with 2 wt% of zinc-triflate catalyst dissolved in it. Microwave power is 80 W during these experiments.

These results prove the integrated rectangular waveguide-reactor design concept to be a feasible option for microwave enhanced continuous flow chemistries, even for slow reactions requiring long residence times. The processing volume is not as constraint as in other types of single-mode cavities, because in principle the cavity can be of any arbitrary length. Furthermore, unlike other microwave applicators types that are more commonly proposed for chemical processes, the system presented herein is amenable to optimization using, for example, the shape adjustment method suggested above owing to the relatively predictable and simple microwave field. If, on the other hand, locally more intense processing conditions are aimed at, as opposed to more uniform temperature conditions along the reactor length, then a zone with narrower reactor loops and tighter spacing between successive loops would place a higher fraction of the fluid trajectory in the central zone of the waveguide where higher field intensity exists. Further, as mentioned in Section 2, impedance tuning during operation will optimize the utilization efficiency of the microwave energy at any specific operating condition. All in all, different optimization strategies can be employed depending on the particular process requirements set.

4.6 Conclusions

This chapter explores the potential of rectangular waveguides as a basis for microwave enhanced chemical processing systems. It is demonstrated that the relatively simple single-mode microwave field pattern in these resonant systems enables optimization, adaptation, and good coupling of microwave energy in fluids. *Microwave applicator cavities based upon rectangular waveguides outperform the more commonly used multimode and single-mode cavity systems in terms of predictability and control*. Furthermore, their volume is not as constraint as it is in the latter systems.

Based upon the findings on the fundamental interactions of a microwave field with a flowing medium, a novel continuous flow coil reactor concept was developed and demonstrated in a rectangular waveguide for the synthesis of *n*-propyl propionate by esterification of propanol and propionic acid. *The results prove that long residence time and high conversion are possible in continuous flow chemistries under single-mode microwave field conditions*. As opposed to the cavity systems discussed in the previous chapters, this concept can be constructed out of commercially available parts and is flexible enough to be tailored and refined to meet specific requirements.

Despite being two dimensional by approximation, the interactions in rectangular waveguides may still be complex and sensitive to variations, because this is inherent to resonant fields. The microwave applicator concept presented in the next chapter aims to resolve these issues by avoiding resonance altogether.

Chapter 5

Coaxial traveling microwave reactor

To avoid the limitations posed by resonance on microwave activated chemical reactions, a novel integrated reactor-and-microwave-applicator concept is presented. This concept is based on coaxial waveguides and traveling microwave fields. The concept is presented as a means to retain the highly optimized processing conditions that are characteristic for microreactor systems both in the context of liquid phase processing and in the context of gas phase, solid catalyst processes. Geometrical optimization for a uniform heating rate distribution is demonstrated.

The contents of this chapter were adapted from the works published resp. in press as:

G.S.J. Sturm, M.D. Verweij, T. Van Gerven, G.D. Stefanidis, A.I. Stankiewicz
"Applicator design for microwave enhanced microprocessing"
Proceedings of the 13th International Conference on Microwave and RF Heating AMPERE 2011, 48–51 (electronic version)

G.S.J. Sturm, A.I. Stankiewicz, G.D. Stefanidis
"Microwave Reactor Concepts: From Resonant Cavities to Traveling Fields"
Novel Reactor Concepts, M. van Sint Annaland and F. Gallucci (eds.), (in press).

5.1 Coaxial waveguides

As was shown in the previous chapters, resonant fields are limited in terms of spatial control over microwave fields. Therefore an alternative approach is presented here that is based upon use of traveling electromagnetic waves as opposed to standing electromagnetic waves. Traveling electromagnetic waves do not occur in confined spaces. They travel through a medium towards one direction without being reflected by reflective surfaces, such as cavity walls. As they move, part of the electromagnetic energy is dissipated to heat, according to the dielectric properties of the medium, and the remainder of the energy travels further along the path of propagation. Due to the absence of interference with microwave fields traveling in the opposite direction, resonant standing wave patterns arising from superposition of interfering waves do not occur. Contrary to resonant standing wave fields, no inherent limitation to the uniformity of the distribution of heat generation exists, and complex interactions that are detrimental for prediction and control are avoided.

Figure 5.1 shows a photograph of a typical coaxial cable. It consists of two concentric conductors with dielectric filler between them. Between both conductors a microwave field is supported. In the coaxial traveling wave reactor concept this is a traveling microwave field that propagates in only one direction along the system, exposing process fluids positioned between the conductors. Two concept variants are presented in this chapter to demonstrate the concept of a coaxial traveling microwave reactor (TMR): a liquid phase reactor and a heterogeneous gas-phase catalytic reactor. We show how both reactor concepts can be geometrically optimized to fulfill a specific set of requirements. A two-step approach towards optimization is employed. First, the cross section is optimized, followed by the inner conductor diameter profile in the axial direction in order to bring the axial heating rate distribution in accordance with the specification.

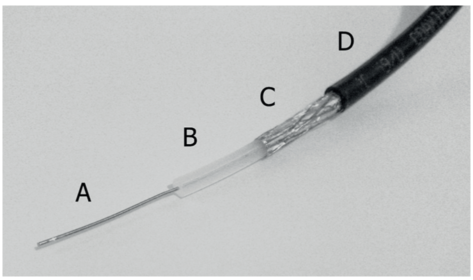

Figure 5.1. RG-59 coaxial cable. It consists of a) an inner conductor, b) a dielectric filler, c) an outer conductor, and d) an outer insulator.

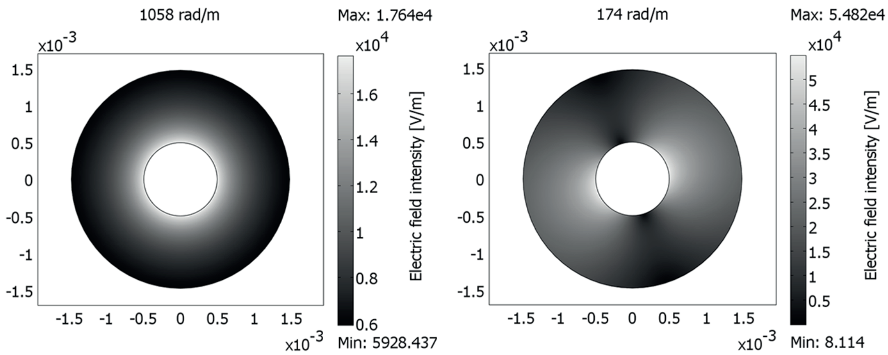

(a) (b)

Figure 5.2. Modal patterns at 1 W of power transmission of the fundamental transverse electromagnetic (TEM) propagation mode (a) and the TE_{11} propagation mode (b) in a RG-141 coaxial cable at a frequency of 35 GHz. The TEM mode propagates at all frequencies, while the TE_{11} mode only propagates above a 34.5 GHz cut-off frequency. The relatively low propagation constant of 174 rad/m indicates that the TE_{11} mode is close to the cut-off condition. It can be seen that for the TEM mode, the field intensity does not fall to zero at the outer conductor and that the intensity distributes uniformly over the circumference. Therefore, an array of channels positioned in the field against the outer conductor will be exposed to uniform field. This is not the case though for the TE_{11} mode.

An important feature of the coaxial TMR is operation below the cut-off frequency of higher order modes. Electromagnetic propagation in waveguides can occur only in an integer number of propagation modes or – colloquially – ways in which the electromagnetic waves propagate. Figure 5.2 presents the cross sectional field distributions of the lowest, fundamental propagation mode and the next higher order propagation mode of a coaxial waveguide. These propagation modes are denoted TEM (Transvers Electric Magnetic) and TE_{11} (Transverse Electric one one) respectively. While the TEM mode can always propagate in a coaxial waveguide, the TE_{11} can only propagate above a certain frequency for a given waveguide. Effectively, the electromagnetic wavelength has to be sufficiently small (or, equivalently, the frequency has to be high enough) for the TE_{11} mode to "fit into" the waveguide, which implies that the TE_{11} mode has a certain (nonzero) cutoff frequency.

5

The concept of TMR requires that it is dimensioned such that only the TEM propagation mode can propagate and that all higher order modes are cut-off. In fact, the tangential non-uniformity observed in the TE_{11} mode in Figure 5.2b is a standing wave pattern, whose avoidance is the primal aim of the TMR concept. Moreover, limiting the propagation modes to only the TEM mode enables predictable microwave fields, because energy can only be distributed over this single-mode.

It is finally remarked here that the electromagnetic field pattern cannot attain a true TEM mode in systems with a non-homogeneous medium distribution between the conductors, so the propagation mode is more correctly referred to as quasi-TEM.

5.2 Liquid phase reactor

For liquid phase processes, microchannels in the filler are cut against the outer conductor. In the concept presented in Figure 5.3, the one-directional microwave field would be present between these conductors. Fluids or reactants that flow in the channels would thus be exposed to and heated by the microwave field. The goal is to achieve a uniform three-dimensional heating rate distribution in the process fluid.

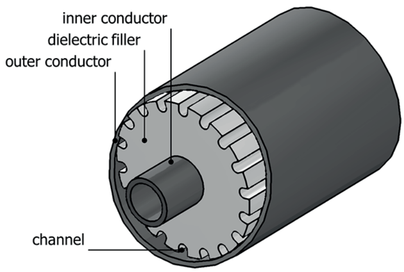

Figure 5.3. Coaxial traveling microwave multichannel liquid phase reactor concept.

As shown in Figure 5.2a, the field intensity in TEM or quasi-TEM distributes uniformly over the circumference of the outer conductor [69]. Heat generation would thus be distributed uniformly among the channels. Note here that the channels can be cooled through the outer conductor surface. Doing so would not expose the coolant to the microwave field. This avoids the need for special coolants that do not absorb microwave energy.

In addition to this, the field distribution can be locally controlled by adjusting the structural parameters of the TMR. In the sections below a two-step optimization approach is demonstrated that aims for the aforementioned uniform microwave field distribution in the process fluid volume. The objectives for the case under consideration are: 1) to achieve a uniform microwave heating rate distribution, 2) in water at 25°C (ε_r = 77 – 9*i* [74]), 3) distributed over 12 channels with a 0.2 mm^2 cross-sectional area and 1.6 m axial length, 4) in a TMR with a 9 mm outer diameter, that is 5) constructed using PTFE (ε_r = 2.2 – 0.0005*i* [65]) as filler material.

5.2.1 Channel cross-section optimization

Figure 5.4 displays a segment of the reactor cross-section that defines the geometrical parameters. For the case discussed herein, two can readily be derived: r_3, the outer conductor radius (half the outer conductor diameter); and α_1, the angle along the segment arc (180° divided by the number of channels). The other parameters are degrees-of-freedom available to the optimization. The first optimization step involves the channel cross-section. The cross section is delimited by a circular arc closest to the inner conductor, and two straight lines on either side of the channel tangent to the arc and running to the outer conductor. The parameters defining the channel cross-section are: the radius of the arc (r_4), the distance of the center of this arc to the center of the inner conductor (r_2) and the angle of the straight line sections relative to a line crossing the center of the inner conductor and the center of the arc section (α_2). In this first optimization step the inner conductor (r_1) radius is chosen arbitrarily and not considered further. The optimization was performed by parameterizing the geometry of the segment in Comsol Multiphysics 3.5 [70] and analyzing the electromagnetic wave propagation by modal analysis with RF-module. Via an optimization routine in Matlab [76] a geometry in terms of r_2, r_4 and α_2 was found that minimizes the heating rate cost function, which was defined as,

$$\textit{cost function} = \frac{\textit{maximum local heating rate}}{\textit{average local heating rate}} \tag{5.1}$$

Figure 5.5 presents the solution found, which minimizes the cost function to 1.147 while maintaining the channel cross-sectional area at 0.2 mm^2; the resulting parameters are r_2 = 4.37 mm, r_4 = 0.282 mm and α_2 = 10.07°.

5

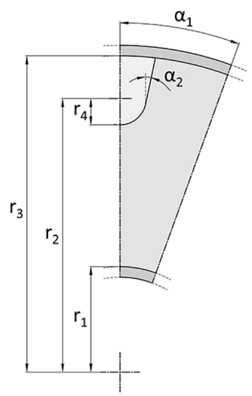

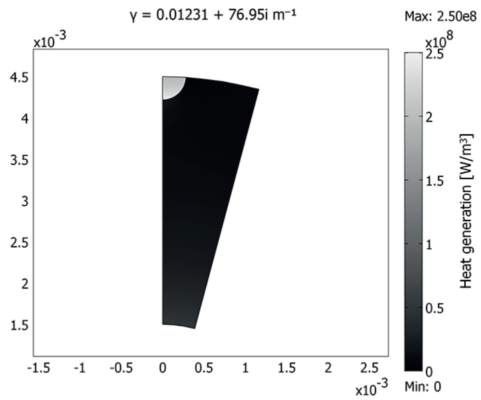

Figure 5.4. Geometrical degrees of freedom in the cross section of the coaxial traveling microwave multichannel liquid phase reactor concept. The radii r_2 and r_4 and the angle α_2 are available for optimization of the channel cross section. The inner conductor radius r_1 can be varied to manipulate the axial distribution of heat generation.

Figure 5.5. Optimized channel geometry with the optimized distribution of the heating rate plotted. The propagation constant for this geometry is $\gamma = 0.01231 + 76.95i\ m^{-1}$.

5.2.2 Optimization of the inner conductor radius

In a second step, the axial heating rate distribution is optimized by manipulating the profile of the inner conductor diameter. If the inner conductor were to be constant over the length of the reactor, the field intensity and heating rate would attenuate exponentially over the length of the reactor. To compensate for this, the inner conductor diameter can be increased along the reactor to gradually press the microwave field more into the channels to compensate the attenuation.

In the example under consideration, the diameter profile is to be optimized for a uniform heating rate distribution along the length of the reactor. To calculate the inner conductor shape, the reactor was discretized into 10 mm elements over which the electromagnetic wave propagation is calculated. Two transmission line parameters are relevant to determine the electromagnetic interactions between the discretization elements: the propagation constant (γ) and characteristic impedance (Z_c). Both depend on the inner conductor radius. The complex valued propagation constant expresses per unit length of a transmission line the number of waves and the wave attenuation. The characteristic impedance is the ratio between the electric potential between the conductors of a transmission line and the electric current flowing through the conductors; the variation in impedance at connections between transmission line sections or – in this case – discretization elements determines the reflections at these connections.

A look-up table for γ was generated by repetitive modal analysis of the geometry in Figure 5.5 while varying r_1. Determining the characteristic impedance is not as straightforward however, because non-TEM waves, like those in the TMR, do not have a uniquely defined voltage and current [69]. Instead, two relations that hold for TEM waves in coaxial waveguides were used to determine a representative characteristic impedance along the reactor. These relations are 1) the equation for the series inductance of coaxial lines,

$$L = \frac{\mu_0}{2\pi} \ln \frac{r_3}{r_1} \tag{5.2}$$

and 2) the relation between characteristic impedance and propagation constant,

$$Z_c = \frac{i2\pi f L}{\gamma} \tag{5.3}$$

Here μ_0 denotes the magnetic permeability of free space and f denotes the frequency of the microwave field. With these relations a look-up table for the characteristic impedance is generated and by using both look-up tables the microwave field distribution and dissipation can be calculated over the TMR. An optimization routine in MATLAB was then used to optimize the inner conductor profile for a uniform dissipation or heat generation along the length of the reactor.

Figure 5.6 presents the solution for the inner conductor diameter profile and Figure 5.7 the axial distribution of heat generation. Note that at the beginning and the end of the reactor-applicator, there are short sections in which the diameter varies more sharply. In these sections, the channels are gradually running into and out of the system; the diameter variation compensates for the effect this has on the impedance to minimize reflections.

To verify whether the distribution of heat generation is indeed uniform over the entire volume of the channel, a three-dimensional simulation of a segment was done using the RF-module of COMSOL Multiphysics 3.5. The simulation results are shown in Figure 5.8. It was found that the greatest variation of ~15% occurs primarily in the cross section rather than in the axial direction. Assuming a limit for the dielectric strength in the reactor-applicator of 1 MV/m, it was found that the maximum microwave inlet power on this system is 13.1 kW. This results in a heat generation per unit volume of 253 MW/m^3, enough to heat water from room temperature to boiling in a few seconds. However it was also found that only 7.4% of the microwave energy is absorbed over the length of the system. Hence for a process involving this TMR it would be required to include microwave circuitry to redirect the microwave energy exiting the reactor back to the input port.

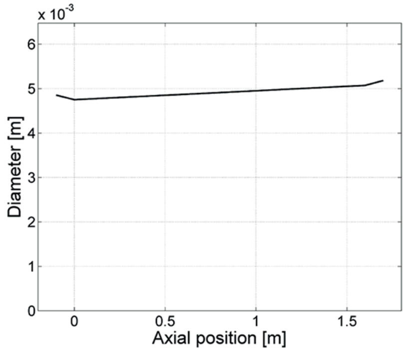

Figure 5.6. Optimized diameter profile over the length of the liquid phase reactor.

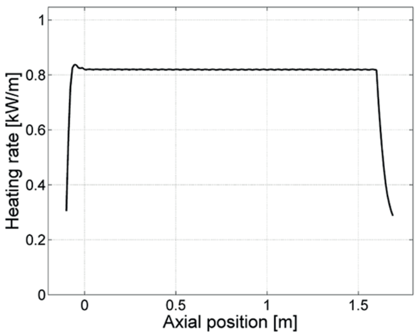

Figure 5.7. Optimized axial heating rate distribution over the length of the liquid phase reactor.

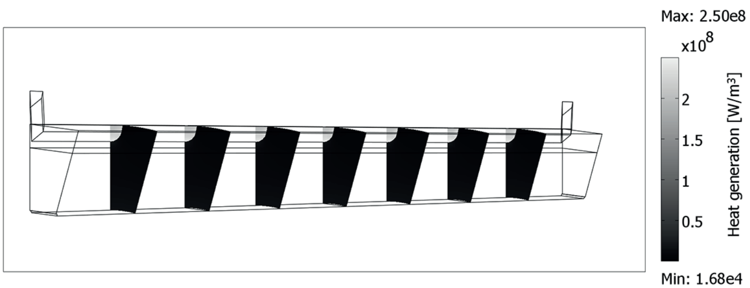

Figure 5.8. Three-dimensional simulation of heating rate in an optimized liquid phase coaxial TMR segment. The slices are spaced 0.2 m apart. Note that this figure has a high degree of perspective distortion, the geometry is only about 2 mm high, while it is 1.6 meter long.

5.3 Gas-solid phase process configuration

The other potential field of application of coaxial traveling microwave reactors presented in this chapter could be processes involving selective heating of catalytic sites in in heterogeneous gas-solid chemistries. As opposed to the liquid phase reactor, now the focus lies in selective catalyst heating. This is, in principle, beneficial not only in terms of energy savings, as inert parts of the reactor are not directly heated, but also in terms of chemical efficiency as undesired side-reactions in the bulk phase may be suppressed. Figure 5.9 presents the concept proposed herein; the space between the inner and outer conductor contains a dielectric material and a monolithic (cordierite/silica) multichannel layer adjacent to the outer conductor. The channels' volume will be occupied by the gas phase. The channel walls transverse to the outer conductor will be functionalized with metal catalyst. Unlike the system for liquid phase processing discussed in the previous section, the goal here is to *focus* the electric field on the metal nanoparticles (selective/direct catalyst heating) in the monolith walls and to attain heating rate uniformity along the axial (flow) direction. The later can be achieved by gradually increasing the radius of the inner conductor, as shown in Figure 5.9, in order to compensate for wave attenuation along the reactor length.

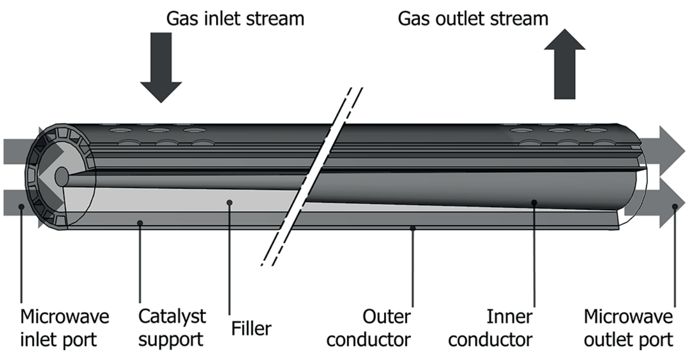

Figure 5.9. Coaxial traveling microwave gas phase monolith reactor concept.

Figures 5.10 and 5.11 are based on a preliminary modeling study of the configuration in Figure 5.9. Figure 5.10 shows the electromagnetic energy dissipation (heat generation) over a cross section of the TMR. Due to the filler material having a higher permittivity compared to the effective permittivity of the outer monolithic layer containing the gas phase, the electric field is "pushed" towards the outer conductor. The densified field in the monolithic layer results in

5

evenly distributed and focused heating of the transverse channel walls as shown in Figure 5.11. The transverse channel walls are functionalized with metal catalyst nanoparticles that have a high dielectric loss factor, thereby selectively absorbing the microwave energy.

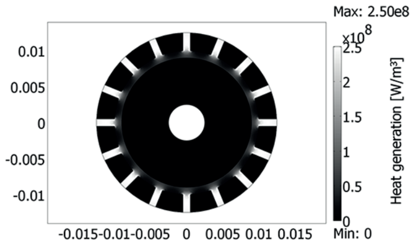

Figure 5.10. Simulation of the heating rate distribution over the cross section of the gas phase monolith reactor. A total cross-sectional heating rate of 12.7 kW/m was simulated in this example.

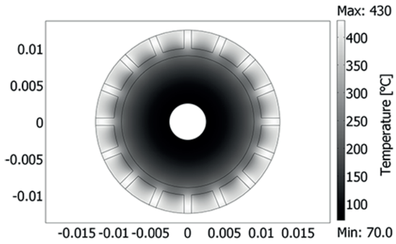

Figure 5.11. Simulation of the temperature distribution over the cross section of the gas phase monolith reactor after 12 s of microwave exposure.

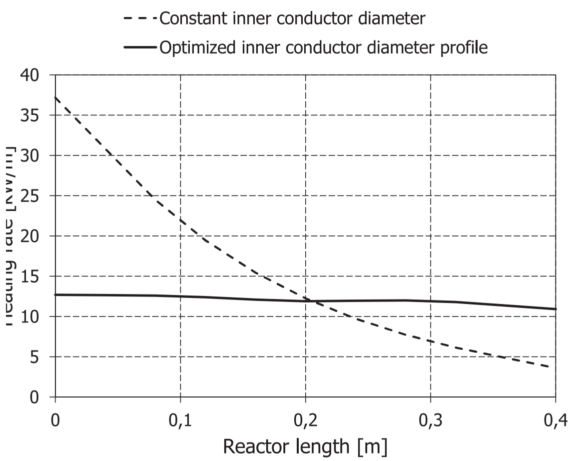

Figure 5.12. Axial heating rate distribution for both the constant inner diameter profile and the inner diameter profile that is optimized for a constant axial heating rate distribution.

Similar to the approach described for the liquid phase system, the inner diameter profile is optimized for a uniform axial distribution of the electromagnetic dissipation. The results for optimized and non-optimized (constant) radius profiles are shown in Figure 5.12. The solid line in the plot corresponds to optimized inner conductor diameter profile and shows that the heating rate along 40 cm length remains almost invariant, although > 70% of the microwave power at the inlet port has been absorbed along the way (not shown).

5.4 Conclusions

In this chapter a novel reactor concept is presented that avoids the resonant field conditions that are associated with microwave cavities. This concept, the Coaxial Traveling Microwave Reactor, merges a multichannel microstructured reactor with a coaxial waveguide. It aims to retain the highly controlled and optimized conditions of microreactors and extend these attributes to the microwave field. Two concept variants are presented: a liquid phase reactor and a gas-solid heterogeneous catalyst reactor. A two-step method of successive optimization of the cross-sectional and the axial geometries was demonstrated to enable control over the spatial distribution of the electromagnetic field and the heat generation. It was shown that a three-dimensional uniform heating rate distribution can be obtained, which is impossible to achieve with resonant microwave fields over any spatial domain that is longer than a small portion of the wavelength.

Thus the TMR may provide a solution to some important issues with respect to microwave chemistry. It permits linear scale-up with no inherent limitation on the length of the reactor and it enables controlled application of microwave energy tailored to specific applications, for example flow-through experimentation with a well-defined microwave field. In addition to this, the arrangements for heat transfer may further facilitate precise study of the microwave-chemical interactions as these can be decoupled from temperature effects in the system.

Chapter 6

Conclusions and Future Outlook

This thesis investigates the application of microwave fields in microreactor systems. In this context, the focus was placed on the electromagnetic aspects in terms of equipment design and prediction, control and optimization of the electromagnetic field. The thesis can be divided in two parts. In the first part, the limitations of commonly used resonant fields in single-mode cavity systems are explored. The introductory chapter already discounts the familiar multimode cavity systems for their usefulness in the above context. Chapter 2 demonstrates limitations due to the non-uniformity of resonant fields. Chapter 3 investigates the practical limitations in commonly applied cavity systems regarding the optimization of the spatial field distribution and the overall heat generation. This exploration was conducted by means of an extended case study with an exemplary and celebrated microwave cavity heating device, the CEM Discover Microwave Synthesis System [88]. The second part of the thesis explores alternative microwave field applicator configurations. In Chapter 4, the potential of cavity systems based on standard sized rectangular waveguide sections is explored. Although the microwave field in such cavities exhibits complex interactions like any resonant field, it is also shown that it is better predictable than the field in more conventional cavity systems, to the extent that the coupling of microwave energy is amenable to optimization by appropriate geometrical manipulations. This is demonstrated for an esterification process in a long residence time continuous flow reactor configuration that this cavity type uniquely supports. Chapter 5 presents a novel applicator configuration that employs traveling microwave fields rather than resonant fields. Via simulation the geometrical optimization of this system is demonstrated to obtain a uniformly distributed heating rate.

The findings have led to new insights regarding the design of equipment for processing with electromagnetic energy as an alternative energy source. Five design principles were formulated, but no design guidelines are yet in sight. The next two sections respectively present the design principles and discuss how design guidelines may be obtained.

The design principles found…

From the previous chapters a number of design principles were extracted that are summarized below with additional clarifications and references to these chapters. These design principles are formulated specifically referring to *electromagnetic fields*, rather than *microwave fields* alone. The microwave spectrum is defined to range from vacuum wavelengths of one meter to one millimeter. There is no reason to assume that the physics of electromagnetic fields in spectra alongside the microwave spectrum deviate considerably from microwave fields, save for their wavelength and frequency. The design principles may thus be extended to the longer wavelength radio frequency fields or to the shorter wavelength terahertz or far infrared fields.

1. Limit the degrees of freedom available to the electromagnetic field in order to improve prediction, control and optimization of electromagnetic fields.

Already in the introductory chapter multimode cavities have been deemed completely unsuitable, since they permit multiple modal patterns to appear simultaneously. Because it is impossible to determine the energy distribution among these modes, the spatial distribution of the electromagnetic field cannot be predicted. A similar effect comes into play in the coaxial traveling microwave reactor concept presented in Chapter 5. If the diameter of that system is made too wide in relation to the wavelength, then an additional propagation mode emerges. This additional degree of freedom available to the electromagnetic field will make it impossible to guarantee that only one specific spatial field distribution can exist in the system.

2. In case a particular *resonant* applicator design is to provide a uniformly distributed electromagnetic field, then the processing volume is constrained to a limited portion of the wavelength of this electromagnetic field. Increasing the processing volume or improving the uniformity requires longer wavelengths or, equally, lower frequencies. In addition to this, the medium properties need to be considered in the analysis, because the wave-length also depends on the dielectric permittivity.

In Chapter 2 the relations between wavelength, equipment size and field uniformity are analyzed for a simple hypothetical resonant electromagnetic field applicator configuration. Although the analysis concerns only two variants of a hypothetical system, it was shown that the relations found can provide a good first estimation of the field distribution in similar, but more complicated and realistic processing systems. Moreover, these results demonstrate a general rule that holds for resonant electromagnetic fields: to obtain a uniform electromagnetic field, the size of a spatial domain cannot exceed a certain portion of the standing wave length, because the standing wave pattern inherently develops non-uniformly given enough space.

3. In order to predict the electromagnetic field interactions, the spatial distribution of all the properties of the media that are involved with the field must be taken into account. This includes the geometries of objects and volumes containing processing fluids, parametrically variable complex dielectric permittivity data of these media, and the orientation of the objects and volumes with respect to the electromagnetic field.

Chapters 3 and 4 both present a study on a particular single-mode microwave cavity applicator system. Chapter 3 presents an extended case study into the CEM Discover Microwave Synthesis System and Chapter 4 presents an exploration into cavity systems based upon standard sized waveguide sections. For both of these systems, experimental data was obtained; furthermore, both systems were simulated and the modeling results were validated against the experimental results. For the system investigated in Chapter 3, qualitative similarities are obtained, and for the system in Chapter 4 quantitative agreement is achieved. Key in attaining these respective levels of agreement is the inclusion of a significant amount of information on the geometries and of complex valued medium properties. In contrast to this, relevant publications in this field of research tend to focus on the dissipative medium properties alone as an explanatory model for observations. That approach does not account for electromagnetic scattering and thereby ignores, for example, the effects of energy losses by the reflection of electromagnetic fields, or the dependence on the field vector orientation of the field strength when an interface between media is crossed. On a more elemental level, one has to consider the size of the wavelength relative to the geometries involved with the electromagnetic field. As was pointed out in Chapter 1 and verified by experimental results in Chapter 3, when the wavelength is of the same order of magnitude as these geometries, wave field physics must be applied in order to attain correct prediction of the spatial distribution of the electromagnetic field.

4. Good prediction and optimization of an electromagnetic field in a field applicator is aided by a plain and well-known applicator geometry and by the avoidance of complex non-linear interactions.

Despite the qualitative agreement between experimental and simulation data, the simulation of Chapter 3 does not nearly achieve the accuracy of the simulation in Chapter 4. Evidently, the system considered in Chapter 4 is much easier to simulate due to the following matters. First, the geometry of the system of Chapter 4 is well-known and geometrically much simpler; the chances of geometrical mismatches occurring are thus considerably reduced. Second, the system of Chapter 3 involves a complex non-linear interaction with a magnetron microwave source. To obtain an accurate simulation, much information on this microwave circuit element would be required as well as additional solving routines to deal with the non-linearities. On the contrary, the system of Chapter 4 employs both an isolator and a matching circuit; both these provisions by themselves can eliminate backward interactions with the microwave source. Moreover, there is an additional advantage to the system of Chapter 4: the microwave field in it is amenable to two-dimensional analysis, rather than three-dimensional. This results in much faster computation and reduced demands on computational hardware. Furthermore, it conveniently facilitates the inclusion of the simulation into an optimization routine. The same computational advantages were exploited in the analysis of the Coaxial Traveling Microwave Reactor described in Chapter 5 to demonstrate the last design principle listed here:

5. Using a *traveling electromagnetic wave field* rather than a resonant field enables a higher degree of control over the spatial distribution of the electromagnetic field and permits larger processing volumes.

Whereas the first four chapters of this dissertation report on the limitations of resonant applicator cavities, Chapter 5 presents a novel reactor concept that avoids resonant electromagnetic fields altogether. This concept, the Coaxial Traveling Microwave Reactor, merges a multichannel microstructured reactor with a coaxial waveguide. Two concept variants are presented. First, a simulation of a liquid phase reactor demonstrates how a three-dimensional uniform heating rate distribution can be obtained by means of successive optimization of the cross-sectional and the axial geometries. Second, a gas-phase solid catalyst reactor variant indicates the possibilities to shape and focus the electromagnetic field in the cross-sectional plane by an appropriate spatial distribution of dielectric medium parameters. For both variants, the dimensions of the cross-sectional plane are chosen too confined to support anything but one favorable, tangentially uniform field pattern. Further, the electromagnetic field is made to travel in only one direction in the axial dimension. This results in the absence of an axial standing wave pattern, which would be inherently non-uniform over any distance that exceeds a small portion of the wavelength. The latter condition permits axial scaling far beyond the constraints that hold for resonant fields.

… though no design guidelines yet

Although the design principles presented in the previous section may help to design process systems with electromagnetic activation, it is still too early to make any clear-cut statements as to what type of equipment may serve a particular process best. What is lacking is a knowledge base of conceptual options to merge chemical processing and electromagnetics in one system. Although, the set of novel concepts presented in this thesis might work for some processes, this set by itself is still small and does not leave much to choose from. A more extensive set of options would be much desired and, in fact, several additional options already exist.

One of them is the range of integrated reactor and microwave transmission systems, under the generic name Labotron [108] by Sairem SAS, which is especially designed to carry out batch or continuous flow microwave-assisted synthesis and extraction processes. This range of products employs an internal transmission line to effectively introduce energy into the processing volume. Another relevant example is radio frequency heating, which uses electromagnetic fields of much lower frequencies and electrode applicator systems [75]. Radio frequency heating is widely applied in industry; a few examples of its applications are: adhesive heating in wood gluing presses, heat treatment of steel and welding of plastics. Because of the longer wavelengths, standing wave patterns would take much more space to emerge in and therefore these are less of an issue. Additionally, there is much potential to manipulate the electromagnetic field via shaping of the electrodes, but due to the lower frequency, the heating rate is more limited. Nevertheless, this form of energy has already been investigated by Izadifar et al. [109] in a packed-bed extraction process.

What these examples illustrate is that the options for the application of electromagnetic fields in chemical processes are much more numerous than they may appear at first glance; the systems that are presented above and in the previous chapters are far from a complete overview of possible technologies. There remains a huge domain to explore. This is expressed by table 6.1, a classification matrix of possible technologies. It crosses the electromagnetic field applicator systems presented above and in previous chapters with a number of process systems. Each cell of this matrix represents a separate conceptual combinational system of a process system with an applicator one. Note that neither the set of applicator systems nor the set of process systems in the table form a complete overview of possibilities. More specifically, the dashed line sections of the table indicate that it may be stretched beyond its current scope. Thus, the table may represent the entire domain of electromagnetically activated process systems.

Table 6.1. Classification matrix of combined electromagnetic and process systems.

		Process systems				
		CSTR	**Packed bed**	**Open channel**	**Multichannel (scale-out)**	**Membrane**
Electromagnetic applicator systems	Multimode					
	CEM Discover					
	TE_{10n}			Chapter 4	Chapter 4	
	Coaxial TMR				Chapter 5	
	Labotron	[108]		[108]		
	Electrode		[109]			

Within this domain two things are apparent. First, the number of potential combinational systems is very large. Second, aside from the top two rows (gray) that make up the volume of work done on microwave processing in "traditional" cavity systems, the matrix is largely empty. At his moment, only a limited number of cells in the third and lower rows contain a reference to a particular combinational processing-and-electromagnetics system, these either refer to a chapter in this thesis or to another publication. Other potential options that could be explored are, for example, to uniformly activate a reaction in (small) packed bed by means of a TE_{10n} cavity, or to apply a membrane in the outer conductor of a TMR so it facilitates both heat transfer and selective mass transfer. References on the latter two examples do not yet exist however, and therefore the respective cells in the table currently remain empty. Nevertheless, the establishment of design guidelines for process systems with electromagnetic activation would require this matrix to be filled in further. Not with the purpose to fully complete it, but to have a knowledge base to which designers may refer in the development of such systems. It is hoped that this could provide a framework for future study.

A major challenge in this stems from the lack of overlap between the respective engineering disciplines that are involved. On the one hand, process engineering traditionally does not deal with the physics of wave interactions or electromagnetic fields, while on the other hand, electronics engineering and microwave engineering do not consider molecular interactions. To address this, a common language could be developed by exploring the conceptual options and by evaluating them both on criteria pertaining to process engineering and to criteria pertaining to electromagnetics. More specifically, aside from factors that relate directly to process engineering, namely yield, selectivity and efficiency, a number of additional criteria may be considered. This thesis mentions in this respect: the predictability and control of the electromagnetic field with specific consideration to these in the spatial domain; special material requirements, e.g. electromagnetically non-dissipative coolants; and existing industrial or practical expertise with particular types of systems.

An additional dimension that can be added to this framework is the frequency or – equally – wavelength of the electromagnetic field. Considerations regarding frequency are twofold. On the one hand, within practical limitations and setting aside changes in medium properties that may occur under frequency variation, as long as system geometries are scaled to the same ratio as wavelengths then findings at a particular frequency also hold at other frequencies. For example, when a particular lab-scale microwave processing system that was optimized for a particular frequency is to be scaled up, then scaling both geometry and wavelength to the same factor will result in a scaled system with either a very similar one or with the same electromagnetic field distribution. On the other hand, it may well be that processes benefit only from specific, possibly narrow, frequency bands. In other words, process benefits may be frequency specific. It would therefore seem opportune not only to correlate process performance with the occurrence or intensity of a radio frequency or microwave field, but with the exact frequency of that field too. It would be difficult at present to judge the outcome of explorations in the frequency domain, since – to the best of our knowledge – all relevant studies have been conducted at one frequency only, mostly in the conveniently available 2.45 GHz band. If frequency dependent interactions could be evinced, then this may lead to new ways of controlling chemical processes, although the instruments that would be needed for such investigations are currently non-existent. The first major – and possibly prohibitive – challenge in such studies would be to develop the required equipment.

The latter remark essentially holds for all activities in the context of applying electromagnetic fields in chemical processes; besides developing the electromagnetically enhanced processes, a parallel development track is needed for the equipment, the instrumentations, and the integrated processing-and-electromagnetics systems. As this thesis has a strong focus on the equipment side of the matter, it is hoped that it may give some directions to subsequent investigations that concentrate on the processing aspects. Eventually, parallel growth of the knowledge base may lead to a detailed set of design guidelines and, ultimately, future chemical processing plants.

Appendix A

Analysis of a concentric cavity configuration

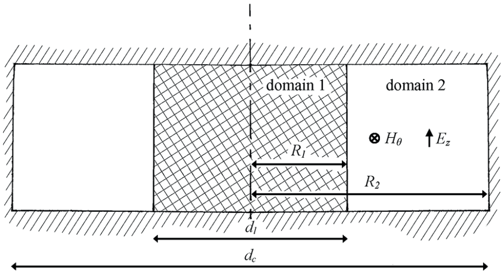

Figure A.1. Concentric configuration with a cylindrical load in a cylindrical cavity.

For the concentric heating cavity configuration in Figure A.1 an analytic solution is determined for resonance in its fundamental resonance mode TM_{010}. By expressing the problem in cylindrical coordinates and by accounting for the invariance of this mode in both axial and tangential direction [69], the problem reduces to a one-dimensional problem in the radial direction. The two relevant electromagnetic field vectors components are the electric field in the axial direction (E_z) and the magnetic field in the tangential direction (H_θ). For these variables, analytic functions were determined with respect to the radius (r). There are two concentric domains: the inner domain ($0 \leq r \leq R_1$), which is the homogeneous load; and the outer domain ($R_1 < r \leq R_2$), which consists of the empty space in the cavity. Heating uniformity is defined as the ratio of minimum to maximum heat generation rate in the load, which in under the aforementioned conditions can be reduced to the square of the ratio of the electric field at $r = R_1$ to the electric field at $r = 0$,

$$HU = \frac{q_{load,\min}}{q_{load,\max}} = \frac{\left(\frac{1}{2}\omega\varepsilon''\varepsilon_0 \left|E_z(r)\right|^2\right)_{load,\min}}{\left(\frac{1}{2}\omega\varepsilon''\varepsilon_0 \left|E_z(r)\right|^2\right)_{load,\max}} = \left(\frac{E_z(R_1)}{E_z(0)}\right)^2 \tag{A.1}$$

The following boundary and continuity conditions occur [69]:

1. At $r = 0$, $E_z(r)$ is bounded, i.e. it may not become infinite.
2. At $r = R_2$, $E_z(r)$ is zero because electromagnetic boundary conditions do not allow a parallel electric field at an electrically conducting surface.
3. At $r = R_1$, $E_z(r)$ and H_θ (r) are continuous over the interface between the load (domain 1) and the empty cavity (domain 2).

Expressing Maxwell's electromagnetic field equations for $E_z(r)$ and $H_\theta(r)$ in the frequency domain in cylindrical coordinates gives,

$$r^{-1}\partial_r(rH_\theta(r)) - i2\pi f\varepsilon E_z(r) = 0 \tag{A.2}$$

$$-\partial_r E_z(r) + i2\pi f\mu H_\theta(r) = 0 \tag{A.3}$$

Rearranging and substituting Eq. A.3 into Eq. A.2 to eliminate $H_\theta(r)$ yields the zeroth-order Bessel equation.

$$r^2\partial_r^{\,2}E_z(r) + r\partial_r E_z(r) + r^2 4\pi^2 f^2 \varepsilon\mu E_z(r) = 0 \tag{A.4}$$

It follows that a general solution for the modal pattern is a combination of Bessel functions of the first and the second kind, as shown below, where m is the domain index,

$$E_z(r) = A_m J_0\left(r2\pi f\sqrt{\varepsilon_m\mu_m}\right) + B_m Y_0\left(r2\pi f\sqrt{\varepsilon_m\mu_m}\right) \tag{A.5}$$

At $r = 0$ the first boundary condition requires that $E_z(r)$ is bounded, therefore in the domain of the load it follows that $B_1 = 0$. The solution of the modal pattern is normalized with the conditions that $E_z(0) = 1$ and – consequently – $A_1 = 1$. Further, a frequency f is imposed. From Eq. A.3 and Eq. A.5 it follows, that the solutions for the electromagnetic field components in the domain $0 \le r \le R_1$ are,

$$E_z(r) = J_0\left(r2\pi f\sqrt{\varepsilon_1\mu_1}\right) \tag{A.6}$$

$$H_\theta(r) = i\sqrt{\frac{\varepsilon_1}{\mu_1}}\, J_1\left(r2\pi f\sqrt{\varepsilon_1\mu_1}\right) \tag{A.7}$$

These fields are parallel to the interface between domains 1 and 2, therefore the electromagnetic field vectors considered here are continuous over this interface. The constants A_2 and B_2 of the electromagnetic field in domain 2 are solved from the set of linear equations that express the continuity over the interface,

$$\begin{gathered} E_z\left(r\uparrow R_1\right) = E_z\left(r\downarrow R_1\right) \\ J_0\left(R_1 2\pi f\sqrt{\varepsilon_1\mu_1}\right) = A_2 J_0\left(R_1 2\pi f\sqrt{\varepsilon_2\mu_2}\right) + B_2 Y_0\left(R_1 2\pi f\sqrt{\varepsilon_2\mu_2}\right) \end{gathered} \tag{A.8}$$

$$H_\theta\left(r\uparrow R_1\right) = H_\theta\left(r\downarrow R_1\right)$$
$$\sqrt{\frac{\varepsilon_1}{\mu_1}}\, J_1\left(R_1 2\pi f\sqrt{\varepsilon_1\mu_1}\right) = \sqrt{\frac{\varepsilon_2}{\mu_2}}\, \left[A_2 J_1(R_1 2\pi f\sqrt{\varepsilon_2\mu_2}) + B_2 Y_1\left(R_1 2\pi f\sqrt{\varepsilon_2\mu_2}\right)\right] \tag{A.9}$$

The cavity radius R_2 is the first root of the solution for the electric field in domain 2, which is the radius where the 2nd boundary condition is met,

$$E_z(R_2) = A_2 J_0\left(R_2 2\pi f\sqrt{\varepsilon_2\mu_2}\right) + B_2 Y_0\left(R_2 2\pi f\sqrt{\varepsilon_2\mu_2}\right) \tag{A.10}$$

The relations found here were implemented in MATLAB [76] to draw a chart that relates the variables (R_1, R_2, ε_1, f and HU) in the configuration of Figure A.1. The constants ε_2, μ_1 and μ_2 take free space values in this analysis.

As a final remark, it is noted that from Eq. A.6 a function for heating uniformity with respect to f, R_1 and ε_1 can be derived. It was found that this is the same relation as for a cylindrical dielectric load heated by radio frequency heating between two circular electrodes [75].

$$HU = \left|\frac{E_z(R_1)}{E_z(0)}\right|^2 = J_0^2\left(R_1 2\pi f\sqrt{\varepsilon_1\mu_1}\right) \tag{A.11}$$

Appendix B

Spatial discretization and modal analysis of a simple rectangular cavity with a cylindrical load

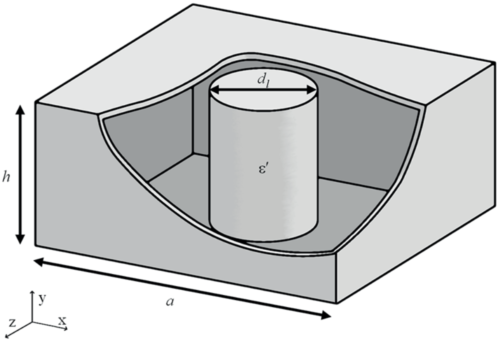

Figure B.1. The cavity configuration under consideration. It is a rectangular cavity with a square base and a cylindrical dielectric load centered inside it. Note that the coordinate system has the y-axis in the height direction, as opposed to that in Figure B.2.

For the cavity configuration in Figure B.1 it has been investigated what the maximum height constraint on the cavity would be in order to only have single-mode TE_{101} operation. This limit is the height (*h*) at which the resonance frequency of the second mode has a value that is 1.2 times that of the fundamental mode. For this purpose a three-dimensional finite difference model is used that spatially discretizes Maxwell's electromagnetic field equations. The values of the resonance frequencies of this model are found by eigenvalue analysis of this model.

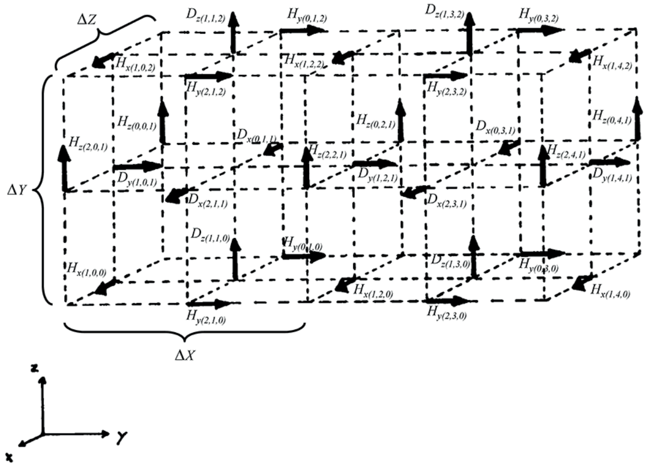

Figure B.2. Two cells of a staggered Yee space lattice.

The Maxwell's curl equations are modeled in a staggered Yee space lattice [78–79]. Figure B.2 shows two 2×2×2 cells of the staggered grid. Material properties are imposed per cell. Magnetic field strength (**H**) and electric flux density (**D**) are used as state variables in the model because the relevant components are continuous over the interface between two unity cells [69]. The curl equations considered here are,

$$\partial_t \mathbf{H} = -\frac{c_0^{\,2}}{\varepsilon'_{eff}} \nabla \times \mathbf{D} \tag{B.1}$$

$$\partial_t \mathbf{D} = \nabla \times \mathbf{D} \tag{B.2}$$

The time derivative of the magnetic field strength vector is calculated from the electric displacement current by employing an effective permittivity for the interface between two unit cells:

$$\varepsilon'_{eff} = \frac{2\varepsilon'_1\,\varepsilon'_2}{\varepsilon'_1 + \varepsilon'_2} \tag{B.3}$$

The electric conduction boundary condition at the cavity walls is modeled by simply imposing that the field variables lying outside the space lattice are zero. The system equations for the space discretization in figure B.2 are:

$$\partial_t H_{x(n_x,n_y,n_z)} = -\frac{c_0^{\,2}}{\Delta Y}\left(\frac{D_{z(n_x,n_y+1,n_z)}}{\varepsilon'_{eff(n_x,n_y+1,n_z)}} - \frac{D_{z(n_x,n_y-1,n_z)}}{\varepsilon'_{eff(n_x,n_y-1n_z)}}\right) + \frac{c_0^{\,2}}{\Delta Z}\left(\frac{D_{y(n_x,n_y,n_z+1)}}{\varepsilon'_{eff(n_x,n_y,n_z+1)}} - \frac{D_{y(n_x,n_y,n_z-1)}}{\varepsilon'_{eff(n_x,n_y,n_z-1)}}\right) \tag{B.4}$$

$$\partial_t H_{y(n_x,n_y,n_z)} = -\frac{c_0^{\,2}}{\Delta Z}\left(\frac{D_{x(n_x,n_y,n_z+1)}}{\varepsilon'_{eff(n_x,n_y,n_z+1)}} - \frac{D_{x(n_x,n_y,n_z-1)}}{\varepsilon'_{eff(n_x,n_y,n_z-1)}}\right) + \frac{c_0^{\,2}}{\Delta X}\left(\frac{D_{z(n_x+1,n_y,n_z)}}{\varepsilon'_{eff(n_x+1,n_y,n_z)}} - \frac{D_{z(n_x-1,n_y,n_z)}}{\varepsilon'_{eff(n_x-1,n_y,n_z)}}\right) \tag{B.5}$$

$$\partial_t H_{y(n_x,n_y,n_z)} = -\frac{c_0^{\,2}}{\Delta X}\left(\frac{D_{y(n_x+1,n_y,n_z)}}{\varepsilon'_{eff(n_x+1,n_y,n_z)}} - \frac{D_{y(n_x-1,n_y,n_z)}}{\varepsilon'_{eff(n_x-1,n_y,n_z)}}\right) + \frac{c_0^{\,2}}{\Delta Y}\left(\frac{D_{x(n_x,n_y+1,n_z)}}{\varepsilon'_{eff(n_x,n_y+1,n_z)}} - \frac{D_{x(n_x,n_y-1,n_z)}}{\varepsilon'_{eff(n_x,n_y-1,n_z)}}\right) \tag{B.6}$$

$$\partial_t D_{x(n_x,n_y,n_z)} = \frac{H_{z(n_x,n_y+1,n_z)} - H_{z(n_x,n_y-1,n_z)}}{\Delta Y} - \frac{H_{y(n_x,n_y,n_z+1)} - H_{y(n_x,n_y,n_z-1)}}{\Delta Z} \tag{B.7}$$

$$\partial_t D_{y(n_x,n_y,n_z)} = \frac{H_{x(n_x,n_y,n_z+1)} - H_{x(n_x,n_y,n_z-1)}}{\Delta Z} - \frac{H_{z(n_x+1,n_y,n_z)} - H_{z(n_x-1,n_y,n_z)}}{\Delta X} \tag{B.8}$$

$$\partial_t D_{z(n_x,n_y,n_z)} = \frac{H_{y(n_x+1,n_y,n_z)} - H_{y(n_x-1,n_y,n_z)}}{\Delta X} - \frac{H_{x(n_x,n_y+1,n_z)} - H_{x(n_x,n_y-1,n_z)}}{\Delta Y} \tag{B.9}$$

These relations yield two system matrices $\mathbf{A}_1$ and $\mathbf{A}_2$ for the electromagnetic field in the cavity:

$$\begin{bmatrix} \partial_t \mathbf{H} \\ \partial_t \mathbf{D} \end{bmatrix} = \begin{bmatrix} & \mathbf{A}_1 \\ \mathbf{A}_2 & \end{bmatrix} \begin{bmatrix} \mathbf{H} \\ \mathbf{D} \end{bmatrix} \tag{B.10}$$

By multiplying the system matrices, the wave equation for the electric flux density in the discretized cavity is found:

$$\partial_t^2 \mathbf{D} = \mathbf{AD}, \text{ where } \mathbf{A} = \mathbf{A}_2 \mathbf{A}_1 \tag{B.11}$$

Eigenvalue analysis yields a set of eigenvalues near zero and a set of eigenvalues on the negative real axis [110]. The former set is due to the non-divergence free boundary condition and is ignored. The latter set of eigenvalues is the set of resonance frequencies of the system.

The relations are implemented in Matlab to find the resonance frequencies of the configuration in Figure B.1 for the system parameters a, d_l, ε' and h. A grid of 10×10×10 cells was used to determine the relevant resonance frequencies. An optimization routine was then employed to find isolines in a contour plot of a / λ_r versus d_l / λ_r for the ratio h / a. On these isolines the fundamental resonance mode is TE_{101} and the second resonance frequency has 1.2 times the value of the resonance frequency associated with the TE_{101} mode.

Appendix C

Electromagnetic interactions with a dielectric layer

While the interactions of a microwave field in realistic systems can be complex, much of the behavior that they exhibit occurs in very simple systems as well. To interpret several observations made from heating processes in the CEM Discover [88] as described in the main body of the text, a simple one-dimensional system is analyzed here. This configuration consists of a dielectric layer of thickness L and relative permittivity ε_2, which separates two domains that have relative permittivities of ε_1 and ε_3, respectively (Figure C.1). The magnetic permeability in all media is that of vacuum. From the ε_1-domain, an electromagnetic wave is perpendicularly incident upon the layer; the electric and the magnetic field vectors of this wave are perpendicular to the direction of propagation.

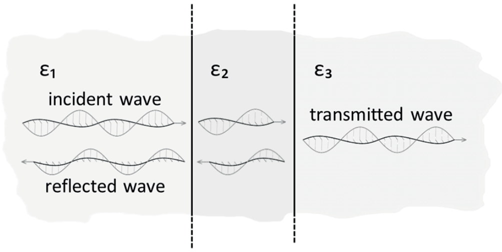

Figure C.1. Configuration of the electromagnetic problem under consideration.

This is a textbook problem and the solution for the reflected wave is readily adapted from typical transmission line problems [69]. The solution is found in terms of the reflection coefficient (Γ). This is the complex ratio of the reflected wave to the incident wave; the magnitude of Γ is the ratio between electric field amplitudes; and the argument of Γ is the phase delay between the incident and reflected field. The reflection coefficient at the interface between the ε_1-domain and the ε_2-layer is,

$$\Gamma = \frac{\dfrac{\eta_3 + i\eta_2 \tan(-i\gamma_2 L)}{\eta_2 + i\eta_3 \tan(-i\gamma_2 L)} - \dfrac{\eta_1}{\eta_2}}{\dfrac{\eta_3 + i\eta_2 \tan(-i\gamma_2 L)}{\eta_2 + i\eta_3 \tan(-i\gamma_2 L)} + \dfrac{\eta_1}{\eta_2}} \tag{C.1}$$

where,

$$\eta_n = \sqrt{\frac{\mu_0}{\varepsilon_0 \varepsilon_n}} \tag{C.2}$$

is the medium impedance of medium n. The impedance is the ratio of the electric to the magnetic field components of an electromagnetic wave. The term,

$$\gamma_2 = \frac{i2\pi f\sqrt{\varepsilon_2}}{c_0} \tag{C.3}$$

is the propagation constant of the electromagnetic wave in the ε_2-layer. This constant is a complex variable: the real part is the attenuation (loss) coefficient of the wave when it travels through a medium (in 1/m); and the imaginary part is 2π times the number of waves per unit length (in rad/m). The symbols μ_0 and ε_0 indicate the magnetic permeability and electric permittivity of vacuum; c_0 is the speed of light in vacuum; and f is the frequency of the electromagnetic field.

One-dimensional absorbing resonator

Heating cavities can be interpreted via an equivalent one-dimensional absorbing resonator configuration. In such a configuration, the ε_3-domain is a conductive metal with a medium impedance of zero, and the ε_2-layer consists of an absorbing medium so the permittivity has an imaginary loss term ($\varepsilon_2 = \varepsilon_2' - i\varepsilon_2''$). The ε_1-domain has vacuum permittivity, $\varepsilon_1 = 1$. The wave incident from the ε_1-domain is at the $\varepsilon_1/\varepsilon_2$-interface partially reflected and partially transmitted into the ε_2-layer. The latter part travels through the layer, being partially absorbed, until it reaches the metal surface. There it is completely reflected and it travels back through the layer, again being partly absorbed, until it reaches the $\varepsilon_1/\varepsilon_2$-interface where it is partially reflected and partially transmitted once more. The forward and backward traveling waves in both domains form an interfering resonant wave pattern.

The absorbed power fraction ($1 - |\Gamma|^2$) is calculated using Eq. C.1 for a layer thickness ranging from 0 to 0.025 m and for four different material properties of the layer: $\varepsilon_2 = 20 - 2i$; $\varepsilon_2 = 20 - 5i$; $\varepsilon_2 = 50 - 2i$; and $\varepsilon_2 = 50 - 5i$ at a frequency of 2.45 GHz. Figure C.2 presents the absorbed power fraction versus L for each set of medium properties; the lines in this graph exhibit a fluctuating pattern of peaks and dips. It appears that the location of the absorption peaks is mainly related to the real relative permittivity; away from of these peaks, the absorption generally increases with the imaginary relative permittivity, but in or near the peaks this is not necessarily the case. A decibel plot of the reflected power (Figure C.3) shows a particularly deep reduction in reflected power at $L = 0.0205$ m for the layer permittivity of $\varepsilon_2 = 20 - 2i$. The reflected power reduces to nearly – 35 dB, which corresponds to a power reflection of only about 0.03%, the remainder is dissipated in the layer.

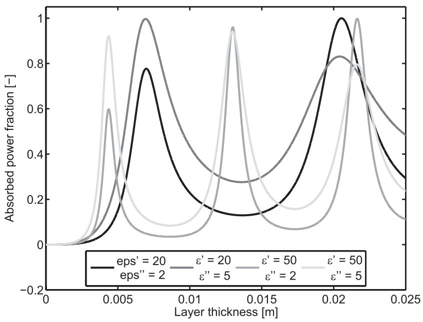

Figure C.2. Absorbed power in the ε_2-layer versus layer length (L), for a variety of relative permittivities of the layer. The frequency is 2.45 GHz; for $\varepsilon_2' = 20$, the wavelength of the microwave field is 27.4 mm, and for $\varepsilon_2' = 50$, the wavelength is 17.3 mm in the ε_2-layer.

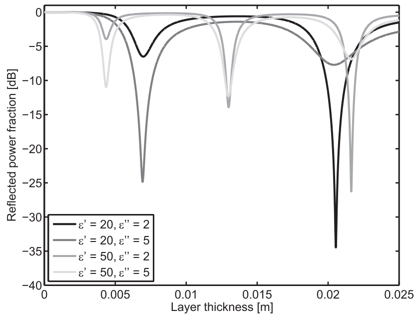

Figure C.3. Decibel plot of the reflected power fraction from the ε_2-layer versus layer length (L) for a variety of relative permittivities of the layer. The frequency is 2.45 GHz; for $\varepsilon' = 20$, the wavelength of the microwave field is 27.4 mm, and for $\varepsilon' = 50$, the wavelength is 17.3 mm in the ε_2-layer.

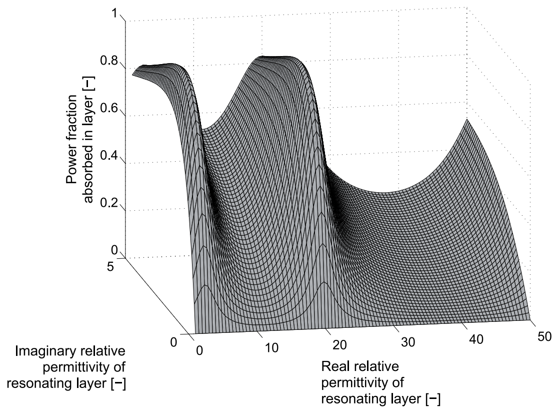

Figure C.4. Absorbed power fraction versus layer material properties. For $L = 0.0205$ m, ε_2' is varied from 1 to 50 and ε_2'' is varied from 0 to 5. The frequency is 2.45 GHz and the wavelength of the microwave field in the ε_2-layer varies from 122.4 mm at $\varepsilon_2' = 1$ to 17.3 mm at $\varepsilon_2' = 50$.

For the layer thickness that gave the highest absorption, L = 0.0205 m, the effect of the layer medium properties is calculated. Figure C.4 presents a surface plot of the absorbed power fraction versus the real relative permittivity (ε_2'), ranging from 1 to 50, and the imaginary relative permittivity (ε_2''), ranging from 0 to 5. The surface shows ridges of high absorption that coincide with particular values for ε_2'. These ridges first rise with increasing ε_2'' and then drop; there is an optimum ε_2'' for which the absorption is highest. Note that the absorption does not necessarily increase with increasing dielectric loss factor ε_2'', but rather a pattern of interconnectedness between the parameters emerges; the effect of a variation in one parameter depends on another parameter.

Anti-reflective layer

The configuration in Figure C.1 can also resemble an anti-reflective layer, which for example can be found on optical lenses. If a microwave field propagates from the ε_1-domain to the ε_3-domain, with both domains consisting of lossless dielectric media, the reflected power fraction ($|\Gamma|^2$) is zero if [69],

$$\varepsilon_2 = \sqrt{\varepsilon_1 \varepsilon_3} \tag{C.4}$$

and,

$$L = \frac{\pi}{-i2\gamma_2} \tag{C.5}$$

These are the conditions for a quarter wave transformer in a microwave network. In case f = 2.45 GHz, ε_1 = 1 and ε_3 = 10, it follows that there is no reflection if ε_2 = 3.1623 and L = 0.0172 m.

Figure C.5 presents a surface plot of the reflected power fraction versus L and ε_2 at this frequency, where L ranges from 0 to 0.024 m and ε_2 ranges from 1 to 10. The plot shows that in case the layer is absent (L = 0 m, ε_2 = 1 or ε_2 = 10) the reflected power fraction is 0.27; also it shows that there is no reflection for the quarter wave transformer conditions. Furthermore, the graph shows that the presence of a layer of intermediate permittivity always reduces the reflection between the two domains, even if the conditions are non-optimal.

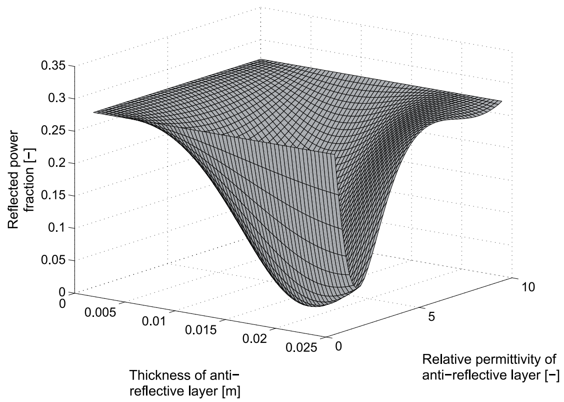

Figure C.5. Reflected power fraction over a dielectric layer between two domains that have respective relative permittivities of 1 and 10. The frequency is 2.45 GHz.

Appendix D

Experimental results for vials heated in the CEM Discover

Chapter 3 presents for only four vials the heat generation versus temperature graphs that are derived from the heating experiments with the CEM Discover. In this appendix, the graphs for the entire set of vials is presented. Each graph presents a set of data points that were determined experimentally and a continuous piece-wise linear curve that was fitted to the data point. The captions list the standard deviation (σ) between the curve and the data points, and the average heat generation over the data points (A) (See Figures D.1–D.15).

The behavior of the heating process differs among the vials. This is apparent from the shapes of the sets of data points and the curves, from the average heat generation, and from the standard deviation. Some of the sets of data points follow a clear trend and allow for a closely fitting curve (e.g. the 27 mm inner diameter vial, Figure D.15), while other sets do not support a closely fitting curve (e.g. the 21 mm inner diameter vial, Figure D.11).

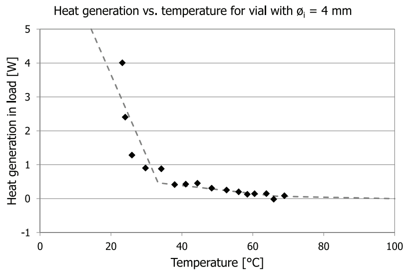

Figure D.1. Heat generation vs. temperature in the vial with the 4 mm inner diameter, A = 0.75 W, σ = 0.41 W, σ/A = 0.54.

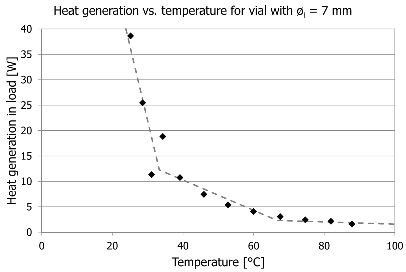

Figure D.2. Heat generation vs. temperature in the vial with the 7 mm inner diameter vial, A = 11 W, σ = 3.1 W, σ/A = 0.28.

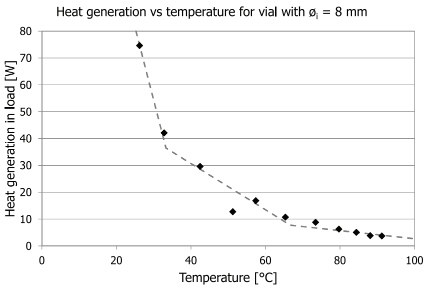

Figure D.3. Heat generation vs. temperature in the vial with the 8 mm inner diameter, A = 19 W, σ = 2.8 W, σ/A = 0.14.

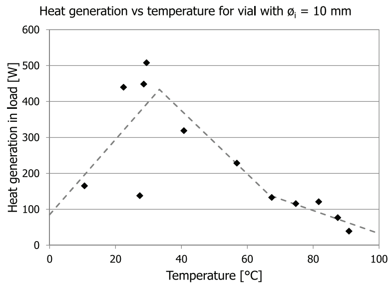

Figure D.4. Heat generation vs. temperature in the vial with the 10 mm inner diameter, A = 227 W, σ = 87 W, σ/A = 0.38.

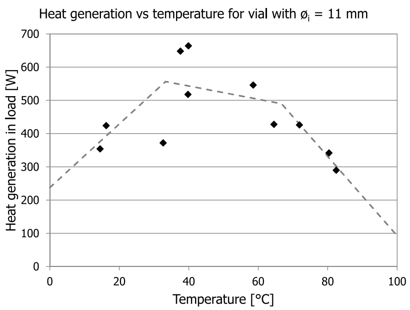

Figure D.5. Heat generation vs. temperature in the vial with the 11 mm inner diameter, A = 456 W, σ = 77 W, σ/A = 0.17.

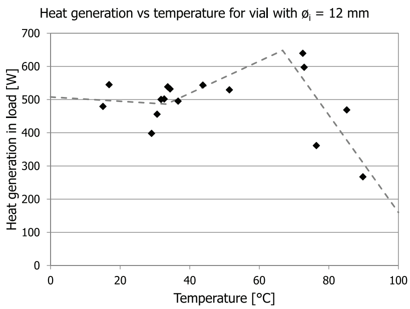

Figure D.6. Heat generation vs. temperature in the vial with the 12 mm inner diameter, A = 491 W, σ = 60 W, σ/A = 0.12.

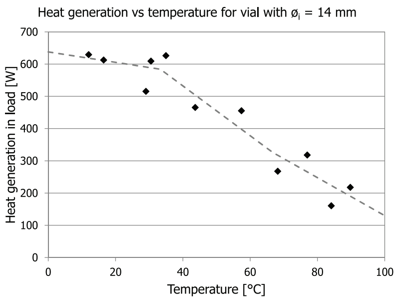

Figure D.7. Heat generation vs. temperature in the vial with the 14 mm inner diameter, A = 444 W, σ = 47 W, σ/A = 0.11.

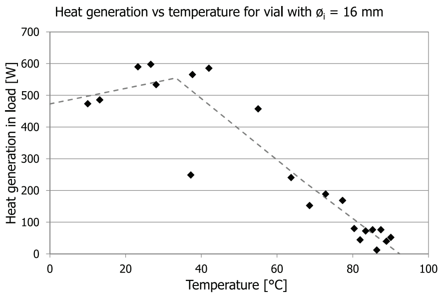

Figure D.8. Heat generation vs. temperature in the vial with the 16 mm inner diameter, A = 273 W, σ = 76 W, σ/A = 0.28. These numbers are affected by the outlier at 37°C/249 W however. Without the outlier the values are, A = 275 W, σ = 37 W,σ/A = 0.14.

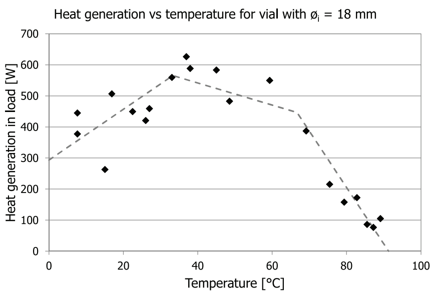

Figure D.9. Heat generation vs. temperature in the vial with the 18 mm inner diameter, A = 376 W, σ = 63 W, σ/A = 0.17.

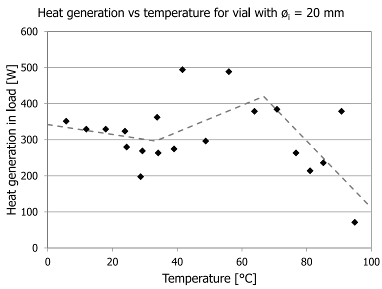

Figure D.10. Heat generation vs. temperature in the vial with the 20 mm inner diameter, A = 309 W, σ = 76 W, σ/A = 0.25.

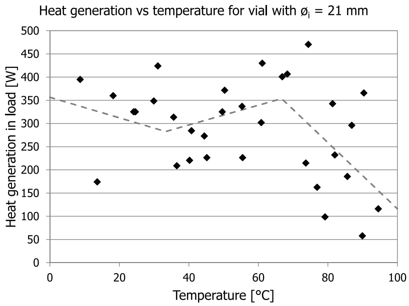

Figure D.11. Heat generation vs. temperature in the vial with the 21 mm inner diameter, A = 288 W, σ = 88 W, σ/A = 0.31.

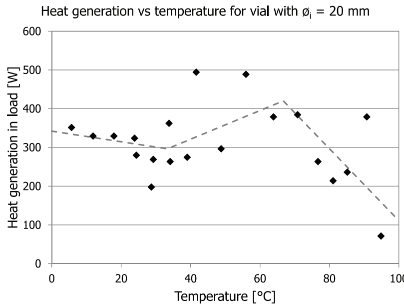

Figure D.12. Heat generation vs. temperature in the vial with the 23 mm inner diameter, A = 244 W, σ = 65 W, σ/A = 0.27.

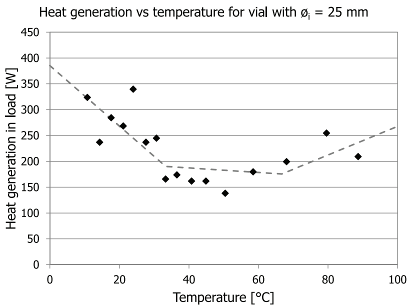

Figure D.13. Heat generation vs. temperature in the vial with the 25 mm inner diameter, A = 224 W, σ = 37 W, σ/A = 0.17.

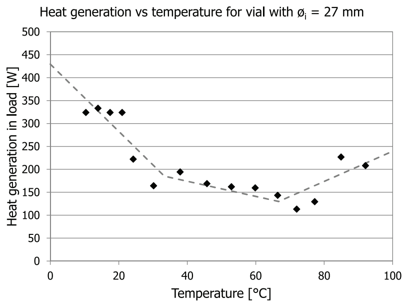

Figure D.14. Heat generation vs. temperature in the vial with the 27 mm inner diameter, A = 213 W, σ = 27 W, σ/A = 0.13.

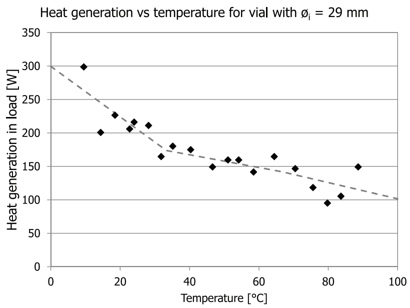

Figure D.15. Heat generation vs. temperature in the vial with the 29 mm inner diameter, A = 172 W, σ = 20 W, σ/A = 0.11.

Nomenclature

List of symbols

A	Arithmetic mean
$\mathbf{A}$	System matrix of the wave equation for the electric flux density
$\mathbf{A}_1$	System matrix of the time derivative of the magnetic field strength
$\mathbf{A}_2$	System matrix of the time derivative of the electric flux density
a	Rectangular cavity wall length
C	Heat capacity
C_p	Specific heat capacity
c_0	Speed of light in vacuum 299792458 m/s
$\mathbf{D}$	Electric flux density vector;
	System state vector of electric flux (Appendix B)
D_x D_y D_z	x-, y- and z- component resp. of electric flux vector
d	Deflection of a string
d_c	Cylindrical cavity diameter
d_l	Cylindrical load diameter
$\mathbf{E}$	Electric field strength vector
E_x E_y E_z	x-, y- and z- component resp. of electric field vector
F	Force tensioning a string
F_z	Volumetric gravitational force
f	Frequency of the time-harmonic electromagnetic field
f_A	Function describing lumped applicator behavior
f_M	Function describing lumped magentron behavior
f_r	Resonance frequency
$\mathbf{H}$	Magnetic field strength vector;
	System state vector of magnetic flux (Appendix B)
H	Enthalpy
H_x H_y H_z H_θ	x-, y-, z- and θ-component resp. of magnetic field vector
h	Cavity height; Lumped heat transfer coefficient
HU	Spatial heating rate uniformity
$\mathbf{J}$	Electric current density vector
J_n	n^{th} order Bessel function of the first kind
k	Thermal conductivity
L	Length of a string, layer thickness;
	Series inductance of transmission line
P	Electrical power
Q	Thermal power generated in an object
q	Volumetric heating rate, electromagnetic dissipation;
	Heat generation in discretization cell
R	Radius

r	Radius
S	Power transmitted by microwave fields
T	Temperature
t	Time
$t_{microwave}$	Duration of exposure to microwave field
$\mathbf{u}$	Flow velocity vector
Y_n	n^{th} order Bessel function of the second kind
α	Geometry angle
Γ	Reflection coefficient
γ	Propagation constant
ε	Electric permittivity
ε_0	Electric permittivity of vacuum
ε_{eff}	Effective permittivity
ε_r	Relative electric permittivity, $\varepsilon = \varepsilon_0\varepsilon_r$, $\varepsilon_r = \varepsilon' - i\varepsilon''$
ε'	Real part of relative electric permittivity, dielectric constant
ε'	Imaginary part of relative electric permittivity, dielectric loss factor
λ	Wavelength
λ_r	Resonance wavelength
μ	Magnetic permeability
μ_0	Magnetic permeability of vacuum
η	Dynamic viscosity; Electromagnetic impedance of a medium
η_U	Utilization efficiency
ρ	Density
ρ_w	Density of water specifically
σ	Electrical conductivity; Standard deviation
ω	Angular frequency

Terminology

TE_{lmn} TM_{lmn} Identifier of modal pattern in a rectangular cavity with l field maxima in the x-direction, m field maxima in the y-direction, and n field maxima in the z-direction. TE and TM refer to *transverse electric* and *transverse magnetic* respectively, which signifies that the respective electric or magnetic field vectors in the cavity are perpendicular to the z-direction. Figure i below presents a visualization of the TE_{101} mode in a rectangular cavity.

$TE_{\phi\varrho n}$ $TM_{\phi\varrho n}$ — Identifier of modal pattern in a cylindrical cavity with ϕ field maxima over half the circumference (θ-direction), ϱ field maxima over the diameter (r-direction), and n field maxima in the axial direction (z-direction). TE and TM refer to *transverse electric* and *transverse magnetic* respectively, which signifies that the respective electric or magnetic field vectors in the cavity are perpendicular to the z-direction. Figure ii below presents a visualization of the TM_{010} mode in a cylindrical cavity.

Microwave field — Electromagnetic wave field in the microwave spectrum, i.e. an electromagnetic field with a frequency of 300 MHz to 300 GHz or, equivalently, a wavelength of 1 m to 1 mm.

Radio waves — Electromagnetic wave field in the radio wave spectrum, i.e. an electromagnetic field with a frequency of 3 kHz to 300 GHz or, equivalently, a wavelength of 100 km to 1 mm. Aside from the microwave spectrum, the radio wave spectrum includes the very low frequency, low frequency, medium frequency, high frequency and very high frequency bands that span from 3 kHz to 300 MHz. These lower frequencies are also being used in heating applications, e.g. induction heating or high-frequency heating.

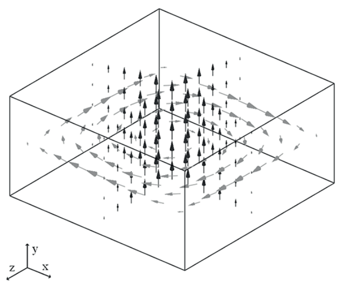

Figure i. Representation of the TE_{101} mode in a rectangular cavity. Dark arrows represent electric field lines and light arrows represent magnetic field lines. Note the orientation of the coordinate system.

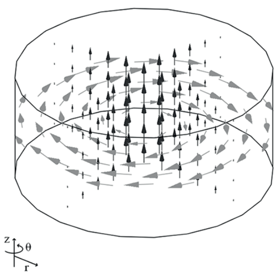

Figure ii. Representation of the TM_{010} mode in a cylindrical cavity. Dark arrows represent electric field lines and light arrows represent magnetic field lines. Note the orientation of the coordinate system.

References

1. R.A. Sheldon, Selective catalytic synthesis of fine chemicals: opportunities and trends, *J. Mol. Catal. A Chemical* 107 75–83, 1996.
2. A. Cybulski, J.A. Moulijn, M.M. Sharma and R.A. Sheldon, *Fine Chemicals Manufacture—Technology and Engineering*, Amsterdam: Elsevier, 2001.
3. A.I. Stankiewicz and J.A. Moulijn, Process intensification: Transforming chemical engineering, *Chem. Eng. Prog.* 1 22–34, 2000.
4. G. Agricola, *De Re Metallica Libri XII*, Basel: Froben, 1561. Available at http://books.google.nl/books?id=ONQLji6flSsC, accessed 9/12/2012.
5. G. Agricola, *De Re Metallica—translated from the first Latin edition of 1556*, trans. H.C. Hoover and L.H. Hoover, New York: Dover Publications, 1950.
6. R.J. Forbes, *Short History of the Art of Distillation—from the beginnings up to the death of Cellier Blumenthal*, Leiden: E.J. Brill, 1948.
7. H. Brunschwig, *Liber de Arte Distillandi de Compositis*, Strasbourg: 1512. Available at http://archive.nlm.nih.gov/proj/ttp/flash/brunschwig/brunschwig.html, accessed 9/12/2012.
8. T. Van Gerven and A. Stankiewicz, *Structure, Energy, Synergy, Time–The Fundamentals of Process Intensification*, Ind. Eng. Chem. Res. 48(5) 2465–2474, 2009.
9. D.J. Adams, J.H. Clark, P.A. Heath, L.B. Hansen, V.C. Sanders and S.J. Tavener, Novel synthetic methodologies for fluorination and perfluoroalkylation, *J. Fluorine Chem.* 101(2) 187–219, 2000.
10. W. Ehrfeld, Process Intensification Through Microreaction Technology, *Re-Engineering the Chemical Processing Plant*, eds. A. Stankiewicz and J.A. Moulijn, CRC Press, 2003.
11. V. Hessel and H. Löwe, Organic Synthesis with Microstructured Reactors, *Chem. Eng. Technol.* 28(3) 267–284, 2005.
12. V. Hessel, H. Löwe and F. Schönfeld, Micromixers – a review on passive and active mixing principles, *Chem. Eng. Sci.* 60 2479 – 2501, 2005.
13. L. Kiwi-Minsker and A. Renken, Microstructured reactors for catalytic reactions. *Catal. Today* 110 2–14, 2005.
14. D.M. Roberge, L. Ducry, N. Bieler, P. Cretton and B. Zimmermann, Microreactor Technology: a revolution for the fine chemical and pharmaceutical industries. *Chem. Eng. Technol.* 28(3) 318–323, 2005.
15. P. Watts and S.J. Haswell, The Application of Microreactors for Small Scale Organic Synthesis, *Chem. Eng. Technol.* 28(3) 290–301, 2005.
16. A. Stankiewicz, On the Applications of Alternative Energy Forms and Transfer Mechanisms in Microprocessing Systems, *Ind. Eng. Chem. Res.* 46 4232–4235, 2007.
17. D. Bogdal, *Microwave-Assisted Organic Synthesis: one hundred reaction procedures*, Amsterdam: Elsevier, 2005.
18. R. Hoogenboom, T.F.A. Wilms, T. Erdmenger and U.S. Schubert, Microwave assisted chemistry: a closer look at heating efficiency, *Aust. J. Chem.* 62(3) 236–243, 2009.
19. C.O. Kappe, Microwave dielectric heating in synthetic organic chemistry, *Chem. Soc. Rev.* 37(6) 1127–1139, 2008.
20. C.O. Kappe and D. Dallinger, Controlled microwave heating in modern organic synthesis: highlights from the 2004–2008 literature, *Mol. Divers.* 13(2) 71–193, 2009.
21. M. Larhed, C. Moberg and A. Hallberg, Microwave-accelerated homogeneous catalysis in organic chemistry, *Accounts Chem. Res.* 35(9) 717–727, 2002.
22. N.E. Leadbeater, T.M. Barnard and L.M. Stencel, Batch and continuous-flow preparation of biodiesel derived from butanol and facilitated by microwave heating. *Energ. Fuel.* 22(3) 2005–2008, 2008.
23. A. Loupy, *Microwaves in Organic Synthesis*, Weinheim: Wiley-VCH, 2006.

24. R. Luque, S.K. Badamali, J.H. Clark, M. Fleming and D.J. Macquarrie, Controlling selectivity in catalysis: selective greener oxidation of cyclohexene under microwave conditions, *Appl. Catal. A-Gen.* 341 (1–2) 154–159, 2008.
25. I. Marin, E. Adrover, D. Vega, M. Urbiztondo, M.P. Pina, R. Mallada and J. Santamaría, Fast microwave synthesis of Pt-MFI zeolite coatings on silicon micromonoliths: application to VOC catalytic combustion. *Green Process Synth.* 1 169–174, 2012.
26. J.D. Moseley, P. Lenden, M. Lockwood, K. Ruda, J.P. Sherlock, A.D. Thomson and J.P. Gilday, A comparison of commercial microwave reactors for scale-up within process chemistry, *Org. Process Res. Dev.* 12(1) 30–40, 2008.
27. A. Navarrete, R.B. Mato and M.J. Cocero, A predictive approach in modeling and simulation of heat and mass transfer during microwave heating. Application to SFME of essential oil of Lavandin Super, *Chem. Eng. Sci.* 68(1) 192–201, 2012.
28. N.M. Nikačević, A.E.M. Huesman, P.M.J. van den Hof and A.I. Stankiewicz, Opportunities and challenges for process control in process intensification, *Chem. Eng. Process.* 52 1–15, 2012.
29. P.D. Patil, V.G. Gude, L.M. Camacho and S.G. Deng, Microwave Assisted Catalytic Transesterification of Camelina Sativa Oil, *Energ. Fuel.* 24 1298–1304, 2010.
30. P.D. Patil, V.G. Gude, A. Mannarswamy, P. Cooke, S. Munson-McGee, N. Nirmalakhandan, P. Lammers and S.G. Deng, Optimization of microwave-assisted transesterification of dry algal biomass using response surface methodology, *Bioresource Technol.* 102(2) 1399–1405, 2011.
31. G. Perin, G. Alvaro, E. Westphal, L.H. Viana, R.G. Jacob, E.J. Lenardao and M.G.M. D'Oca, Transesterification of castor oil assisted by microwave irradiation, *Fuel* 87(12) 2838–2841, 2008.
32. W.L. Perry, D.W. Cooke, J.D. Katz and A.K. Datye, On the possibility of a significant temperature gradient in supported metal catalysts subjected to microwave heating, *Catal. Lett.* 47(1) 1–4, 1997.
33. W.L. Perry, A.K. Datye, A.K. Prinja, L.F. Brown and J.D. Katz, Microwave heating of endothermic catalytic reactions: reforming of methanol, *Aiche J.* 48(4) 820–831, 2002.
34. N.A. Pinchukova, V.A. Chebanov, N.Yu. Gorobets, L.V. Gudzenko, K.S. Ostras, O.V. Shishkin, L.A. Hulshof and A.Yu. Voloshko, Beneficial energy-efficiencies in the microwave-assisted vacuum preparation of polyphosphoric acid, *Chem. Eng. Process.* 50 1193–1197, 2011.
35. X.H. Qi, M. Watanabe, T.M. Aida and R.L. Smith, Fast transformation of glucose and di-/polysaccharides into 5-hydroxymethylfurfural by microwave heating in an ionic liquid/catalyst system, *Chemsuschem* 3(9) 1071–1077, 2010.
36. J.R. Schmink, C.M. Kormos, W.G. Devine and N.E. Leadbeater, Exploring the scope for scale-up of organic chemistry using a large batch microwave reactor, *Org. Process Res. Dev.* 14(1) 205–214, 2010.
37. R. Weingarten, J. Cho, W.C. Conner and G.W. Huber, Kinetics of furfural production by dehydration of xylose in a biphasic reactor with microwave heating, *Green Chem.* 12(8) 1423–1429, 2010.
38. H. Will, P. Scholz and B. Ondruschka, Microwave-Assisted Heterogeneous Gas-Phase Catalysis, *Chem. Eng. Technol.* 27(2) 113–122, 2004.
39. Y.Y. Wu, Z.H. Fu, D.L. Yin, Q. Xu, F.L. Liu, C.L. Lu and L.Q. Mao, Microwave assisted hydrolysis of crystalline cellulose catalyzed by biomass char sulfonic acids, *Green Chem.* 12(4), 696–700, 2010.
40. X.L. Zhang and D.O. Hayward, Applications of microwave dielectric heating in environment-related heterogeneous gas-phase catalytic systems. *Inorg. Chim. Acta* 359 (11), 3421–3433, 2006.
41. R. Gedye, F. Smith, K. Westaway, H. Ali, L. Baldisera, L. Laberge and J. Rousell, The use of microwave-ovens for rapid organic-synthesis, *Tetrahedron Lett.* 27(3) 279–282, 1986.
42. R.J. Giguere, T.L. Bray, S.M. Duncan and G. Majetich, Application of commercial microwave-ovens to organic-synthesis, *Tetrahedron Lett.* 27(41) 4945–4948, 1986.
43. R.K. Arvela, N.E. Leadbeater, T.L. Mack and C.M. Kormos, Microwave-promoted Suzuki coupling reactions with organotrifluoroborates in water using ultralow catalyst loadings, *Tetrahedron Lett.* 47(2) 217–220, 2006.

44. M.J. Gronnow, R.J. White, J.H. Clark and D.J. Macquarrie, Energy efficiency in chemical reactions: a comparative study of different reaction techniques. *Org. Process Res. Dev.* 9(4) 516–518, 2005.
45. A. de la Hoz, A. Diaz-Ortiz and A. Moreno, Microwaves in organic synthesis—thermal and non-thermal microwave effects, *Chem. Soc. Rev.* 34(2) 164–178, 2005.
46. M. Larhed, C. Moberg and A. Hallberg, Microwave-accelerated homogeneous catalysis in organic chemistry, *Accounts Chem. Res.* 35(9) 717-727, 2002.
47. A. Loupy, L. Perreux, M. Liagre, K. Burle and M. Moneuse, Reactivity and selectivity under microwaves in organic chemistry–relation with medium effects and reaction mechanisms, *Pure Appl. Chem.* 73(1) 161–166, 2001.
48. L. Perreux and A. Loupy, A tentative rationalization of microwave effects in organic synthesis according to the reaction medium, and mechanistic considerations, Tetrahedron 57(45) 9199–9223, 2001.
49. T. Durka, G.D. Stefanidis, T. van Gerven and A. Stankiewicz, On the accuracy and reproducibility of fiber optic (FO) and infrared (IR) temperature measurements of solid materials in microwave applications, *Meas. Sci. Technol.* 21 045108, 2010.
50. T. Durka, G.D. Stefanidis, T. van Gerven and A.I. Stankiewicz, Microwave-activated methanol steam reforming for hydrogen production, *Int. J. Hydrogen Energ.* 36 12843–12852, 2011.
51. H. Will, P. Scholz, B. Ondruschka, Heterogeneous gas-phase catalysis under microwave irradiation—a new multi-mode microwave applicator, *Top. Catal.* 29(3–4) 175–182, 2004.
52. M.A. Herrero, J.M. Kremsner and C.O. Kappe, Nonthermal microwave effects revisited: on the importance of internal temperature monitoring and agitation in microwave chemistry, *J. Org. Chem.* 73(1) 36–47, 2008.
53. M. Irfan, M. Fuchs, T.N. Glasnov and C.O. Kappe, Microwave Assisted Cross-Coupling and Hydrogenation Chemistry by Using Heterogeneous Transition-Metal Catalysts: an evaluation of the role of selective catalyst heating, *Chem.-Eur. J.* 15(43) 11608–11618, 2009.
54. I. Plazl, S. Leskovšek and T. Koloini, Hydrolysis of Sucrose by Conventional and Microwave-Heating in Stirred-Tank Reactor, *Chem. Eng. J. Bioch. Eng.* 59(3) 253–257, 1995.
55. M.H.C.L. Dressen, B. H. P. van de Kruijs, J. Meuldijk, J. A. J. M. Vekemans and L. A. Hulshof, Vanishing microwave effects: Influence of heterogeneity, *Org. Process Res. Dev.* 11 865–869, 2007.
56. M.H.C.L. Dressen, B. H. P. van de Kruijs, J. Meuldijk, J. A. J. M. Vekemans and L. A. Hulshof, From Batch to Flow Processing: Racemization of N-Acetylamino Acids under Microwave Heating, *Org. Process Res. Dev.* 13 888–895, 2009.
57. M. Komorowska, G.D. Stefanidis, T. Van Gerven, A.I. Stankiewicz, Influence of microwave irradiation on a polyesterification reaction, *Chem. Eng. J.* 155(3) 859–866, 2009.
58. International Telecommunication Union, *Radio Regulations*, Geneva, 2004.
59. J.G. van Bladel, *Electromagnetic Fields* (2nd ed.), Hoboken: Wiley, 2007.
60. D.J. Inman, *Engineering Vibration* (2nd ed.), Upper Saddle River: Prentice Hall, 2001.
61. CEM corp., *MARS 6—One Touch Makes All the Difference*, 2011. Available at http://cem.com/mars6.html, accessed 2/1/2013.
62. Milestone s.r.l., *MicroSYNTH—Microwave Synthesis Labstation*, 2009. Available at http://www.milestonesrl.com/analytical/products-microwave-synthesis-microsynth.html, accessed 2/1/2013.
63. Milestone s.r.l., *START D—Microwave Digestion System*, 2009. Available at http://www.milestonesrl.com/analytical/products-microwave-digestion-start-d.html, accessed 2/1/2013.
64. Sineo corp., *Ultra High Throughput Closed Microwave Digestion/Extraction Workstation*, 2009. Available at http://www.sineomicrowave.com/Products_px_en.asp?pid=60, accessed 2/1/2013.
65. R. Meredith, *Engineers' Handbook of Industrial Microwave Heating*, London: Institution of Electrical Engineers, 1998.
66. T.V. Chow Ting Chan and H.C. Reader, *Understanding microwave heating cavities*, Boston: Artech House, 2000.

67. G.B. Collins (ed.), *Microwave Magnetrons: MIT Radiation Laboratory Series*, New York: McGraw-Hill, 1948.
68. A.S. Gilmour, *Microwave Tubes*, Norwood: Artech House, 1986.
69. D.M. Pozar, Microwave Engineering (3rd ed.), Hoboken: Wiley, 2005.
70. *Comsol Multiphysics® 3.5 with RF-module and Heat Transfer module*, Stockholm: Comsol AB, 2008.
71. D. Karstädt, K. Möllmann and M. Vollmer, Eier im Wellensalat: Experimente mit der Haushaltsmikrowelle, *Physik in unserer Zeit* 35(2) 90–96, 2004.
72. P. Plaza-González, J. Monzó-Cabrera, J.M. Catalá-Civera and D. Sánchez-Hernández, New Approach for the Prediction of the Electric Field Distribution in Multimode Microwave-Heating Applicators With Mode Stirrers, *IEEE T. Magn.* 40(3) 1672–1678, 2004.
73. G. Roussy and J.A. Pearce, *Foundations and Industrial Applications of Microwave and Radio Frequency Fields: Physical and Chemical Processes*, Chichester: Wiley, 1995.
74. B.L. Hayes, *Microwave Synthesis: chemistry at the speed of light*, Matthews: CEM Publishing, 2002.
75. G.H. Brown, C.N. Hoyler and R.A. Bierwirth, *Theory and Application of Radio-Frequency Heating*, New York: Van Nostrand, 1947.
76. *Matlab and Simulink*®, Natrick: The Mathworks Inc., 2007.
77. A.C. Metaxas, Design of a TM_{010} resonant cavity as a heating device at 2.45 GHz, J. *Microwave Power* 9(2) 123–128, 1974.
78. K.S. Yee, Numerical Solution of Initial Boundary Value Problems Involving Maxwell's Equations in Isotropic Media, *IEEE Trans. Antenn. Propag.* 14(3) 302–307, 1966.
79. A. Taflove, *Computational Electrodynamics: The Finite-Difference Time Domain Method*, Boston: Artech House, 1995.
80. N.G. Patil et al., Personal communication, 2009.
81. U. Kaatze, K. Menzel and R. Pottel, Broad-band dielectric-spectroscopy on carboxylic-acid water mixtures-dependence upon composition, *J. Phys. Chem.-US* 95(1) 324–331, 1991.
82. C. Gabriel, S. Gabriel, E.H. Grant, B.S.J. Halstead and D.M.P. Mingos, Dielectric parameters relevant to microwave dielectric heating, *Chem. Soc. Rev.* 27(3) 213–223, 1998.
83. T. Meissner and F. Wentz, The Complex Dielectric Constant of Pure and Sea Water from Microwave Satellite Observations, 2004. Available at http://www.remss.com/papers/ssmi/the_complex_dielectric_constant_of_pure_and_sea_water_from_microwave_satellite_observations.pdf, accesses 26/11/2009.
84. T. Hao, The role of the dielectric loss of dispersed material in the electrorheological effect, *Appl. Phys. Lett.* 70 (15) 1956–1958, 1997.
85. G.A. Tompsett, W.C. Conner and K.S. Yngvesson, Microwave synthesis of nanoporous materials, *Chemphyschem* 7(2) 296–319, 2006.
86. F. Chemat, D.C. Esveld, M. Poux and J.L. Di-Martino, The role of selective heating in the microwave activation of heterogeneous catalysis reactions using a continuous microwave reactor, *J. Microwave Power EE* 33(2) 88–94, 1998.
87. W.E. Jennings, *Microwave-assisted chemical synthesis instrument with fixed tuning*, Patent No. US 6753517 B2, 2004.
88. CEM corp., *Discover legacy systems – Microwave Synthesizers*, 2011. Available at http://www.cem.com/discover-legacy-systems.html, accessed 20/12/2011.
89. J. Robinson, S. Kingman, D. Irvine, P. Licence, A. Smith, G. Dimitrakis, D. Obermayer and C.O. Kappe, Understanding microwave heating effects in single mode type cavities—theory and experiment, *Phys. Chem. Chem. Phys.* 12 4750–4758, 2010.
90. J. Zhu, A.V. Kuznetsov and K.P. Sandeep, Mathematical modeling of continuous flow microwave heating of liquids (effects of dielectric properties and design parameters), *Int. J. Therm. Sci.* 46 328–341, 2007.

91. *2M218 specifications*. Available at http://www.k3r.com.br/download/Magnetrons%20serie%202M218.pdf, accessed 06/01/2012.
92. Schott AG, *BORO-8330™ technical data*, 2010. Available at http://www.schott.com/tubing/english/product_selector/index.html?glassid=BORO-8330, accessed 23/08/2010.
93. The Engineering Toolbox, *Water – thermal properties*, 2010. Available at http://www.engineeringtoolbox.com/water-thermal-properties-d_162.html, accessed 22/10/2010.
94. The Engineering Toolbox, *Water – dynamic and kinematic viscosity*, 2010. Available at http://www.engineeringtoolbox.com/water-dynamickinematic-viscosity-d_596.html, acces-sed 22/10/2010.
95. The Engineering Toolbox, *Solids – specific heats*, 2010. Available at http://www.engineeringtoolbox.com/thermal-conductivity-d_429.html, accessed 22/10/2010.
96. Neoptix Canada LP, *T1™ Fiber Optic Temperature Probe*, 2010. Available at http://www.neoptix.com/literature/v1002_Datasheet_t1.pdf, accessed 6/1/2012.
97. Neoptix Canada LP, *Reflex™ Signal Conditioner*, 2009. Available at http://www.neoptix.com/literature/v1001_Datasheet_reflex.pdf, accessed 6/1/2012.
98. E.R. De Castro, M.B. Mourao, L.A. Jermolovicius, C. Takano and J.T. Senise, Carbothermal Reduction of Iron Ore Applying Microwave Energy, *Steel Res. Int.* 83(2) 131–138, 2012.
99. N.G. Patil, A.I.G. Hermans, F. Benaskar, J. Meuldijk, L.A. Hulshof, V. Hessel, J.C. Schouten and E.V. Rebrov, Energy efficient and controlled flow processing under microwave heating by using a millireactor-heat exchanger, *AICHE J.* 58(10) 3144–3155, 2012.
100. B. Toukoniitty, J.P. Mikkola, D.Y. Murzin and T. Salmi, Utilization of electromagnetic and acoustic irradiation in enhancing heterogeneous catalytic reactions, *Appl. Catal. A* 279(1–2) 1–22, 2005.
101. B. Toukoniitty, J. Warna, J.P. Mikkola, M. Helle, H. Saxen, D.Y. Murzin and T. Salmi, Modelling of enantioselective and racemic hydrogenation of ethyl pyruvate on a Pt/Al2O3 catalyst in the presence of microwave irradiation, *Chem. Eng. Process.* 48(4) 837–845, 2009.
102. Microwaves101.com, *Rectangular Waveguide Dimensions*, 2012. Available at: http://www.microwaves101.com/encyclopedia/waveguidedimensions.cfm, accessed 29/4/2012.
103. Sairem SAS, Personal Communication, 25/1/2011.
104. Sairem SAS, *2450 MHz Magnetron*, 2009. Available at http://www.sairem.com/gb/produits/microwave_generator/microwave_generator_2450_magnetron.html, accessed 29/04/2012.
105. Sairem SAS, *Microwave components*, 2009. Available at http://www.sairem.com/gb/produits/composants_mo/composants_mo.html, accessed 29/04/2012.
106. E. Altman, G.D. Stefanidis, T. van Gerven and A. Stankiewicz, Microwave-Promoted Synthesis of n-Propyl Propionate using Homogeneous Zinc Triflate Catalyst, *Ind. Eng. Chem. Res.* 51(4) 1612–1619, 2012.
107. E. Altman, G.D. Stefanidis, T. van Gerven and A.I. Stankiewicz, Process Intensification of Reactive Distillation for the Synthesis of n-Propyl Propionate: The Effects of Microwave Radiation on Molecular Separation and Esterification Reaction, *Ind. Eng. Chem. Res.* 49(21) 10287–10296, 2010.
108. Sairem SAS, *Labotron Extraction & Synthesis 2450 MHz*, 2010. Available at http://www.sairem.com/fiches_techniques/equipements/Labotron%20X%20EN.pdf, accessed 6/1/2012.
109. M. Izadifar, O.D. Baik and G.S. Mittal, Radio frequency-assisted extraction of podophyllotoxin: Prototyping of packed bed extraction reactors and experimental observations, *Chem. Eng. Process.* 48(10) 1437–1444, 2009.
110. Y. Zhu and A.C. Cangellaris, *Multigrid finite element methods for electromagnetic field modeling*, Hoboken: Wiley-Interscience, 2006.

Curriculum Vitae

Guido Sturm was born on the 16th of April 1980. After graduating in 1998 from secondary school, atheneum at the Norbertuscollege, he began his studies in mechanical engineering at Delft University of Technology, obtaining his BSc and MSc degrees in 2004 and 2006 respectively. Specializing in control engineering and mechatronics, his graduation project was on the design of a plant-wide control system for a nuclear cogeneration plant. In 2008 he began his work as a PhD researcher at the Process & Energy department of Delft University of Technology. The results of his research have been presented in internationally renowned conferences and published in peer reviewed scientific journals. Since November 2012 he is employed as a postdoctoral researcher at the same department and working on the development of microwave plasma gasification technology for biomass.

List of publications

Journal articles

G.S.J. Sturm, G.D. Stefanidis, M.D. Verweij, T. van Gerven, A.I. Stankiewicz, Design principles of microwave applicators for small-scale process equipment, *Chem. Eng. Process.* 49 912–922, 2010.

G.S.J. Sturm, M.D. Verweij, T. van Gerven, A.I. Stankiewicz, G.D. Stefanidis, On the effect of resonant microwave fields on temperature distribution in time and space, *Int. J. Heat Mass Tran.* 55 3800–3811, 2012.

G.S.J. Sturm, M.D. Verweij, T. van Gerven, A.I. Stankiewicz, G.D. Stefanidis, On the Parametric Sensitivity of Heat Generation by Resonant Microwave Fields in Process Fluids, *Int. J. Heat Mass Tran.* 57 375–388, 2013.

G.S.J. Sturm, A.Q. van Braam Houckgeest, M.D. Verweij, T. van Gerven, A.I. Stankiewicz, G.D. Stefanidis, Exploration of Rectangular Waveguides as a Basis for Microwave Enhanced Continuous Flow Chemistries, *Chem. Eng. Sci.* 89 196–205, 2013.

M. Komorowska-Durka, M. Barmen 't Loo, G.S.J. Sturm, M. Radoiu, M. Oudshoorn, T. Van Gerven, A.I. Stankiewicz, G.D. Stefanidis, Novel microwave reactor equipment using internal transmission line (INTLI) for efficient liquid phase chemistries: A study-case of polyester preparation, *Chem. Eng. Process.* 69 83–89, 2013.

G.S.J. Sturm, M.D. Verweij, A.I. Stankiewicz, G.D. Stefanidis, Microwaves and Microreactors: Design Challenges and Remedies, *Chem. Eng. J.* (under review).

G.D. Stefanidis, G.S.J. Sturm, A. Navarrete, A.I. Stankiewicz, A Helicopter View of Microwave Application to Chemical Processes: Reactions, Separations, and Equipment Concepts, *Rev. Chem. Eng.* (under review).

Book contribution

G.S.J. Sturm, A.I. Stankiewicz, G.D. Stefanidis, Microwave Reactor Concepts: From Resonant Cavities to Traveling Fields, *Novel Reactor Concepts*, M. van Sint Annaland and F. Gallucci (eds.), London: Imperial College Press (in press).

Conference paper (selection)

G.S.J. Sturm, M.D. Verweij, T. Van Gerven, G.D. Stefanidis, A.I. Stankiewicz, Applicator design for microwave enhanced microprocessing, *Proceedings of the 13th International Conference on Microwave and RF Heating AMPERE 2011*, 48–51 (electronic version).

Oral presentations

Analysis of Microwave Fields and Heating Uniformity in Micro- and Small Structured Process Systems in Single Mode Microwave Applicators, CAPE Forum, Aachen, 2010.

Conceptual Design of Electromagnetic Heating Applicators for Microreactors, Netherlands Process Technology Symposium (NPS10), Veldhoven, 2010.

Applicator design for microwave enhanced microprocessing, 13th International Conference on Microwave and High Frequency Heating AMPERE 2011, Toulouse, 2011.

Applicator design for microwave enhanced microprocessing, 8th European Congress of Chemical Engineering (ECCE), Berlin, 2011.

Microwave Processing System Design, 9th European Congress of Chemical Engineering (ECCE), The Hague, 2013.

Microwave Processing System Design, 14th International Conference on Microwave and High Frequency Heating AMPERE 2013, Nottingham, 2013.

Acknowledgements

Well, here we go again. Sitting in a hotel room to participate in a conference that starts the next day. It strikes me that every time you leave home for such events they let you into the airplane, the hotel is there, your reservation exists, and that there is a badge with your name on it waiting for you at the registration desk. As if like magic everything works out like clockwork and the event is there to explore. Not that I believe in magic though. It's more like people doing a lot of hard work organizing it, and planning it for several years beforehand. So as I slump down on the bed in this fine hotel room – the Bridal Suite no less – watching a Scandinavian motorcycle journey report on the Travel Channel, looking back over the past years I recognize the same experience while living the PhD life resulting in this thesis. Back when I started, I figured that it would probably involve lots of hard work, but I couldn't really picture myself actually writing a dissertation. And yet, here we are, as if like magic the thesis is there. All I have to do is work out these final bits. It is a frustratingly slow process again. Propositions and acknowledgements are the least important, but most red parts of a PhD thesis, so I really need to put some effort into it. Scoping out the hotel room for inspiration I notice the classical wooden ornaments, the drawings of scarcely clad ladies and the timeless, mass-produced statuette of two angels doing whatever angels are doing. I wonder... How many people would have crashed their heads into the ceiling during the final wild celebrations on that very significant day of both their lives? Would they have noticed that this bed is on a raised platform? Or would they have simply forgotten it? Embracing, and embraced in this brown flower wallpapered goodness. I notice no dark stains, but imagining this embarrassing wedding night mishap amuses me. In any case more so than watching the presenter on the tv show looking as miserable as the Norwegian rain pouring down on him while asking himself how on earth he got on that motorcycle on that road in that part of the world of which it is well known that it averages 235 rainy days a year. How did that happen? How do people get into places? *How did I get here?* Well, by airplane and train mostly. Traveling all day. But that is not the real answer. In fact, the real answer is about the people around you. About this web of personal interaction that pulls you forward. About the reason why I'm writing these acknowledgements, *dit dankwoord*. So where to start?

I would like to start with thanking everyone who I encountered from the start to the completion of my PhD project. It has been a period of great professional and personal development and of many inspiring and enjoyable moments. Chats, drinks, dinners, lunches, parties, coffee breaks, even meetings, these are the things that make the life worth living, so therefore, dear colleagues, scientific staff, support staff, students, business contacts, friends I would like to thank you very much.

I would like to thank in particular a number of people who made an important contribution to this thesis, to my pleasure of working on it, or to both these things. Ten eerste wil ik mijn promotor Andrzej Stankiewicz bedanken voor de gelegenheid om dit project aan te pakken. Het bleek een interessante, uitdagende klus en ik waardeer de vrijheid en de begeleiding die ik hierbij kreeg. Ik hoop dat de chemische fabriek van 2050 er een stap dichterbij mee is gekomen, en dat wat wij nu als procesintensificatie zien dan gangbare technologie zal zijn geworden. Verder wil ik Tom van Gerven bedanken voor de dagelijkse begeleiding in het begin van het project. Tom, al was het een korte periode, hartelijk dank dat je me op weg hebt geholpen. Mijn bijzondere dank gaat uit naar Martin Verweij. Zonder jouw hulp en ondersteuning op het gebied van elektromagnetisme had dit proefschrift er heel anders uitgezien. Onze prettige samenwerking, je kritische reflecties en scherp oog voor details hebben veel bijgedragen aan het werk en, Martin, ik wil je daar bijzonder voor bedanken. To Georgios Stefanidis, my daily supervisor, many thanks for your guidance and motivation. It was a pleasure collaborating with you on the project and on developing new ideas. I am very grateful for your help in fitting the work in the right context. I am looking forward to our continued collaboration on plasma gasification. I would also like to thank our partners at Eindhoven University, STW, and the user committee of the project, in particular my fellow PhD-students Narendra and Faysal. It was a pleasure working with you guys. Many thanks go out to my microwave colleagues Magda, Tomek and Ernesto. It was a pleasure to work alongside you in the same field of research and I enjoyed sharing an office with you. I wish you all the best in your career and in life. Ik ben buitengewoon dankbaar voor het werk van mijn student Andreas. Andreas, jouw inzet heeft ons veel geholpen en het was een genoegen om met je samen te werken. To my officemates not already mentioned, initially Xiaohua, Aylin and Stephanie, and later Martijn, Daniel, Iza, Alex and Maryam, thank you for the times we shared and for all the interesting discussions, coffee breaks and chats. Of course I must also mention my IRS colleagues for whom much of the same goes: Somnath, Herman, Maloes, Ana, Samir, Widya, Sander, George, Richard, David, Christian, Jelan, Joop, Marta, Cristian, Norbert, Ali and others, thank you very much. Many thanks go out to all P&E colleagues. It was and still is a real pleasure to be in our department. Mijn speciale dank gaat uit naar Leslie, Helma en Ilona, onze fantastische management assistentes, en naar Rob, de energieke regelaar die onze afdeling in het juiste spoor houdt. Verdere bijzondere dank gaat uit naar onze werkplaats voor de technische ondersteuning, met name naar Andre, Gerard, Jan en Martijn voor het werk aan de opstelling. Er waren wat hobbels, maar het ding ziet er dan ook uit als een laserkanon. Bijzondere dank gaat ook uit naar Michel voor de ondersteuning in het lab, in mijn eentje had ik de weg daar nooit gevonden. Dan nog mijn dank aan de nog niet genoemde bewoners van de Candyshop, ik was er vaak te vinden en het

kan geen toeval zijn dat ik er zelf ook terecht ben gekomen. Dennis, Mahinder, Jurriaan, dank voor de uitstekende service.

Ten slotte wil ik vrienden en familie bedanken. In het bijzonder natuurlijk mijn broertjes en mijn moeder. Bedankt voor jullie begrip en ondersteuning.